Assessment of Feedbacks in the Earth System under Anthropogenic Forcing: Two Case Studies

Dissertation

ZUR ERLANGUNG DES DOKTORGRADES

DER MATHEMATISCH - NATURWISSENSCHAFTLICHEN FAKULTÄT

DER CHRISTIAN-ALBRECHTS-UNIVERSITÄT ZU KIEL

VORGELEGT VON

TRONJE PEER KEMENA

KIEL, OKTOBER 2017

1. Gutachter:	Prof. Dr. Andreas Oschlies
2. Gutachterin:	Prof. Dr. Katja Matthes
Referent:	Prof. Dr. Andreas Oschlies
Koreferent:	Prof. Dr. Katja Matthes
Disputationsdatum:	15.12.2017

Zum Druck genehmigt

---

gez. Prof. Dr. Natascha Oppelt, Dekanin

Summary

Feedbacks determine the sensitivity of the Earth system to perturbations. In the last centuries, the Earth system has been undergoing substantial changes caused to a great extent from the human activity. Nowadays, it is well documented that global warming is mainly driven by the anthropogenic emissions of greenhouse gases. In the future, these emissions will likely continue and lead to further climate warming. Large-scale climate engineering projects are human actions proposed to counteract climate warming. However, these projects could also cause unintentionally perturbations to the Earth system or its subsystems.
Scientists apply models to estimate the impact of these anthropogenic forcings on the Earth system in future projections. Therefore it is important that feedbacks are well represented in these models to make reliable predictions.

The aim of this PhD thesis is to advance the research in feedbacks and their response to anthropogenic forcing in the Earth system or its subsystems. Two case studies are carried out with a focus on a) the atmospheric feedbacks in North Africa driven by an irrigated afforested Sahara, and b) the biogeochemical feedbacks related to the phosphorus cycle and its link to oceanic deoxygenation.

Regarding the first case study, the irrigated afforestation of the Sahara has been proposed as a climate engineering method to sequester a substantial amount of carbon dioxide from the atmosphere, which might potentially be effective to mitigate climate change. Substantial amounts of irrigation are required to sustain the artificial forest. Enhanced evapotranspiration would moisten the Saharan air. Its impact on the global atmospheric hydrological cycle and circulation is widely unexplored.
In this thesis, a state-of-the-art Earth system model is used for the first time to investigate in detail atmospheric feedbacks and their side effects due to such a large-scale afforestation project.
Atmospheric feedbacks reduce the precipitation potential over an afforested Sahara and raise questions about the self-sustainability of such an artificial forest. Only 26% of the evapotranspirated water re-precipitates over the Sahara, considerably large amounts are advected southward to the Sahel zone and westward to the North Atlantic.
In the Sahel zone, a complex atmospheric circulation feedback and the adaptation of the Tropical easterly jet and African easterly jet to the afforestation lead to an enhancement of the West African Monsoon precipitation.
In the North Atlantic tropical cyclones (TCs) are intensified. Advection of humidity from the afforested Sahara to the North Atlantic improves environmental conditions for the development of Atlantic TCs. The Saharan afforestation has a considerably larger impact on the TC development than a worst-case global warming scenario.

Regarding the second case study, observations indicate ongoing deoxygenation in the ocean and the expansion of suboxia both likely driven by climate change. Previous studies of former oceanic anoxic events proposed a link between large-scale deoxygenation and ocean phosphorus (P) inventory. Under climate warming, weathering supplies additional P to the ocean, which in turn promotes ocean productivity and deoxygenation. A feedback between benthic release of P and ocean biological productivity, the so-called oxygen productivity feedback, could further enhance the deoxygenation. Models are applied to predict future expansion of suboxia, but most of these models show still a lack in simulating the present-day trend in the decline of the oceanic oxygen inventory. This indicates that still large uncertainties exist

and that it is necessary to reevaluate feedbacks, which are related to the deoxygenation process.
In this thesis, an Earth system model of intermediate complexity is used to investigate feedbacks and their uncertainties between the P cycle and the deoxygenation in the ocean in a business-as-usual scenario on millennial timescales. Model results confirm the link between marine P inventory and ocean deoxygenation; until year 5000, a 4 to 5-fold expansion of suboxic water volume occur. Low oxygen bottom waters lead to a release of P from ocean sediments, which might cause further expansions of suboxia due to the oxygen productivity feedback. However, this feedback has a minor impact on deoxygenation in this study.
In addition, expanding suboxia leads to an increase in denitrification and thus to nitrogen limitation and a decrease in biological productivity. This negative feedback limits the utilization of the added P. Since nitrogen fixation is not able to counteract the nitrogen loss due to denitrification, considerably large amounts of the added P leave the ocean surface unused as preformed P.
Finally, model uncertainties are investigated. Model simulations show a large spread in weathering and benthic fluxes of P. Consequentially, the suboxic volume ranges between 1 and 5% of the whole ocean volume in year 5000. Different assumptions for weathering parameters, the representation of slope and shelfs in the model bathymetry, different parametrization of benthic fluxes and limits to the benthic P release by a simple sediment P inventory, all these factors have a large impact on the results. For example, the limited inventory of P further reduces the effect of the oxygen productivity feedback on the deoxygenation.

This PhD thesis advances the understanding of the North African climate system and their feedbacks under an artificial large-scale afforestation scenario. It reveals the potential and unintentional side effects of such a climate engineering project. Furthermore, this thesis discusses to what extent human activity could drive the global ocean suboxic or anoxic and reassessed the relevance of the different feedbacks for the deoxygenation of the ocean.

Zusammenfassung

Feedbacks bestimmen die Sensititvität des Erdsystems und des Klimas gegenüber Störungen. In den letzten Jahrhunderten hat das Erdsystem erhebliche Klimaveränderungen erfahren, die in hohem Maße vom Menschen verursacht wurden. Aktuelle Studien zeigen, dass die globale Erwärmung hauptsächlich durch die anthropogenen Emissionen von Treibhausgasen verursacht wird. Diese Emissionen werden vermutlich noch länger andauern und zu einer weiteren Klimaerwärmung führen. Groß angelegte Climate Engineering Projekte sind Maßnahmen um dieser Klimaerwärmung entgegenzuwirken. Diese Projekte könnten jedoch auch zu unbeabsichtigten Veränderungen im Erdsystems führen.
Die Wissenschaftler wenden Erdsystemmodelle an, um den anthropogenen Einfluss das Erdsystem abzuschätzen. Dabei ist es wichtig, dass Feedbacks in diesen Modellen gut repräsentiert werden, um zuverlässige Vorhersagen zu treffen.

In dieser Doktorarbeit werden Feedbacks und deren Auswirkungen auf das Erdsystem oder dessen Subsystemen untersucht. Zwei Fallstudien wurden durchgeführt mit Fokus auf a) die atmosphärischen Feedbacks hervorgerufen durch die Bewässerung und Aufforstung der Sahara und b) biogeochemische Feedbacks im Zusammenhang mit dem Phosphorzyklus und der Abnahme von Sauerstoff im Ozean.

In früheren Studien wurde die Bewässerung und Aufforstung der Sahara als eine Climate Engineering Methode vorgeschlagen, um die atmosphärische Konzentration von Kohlenstoffdioxid zu reduzieren, was möglicherweise zur Abschwächung der Klimaerwärmung führen könnte. Große Mengen an Wasser sind jedoch notwendig, um die gepflanzten Bäume zu bewässern. Dies würde zu einer erhöhten Evapotranspiration und zu einer erhöhten Luftfeuchtigkeit in der Luft über der Sahara führen. Die daraus resultierenden Auswirkungen auf die atmosphärische Zirkulation und auf den globalen Wasserkreislauf sind weitestgehend unerforscht.
In der ersten Fallstudie wird erstmals ein hochmodernes Erdsystemmodell angewendet, um atmosphärische Feedbacks und deren Nebenwirkungen hervorgerufen durch die Bewässerung und Aufforstung der Sahara im Detail zu untersuchen.
Atmosphärische Feedbacks reduzieren das Niederschlagspotenzial über einer aufgeforsteten Sahara, was die Frage aufwirft, ob ein künstlicher Wald in der Sahara nachhaltig sein kann. Nur 26% des durch Evapotranspiration verlorenen Wassers regnet wieder über der Sahara aus, beträchtliche Mengen werden nach Süden in die Sahelzone und nach Westen in den Nordatlantik transportiert.
In der Sahelzone führen komplexe Feedbacks der atmosphärischen Zirkulation und Veränderungen des Tropical Easterly Jets und des African Easterly Jets durch die Aufforstung zu verstärkten Niederschlägen während des Westafrikanischen Monsuns.
Im Nordatlantik werden tropische Wirbelstürme (TWs) verstärkt. Feuchtigkeit wird von der Sahara in den Nordatlantik transportiert. Die dort erhöhte Luftfeuchtigkeit verbessert die Bedingungen für die Entstehung und Entwicklung von atlantischen TWs. Die Aufforstung der Sahara hat auf die Entwicklung der TWs einen wesentlich größeren Einfluss als in einem Business-as-usual Szenario.

In der zweiten Fallstudie wird der anthropogene Einfluss auf die Entstehung von Suboxia untersucht. Beobachtungen deuten auf eine fortschreitende Abnahme der Sauerstoffkonzentration im Ozean und eine Ausdehnung der Suboxia hin, was potentiell auf den Klimawandel zurückzuführen ist. Paleo Studien von ozeanischen anoxischen Ereignissen fanden einen Zusammenhang zwischen globaler Abnahme von Sauerstoff im Ozean und dem Phosphor (P) Inventar des Ozeans. Eine Zunahme der terrestrischen

Verwitterung von P durch die Klimaerwärmung führt zu einer Zunahme von P im Ozean, was wiederum die marine biologische Produktivität stimuliert und damit zu einer Abnahme von Sauerstoff im Ozean führt. Ein Feedback zwischen der benthischen Freisetzung von P und der biologischen Produktivität im Ozean, der Sauerstoff-Produktivitäts Feedback, könnte die Sauerstoffabnahme weiter beschleunigen. Modelle werden verwendet, um die zukünftige Ausdehnung von Suboxia vorherzusagen. Die meisten dieser Modelle zeigen jedoch immer noch Defizite bei der Simulation des gegenwärtigen Trends in der Sauerstoffabnahme. Dies könnte auf Unsicherheiten im Hinblick auf die genannten Feedbacks hinweisen.
In dieser Arbeit wird ein Erdsystemmodell mit mittlerer Komplexität verwendet, um Feedbacks zwischen dem P-Kreislauf und der Sauerstoffabnahme im Ozean in einem Business-as-usual Szenario auf Zeitskalen von tausenden Jahren und deren Unsicherheiten zu untersuchen. Die Modellergebnisse bestätigen den Zusammenhang zwischen dem P-Inventar des Ozeans und der Sauerstoffabnahme. Bis zum Jahr 5000 nimmt das suboxische Ozeanvolumen um das 4 bis 5-fache zu. Suboxisches Bodenwasser führt hierbei zu einer Freisetzung von P von den Ozeansedimenten, was eine weitere Ausbreitung von Suboxia verursachen könnte. In diesem Modell hat der Sauerstoff-Produktivitäts Feedback jedoch einen geringen Einfluss auf die Sauerstoffabnahme im Ozean. Insbesondere limitiert das begrenzte P-Inventar im Sediment die Freisetzung von P und damit auch den Feedback.
Darüber hinaus führen Ausbreitung der Suboxia auch zu einer Zunahme der Denitrifikation und damit zu einer Stickstofflimitierung und einer Abnahme der biologischen Produktivität. Dieser negative Feedback begrenzt die Aufnahme des hinzugefügten Ps. Da die Stickstofffixierung den durch die Denitrifikation verursachten Stickstoffverlust nicht kompensieren kann, bleiben große Mengen an P in der oberflächennahen Mischungsschicht des Ozeans ungenutzt.
Abschließend wurden Modellunsicherheiten untersucht. Die Modellsimulationen zeigen eine große Streuung bezüglich der Verwitterung und der benthischer Flüssen von P. Unterschiedliche Annahmen für Verwitterungsparameter, die bessere Darstellung von Schelfen in der Modell-Bathymetrie, unterschiedliche Parametrisierung benthischer Flüsse und die Begrenzung der benthischen P-Freisetzung durch ein einfaches P-Inventar im Sediment hat einen großen Einfluss auf die Ergebnisse. Folglich liegt das suboxische Volumen im Jahr 5000 zwischen 1 und 5% des gesamten Ozeanvolumens.

Diese Dissertation verbessert das wissenschaftliche Verständnis des nordafrikanischen Klimasystems und deren Feedbacks im Rahmen eines Aufforstungsszenarios der Sahara. Das Potential und die unbeabsichtigten Nebenwirkungen eines solchen Climate Engineering Projekts werden aufgezeigt. Darüber hinaus wird in dieser Arbeit diskutiert, inwieweit der anthropogene Einfluss den globalen Ozean in einen suboxischen oder in einen anoxischen Zustand führen könnte. Die unterschiedliche Relevanz der Feedbacks für die Sauerstoffabnahme im Ozean wird neu beurteilt.

Acknowledgements

First and foremost, I want to deeply thank both Andreas Oschlies and Katja Matthes for giving me the opportunity to perform my research as a doctoral candidate and write this PhD thesis. Without their guidance and financial support, this dissertation would not have been possible.
I would like to thank my primary advisor Andreas Oschlies for his supervision and his valuable contribution to my project, for trusting me, for securing funds for me but above all for giving me the freedom of individual research and for allowing me to evolve as a scientist.
I would also like to express my appreciation and gratitude to my advisor Katja Matthes for constantly offering me her support and advice and for contributing to the financing of my research. Her meticulous comments were an enormous help to me and improved significantly the manuscripts.
I am very grateful to my colleagues Thomas Martin, Iris Kriest, Wolfgang Koeve, Klaus Wallmann, Ulrike Löptien, Heiner Dietze, Daniela Niemeyer, Katrin Meissner, Sebastian Wahl, Christiane Schelten, Andy Dale, Rita Erven and Angela Landolfi for the excellent collaboration, the interesting discussions, their insightful comments and suggestions on my manuscripts.
I also like to thank my colleagues Fabian Reith, Wanxuan Yao and all the colleagues from the Biogeochemical Modeling Group of GEOMAR for creating an excellent working environment throughout my time as a PhD student and for the nice discussions.
On a personal level, I would like to thank my family, especially my parents, for their support on my pursuits and for initiating my intellectual development and my interest for science from an early age on. I also want to deeply thank my girlfriend Evangelia Louropoulou for her great support, for her endless patience, for cheering me up and for giving me hope in times when I felt desperate. Finally, I thank all my friends for being tolerant and supportive throughout my journey.

Thank you all!

Tronje Kemena

Content

1. Introduction

1.1 Motivation and outline

It is widely accepted, and confirmed by observations, that human activity perturbs the global climate system. Because the global Earth system is highly complex, anthropogenic forcing leads not only to simple cause and effect relationships. Instead the whole Earth system interacts with the anthropogenic forcing, which could lead to further side-effects or to feedbacks. A feedback appears when the initial perturbation initiates a process or a chain of processes that again affects the perturbation itself. Feedbacks can amplify or dampen the initial perturbation. The individual feedback strength can depend on the climate state onto which the perturbation is imposed (for example palaeo or present-day climate). Because feedbacks determine the sensitivity of the climate system to perturbations, it is crucial to understand their role in the Earth system. A better representation of feedbacks in models can help to predict the development of the climate and help to determine, if anthropogenic forcing could drive the Earth system or parts of the Earth system into a new equilibrium. At some point, during the transition from the former to the new equilibrium, positive feedbacks would overcome negative feedbacks. Beyond this point, the so-called tipping point, these feedbacks drive the climate into a new equilibrium even without additional anthropogenic forcing.

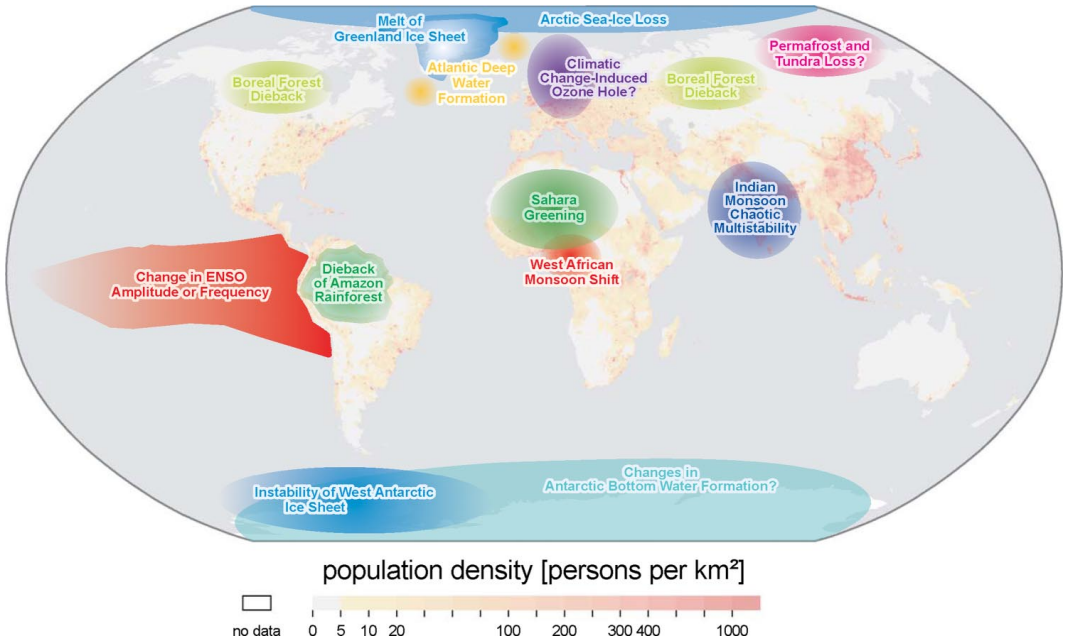

Fig. 1 Map of potential policy-relevant tipping elements in the climate system and global population density. They could be triggered this century and would undergo a qualitative change within this millennium. Tipping elements are excluded from the map systems, which qualitative change would appear beyond this millennium (e.g., ocean anoxia). Question marks indicate systems whose status as tipping elements is particularly uncertain. Figure and caption adapted from Lenton et al. (2008).

The climate system can be divided up into subsystems, called tipping elements (Fig. 1), with each tipping element containing a tipping point (Lenton et al., 2008). Lenton et al. (2008) found several policy-relevant tipping elements (Fig. 1), which can affect a significant number of people in the future. For example the Sahara Greening or a West African Monsoon Shift would affect directly a large number of people (see Fig. 1 population density). Large scale anoxia would also affect a large number of people indirectly by affecting the marine ecosystem and fishery.

The aim of this PhD thesis is to advance the research in tipping elements. A large number of tipping elements exist and therefore two case studies are performed with a focus on Earth system feedbacks:

1. Atmospheric feedbacks in North Africa driven by an irrigated afforested Sahara (Chapter 2, 3)
2. Biogeochemical feedbacks related to the phosphorus cycle and its link to oceanic deoxygenation (Chapter 4, 5)

The structure of the thesis is as follows. First a general introduction (Section 1.2) is given. The general introduction describes the beginning of human climate intervention and their feedbacks (Section 1.2.1), a linear concept for climate feedbacks (Section 1.2.1.1) and how model development expands the representation of feedbacks in Earth-system models (Section 1.2.2).

In the first case study, atmospheric feedbacks in the North African climate system (introduced in Section 1.3) to an artificial afforestation are investigated. Artificial afforestation is proposed as one climate engineering option to sequester carbon dioxide from the atmosphere (Ornstein et al., 2009; Keller et al., 2014; Bowring et al., 2014). The past greening of the Sahara (Section 1.4) could suggest that initiated atmospheric feedbacks by irrigation and afforestation could sustain a Green Sahara, which would, in turn, reduce irrigation efforts (“Artificial Green Sahara" is used in the following as a synonym for an irrigated and afforested Sahara). In this thesis the self-sustainability of an artificial Green Sahara, the effect on the West African Monsoon (Chapter 2) and potential consequences for tropical cyclone development (Chapter 3) are assessed.

In the second case study, future deoxygenation of the ocean under a “business-as-usual" scenario is investigated. The role of enhanced phosphate weathering, anthropogenic phosphate fluxes, sediment fluxes and their feedbacks are considered. In contrast to the annual to decadal timescales associated with atmospheric feedbacks (first case study), weathering and sediment fluxes influence the ocean on millennial timescales. In an anoxic environment, redox conditions can lead to an excess release of P from the sediment and lead to high rates of recycling of P in the ocean (see biogeochemical

feedbacks related to the ocean oxygen inventory in Section 1.5). Several Oceanic Anoxic Events (OAEs) occurred already in the past, which probably caused mass extinctions in the ocean (Section 1.6). The relevance of the phosphorus-oxygen feedback for the development of potential future OAEs (Chapter 4) and its uncertainties (Chapter 5) are assessed.

The research questions are formulated in Section 1.7. Chapters 2 and 3 present the first case study and Chapters 4 and 5 the second case study. The overall conclusion can be found in Section 6.

1.2 General Introduction

1.2.1 Early signs of human climate intervention: The Ruddiman Hypothesis

The Ruddiman Hypothesis (Ruddiman, 2003) states that anthropogenic forcing changed the Earth system already thousand years ago. This hypothesis is supported by ice core records and proxy data (Fuller et al., 2011; Kaplan et al., 2011; Marcott et al., 2013; Mitchell et al., 2013). 10000 years ago, orbital driven methane (CH_4) and carbon dioxide (CO_2) removal would have initiated the beginning of a new ice age cycle, if not inhibited by anthropogenic climate warming (Fig. 2.2; Ruddiman et al., 2005). Already 5000 years ago anthropogenic CH_4 emissions started due to irrigation for rice in Asia and lead to a greenhouse effect on temperature (Ruddiman, 2003). Anthropogenic CH_4 accumulated in the atmosphere by 230 ppb until the beginning of industrialization (Fig. 2.2a), whereby approximately 9 to 22% of the CH_4 emissions are related to temperature feedbacks (Ruddiman, 2006). Rising temperatures due to anthropogenic CO_2 and CH_4 forcing lead to a release of CH_4 from wetlands, this enhances the greenhouse effect and consequentially results in an additional release of CH_4 from wetlands.

Anthropogenic CO_2 emissions started 8000 years ago driven by deforestation in Europe to grow crops (Ruddiman, 2003). This leads to an increase in atmospheric CO_2 concentration of 40 ppm until the start of the industrial era (Fig. 2.2b), but only 9 ppm were caused by direct emissions (Ruddiman, 2006). The remaining 75% of the emissions were likely driven by a feedback between climate warming and the ability of the ocean to take up CO_2. At higher temperatures, the solubility of CO_2 in the ocean decreases and stratification increases, therefore less anthropogenic CO_2 can be taken up by the ocean.

The pre-industrial climate warming occurs on millennial timescales much longer timescales than the industrial climate warming. On these different timescales, the contribution and relevance of feedbacks for global temperature development can vary. The preindustrial anthropogenic emissions of CH_4 and CO_2 caused a net warming of 0.75K (Fig. 2.2c), similar to the industrial warming of 0.85K since 1850 (IPCC, 2013), but the release of anthropogenic CO_2 and CH_4 is much larger during the industrial time than during the pre-industrial time (Fig. 2.2a, b). This indicates that timescales matter

for the response of the climate system to an anthropogenic forcing. Earth system components react on different timescales and therefore different feedbacks are involved, for example processes in the deep ocean and ocean sediments act on millennial timescales in contrast to the atmosphere and the upper ocean, which react on much shorter timescales.

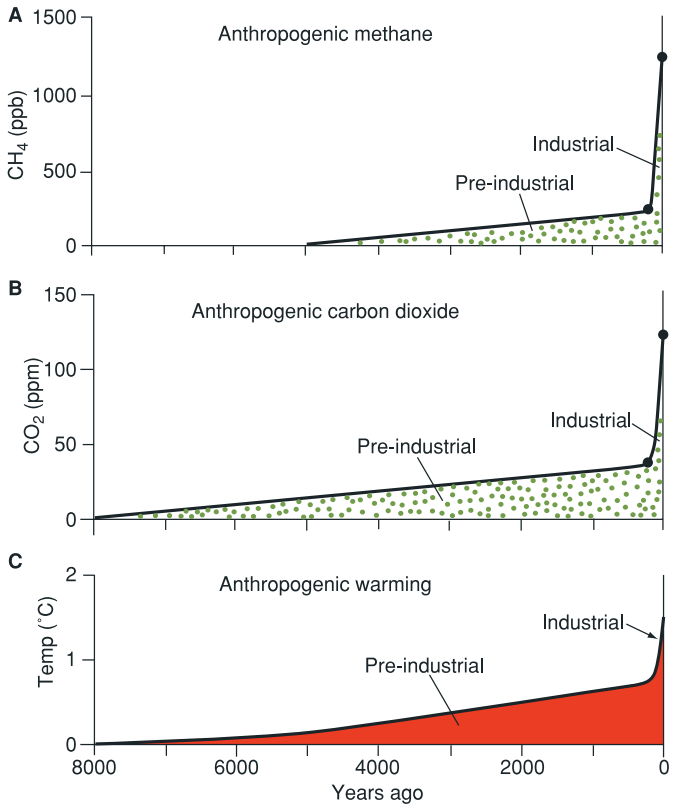

Fig. 2 Net anthropogenic contribution during the Holocene to (a) atmospheric CH_4 concentration, (b) CO_2 concentration, and (c) global mean temperature. Figure adapted from Ruddiman (2006).

1.2.1.1 A linear concept for climate feedbacks: Climate sensitivity, forcing and climate effect

Observations of greenhouse gas (GHG) concentrations and emissions are much better confined for the time after the industrial revolution. This contains estimates for CO_2, CH_4, N_2O, hydrofluorcarocarbons, perflurocarbons and other GHGs (Meinshausen et al., 2011). In current research, a large focus lies on the investigation of climate feedbacks due to increasing GHG concentrations and their effect on global temperature (ΔT). Anthropogenic GHG emissions perturb the radiation balance at the top of the atmosphere and lead to a change in radiative forcing (ΔR). Radiative forcing and global

temperature changes are often considered with a linear relationship scaled by climate sensitivity (λ):

$$\Delta T = \lambda \cdot \Delta R. \quad (1)$$

Different definitions and calculations for the climate sensitivities λ exist, for example the equilibrium and transient climate sensitivity (IPCC, 2013). The equilibrium (transient) climate sensitivity gives the response in global temperature to a forcing *R* on multi-century (decadal to century) timescales. The equilibrium response is smaller than the transient response, because some feedbacks react on much longer timescales (compare also to Fig. 2.2). The climate sensitivity parameter λ summarizes a large number of climate processes and feedbacks in one number, but obviously this is hard to obtain. Different components of the Earth system respond to anthropogenic forcing *R* at the same time.

Various climate models are used to determine λ as accurately as possible. Equilibrium climate sensitivity is likely in the range from 1.5 to 4.5°C for doubling of atmospheric CO_2 (IPCC, 2013). These large uncertainties are attributed to not fully understood climate feedbacks and climate forcings. Eq. (1) can be used as a simplified approach to assess the impact of human intervention on climate, limited to temperature change in response to increasing GHG concentrations until the end of the 21st century. This simplification helps to build a common basis for different disciplines of climate science (e.g. climate modelling, climate policy making and economic modelling), but there are also other feedbacks, beside climate feedbacks, relevant for human beings. This could be for example biogeochemical feedbacks affecting the marine ecosystems and the ocean oxygen state.

1.2.2 Model complexity and the representation of Earth system feedbacks

The growing complexity of climate models (Fig. 3) increased the numbers of feedbacks which models are able to simulate. In the very beginning simple zero- and one-dimensional energy balance models were used to explain and predict climate dynamics (Budyko, 1968), but these models could not simulate realistic meridional temperature profiles of the Earth. The establishment of computers in climate science led to a new generation of climate models, the so-called general circulation models (GCMs). In the beginning, ocean and atmosphere were modelled independently, followed by development of coupled atmosphere-ocean GCMs in the 80s (see Fig. 3). In GCMs, ocean and atmosphere dynamics are represented by a set of primitive equations. These equations conserve momentum, mass and energy for every grid cell in the atmosphere and in the ocean. GCMs are well suited to understand and model climate feedbacks caused by changes in water vapour, surface albedo and clouds. These and other feedbacks (introduced in Section 1.3), affect for example the response of the North African climate system to the irrigation and afforestation of the Sahara (case study one).

In the late 90s and in the beginning of the 21st century, biogeochemical processes were implemented in the so-called Earth System Models (ESMs). This includes representations of aerosol and dust processes, vegetation dynamics, a dynamic carbon cycle in the ocean, atmosphere and/or on land and other biogeochemical cycles. In this thesis the future ocean deoxygenation and its consequence for ocean anoxia are investigated (case study two) and therefore biogeochemical feedbacks only related to the ocean oxygen inventory are presented (see Section 1.5).

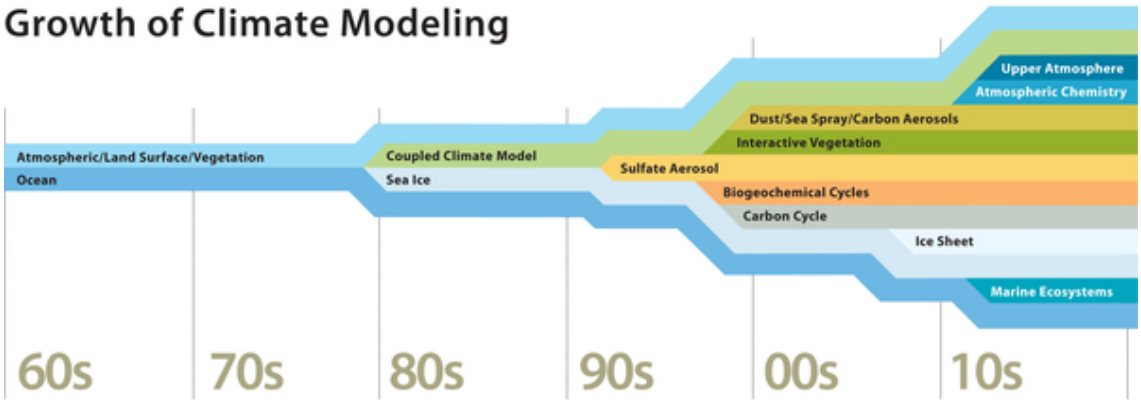

Fig. 3 Historical development of Earth system components, which are represented and simulated with climate models. Picture is used with kind permission from the University Corporation for Atmospheric Research (UCAR).

1.3 Atmospheric feedbacks in the North African climate system

This section will provide an overview of atmospheric feedbacks in the North African climate system, which could affect the afforestation and irrigation of the Sahara in a climate engineering scenario (first case study). The irrigated afforestation of the Sahara is proposed as a climate engineering measure for CO_2 removal, but also associated with substantial irrigation costs (Ornstein et al., 2009). The degree of self-sustainability of an artificial Green Sahara affects the required irrigation costs, therefore contributions of atmospheric feedbacks to the self-sustainability are analyzed in the first case study. The relevance of these feedbacks for the mid-Holocene Green Sahara are given in Section 1.4.

1.3.1 Vegetation albedo feedback or Charney feedback

Charney (1975) suggested a vegetation albedo feedback (Fig. 4) to explain circulation and precipitation dynamics in the North African climate system. The vegetation albedo is lower than the desert albedo. A larger vegetation cover would increase the surface temperature due to the absorption of shortwave (SW) radiation. Warmer temperatures result in more moist static energy, which could destabilize the atmospheric air column. In North Africa, this could affect the descending branch of the Hadley Cell and consequently affect precipitation strength and location of the West African Monsoon (Charney, 1975). More precipitation results in expanding vegetation and consequently leads to a positive feedback loop.

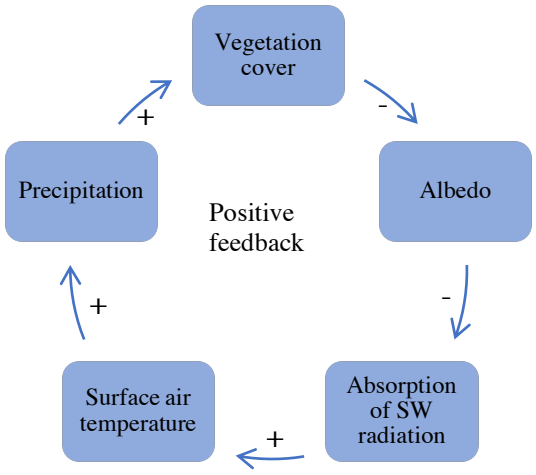

Fig. 4 The vegetation albedo feedback is triggered by changes in vegetation cover. Different albedos of bare soil and vegetation affect absorbed shortwave (SW) radiation and the surface air temperature. Low-level moist static energy increases (decreases) with higher (lower) surface air temperature and could lead to more (less) precipitation, which feeds back to vegetation cover.

1.3.2 Vegetation water recycling feedback

Regions with trees as vegetation can store a substantial amount of water. Evapotranspiration releases the stored water and leads to higher atmospheric moisture content than in deserts or grasslands. The increase in low-level moist static energy could destabilize the air column and result in local re-precipitation. This local precipitation could extend the length of the growing season and increase the vegetation cover as long the feedback is not interrupted by horizontal moisture advection. This so-called vegetation water recycling feedback (Fig. 5) could help to establish an artificial Green Sahara by recycling evaporated water and reducing irrigation costs.

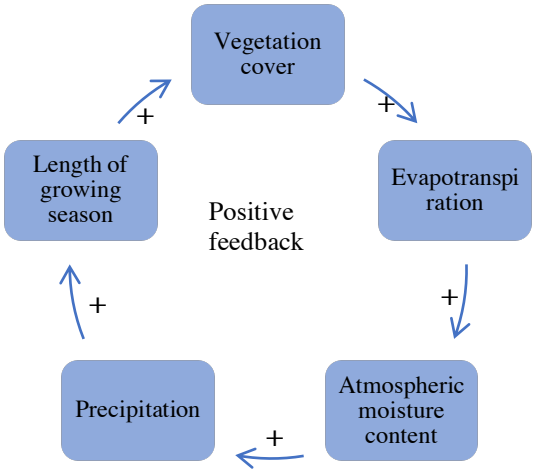

Fig. 5 Vegetation water recycling feedback: Direct local water recycling by precipitation of evaporated water could promote growth of vegetation and the vegetation cover.

The effectiveness of local water recycling can depend hereby on many different aspect, for example the location of the vegetation. Zhang et al. (1996) found that local water recycling is important in the Amazon Basin, but less in Southeast Asia or in tropical Africa. In the Sahara the water recycling feedback played a minor role for precipitation during the early- to mid-Holocene (Rachmayani et al., 2015). Instead, soil moisture was more important to influence circulation dynamics in North Africa and effect precipitation as described in the next subsection.

1.3.3 Vegetation circulation feedback or soil moisture feedback

The vegetation circulation feedback (Fig. 6) interacts between vegetation and the African Easterly Jet (AEJ). The AEJ is part of the zonal jets system over North Africa. Position and strength of the AEJ affects precipitation over the Sahara and the Sahel zone. The AEJ transports moisture off the continent, so that a weaker AEJ would result in mid-tropospheric moisture convergence and a positive precipitation anomaly (Cook, 1999). The AEJ is driven by the positive meridional temperature gradient between the Sahara and the Sahel zone via geostrophy and the thermal wind equation.

The vegetation circulation feedback affects the strength of the AEJ and is most efficient, when the vegetation change appears north of the AEJ (18°N) in North Africa (Patricola and Cook, 2008). Enhanced coverage of vegetation in the Sahara cools the surface by enhanced latent heat fluxes. This reduces the meridional temperature gradient and the strength of the AEJ. A weaker AEJ reduces the moisture divergence over the Sahara and potentially increases precipitation.

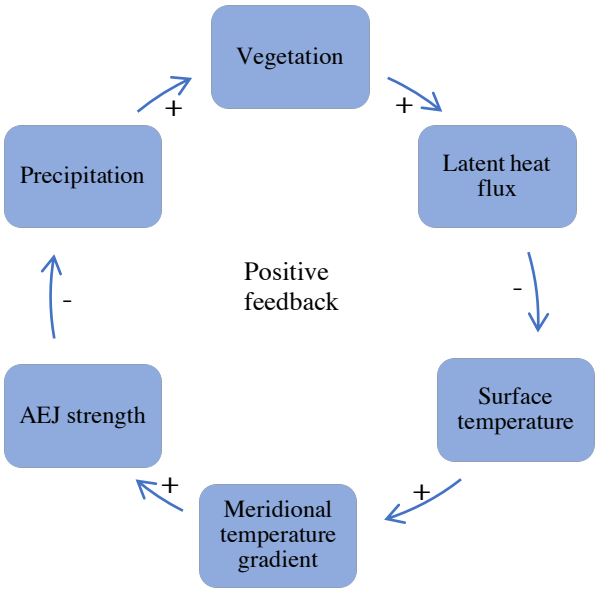

Fig. 6 The vegetation circulation feedback is described by a complex interplay between vegetation and the African Easterly Jet (AEJ) (details see text). This feedback is primary restricted to areas north of the AEJ in North Africa.

1.3.4 Dust precipitation feedback

Reduction in dust coverage over North Africa could promote precipitation in the Sahara due to a dust precipitation feedback (Fig. 7). Strong dust emissions occur in a dry bare-soil region like the Saharan desert. The dust precipitation feedback is triggered by increasing vegetation cover. Increased vegetation cover reduces surface wind speeds and the wind exposed soil areas. Less atmospheric dust reduces scattering of SW radiation, which warms the surface. As a result, moist static energy increases in the lower troposphere, thereby promoting precipitation and vegetation growth. Model simulations show that dust reduction during the mid-Holocene could have led to a 500 km northward expansion of the West African Monsoon (Pausata et al., 2016). However, the representation of the dust cycle in North Africa is subject to considerable biases (Parajuli et al., 2016) and more detailed evaluation of dust processes is needed until reliable predictions can be done.

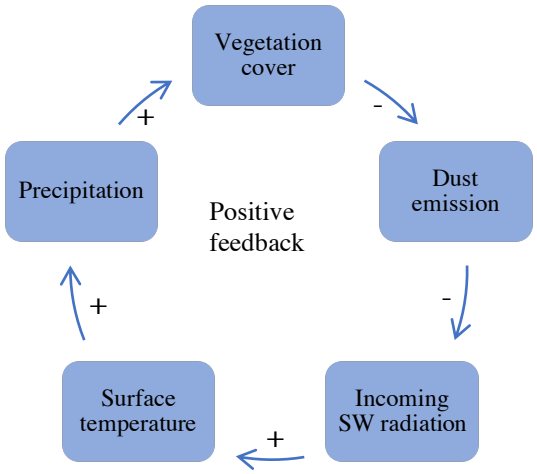

Fig. 7 The dust precipitation feedback is triggered by an increase in vegetation cover. Dust emissions are reduced in areas, where vegetation replaces bare soil areas or grassland. Less atmospheric dust reduces scattering of shortwave (SW) radiation and warms the Earth surface. Low-level moist static energy increases with higher surface air temperature and could lead to more precipitation, which feeds back to vegetation cover.

1.3.5 Water vapor feedback

Water vapor as a greenhouse gas increases surface air temperature in a positive feedback loop (Fig. 8). A positive water vapor anomaly in the atmosphere affects the radiative forcing of the atmosphere. Water vapor absorbs longwave radiation from the Earth surface and reemits half of it back to the Earth surface. Consequentially, surface air warms and increases the saturation vapor pressure by approximately 7% per Kelvin as derived from the Clausius-Clapeyron relationship. Enhanced evaporation closes the feedback loop and leads to more moisture content in the atmosphere. This feedback is generally analyzed for climate warming scenarios (Held and Soden, 2000) and works best for ocean areas where no water limitation appears.

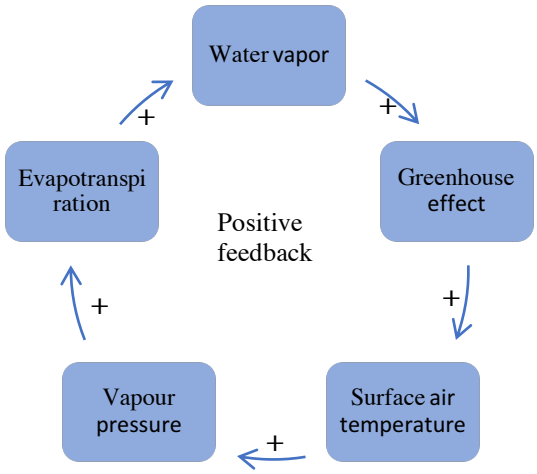

Fig. 8 Water vapor feedback: Climate warming or irrigation as anthropogenic water vapor source can initiate this feedback. More water vapor in the atmosphere enhances the greenhouse effect and warms the surface and surface air temperature. Warmer air can hold more water vapor, thereby promote evapotranspiration. This amplifies the initial change and is therefore a positive feedback.

1.3.6 Cloud feedback

Clouds have a warming effect on the surface by absorption and reemission of longwave (LW) radiation and a cooling effect by reflecting incoming shortwave (SW) radiation. The net effect of clouds depends on the sum of the LW and SW forcing radiation. Low clouds act to cool the surface due to the reflection of SW radiation, whereas high clouds lead to warmer surface temperatures. Reflection of SW radiation of high clouds is less effective than the absorption of LW radiation and hence the greenhouse effect is enhanced (Liou, 2002). The radiative forcing of clouds could also interact with the water vapor feedback (see Fig. 9). On a global scale, radiative forcing of clouds significantly enhances the water vapor feedback (Hall and Manabe, 1999), but regionally a change in cloudiness could lead to positive or negative cloud feedbacks. The example for cloud feedbacks presented here does not describe all possible interactions of clouds with the climate system. Scientific discussion about cloud feedbacks is still controversial, but an inter-comparison project started recently (Webb et al., 2017) to give a more complete picture about cloud processes and related feedbacks.

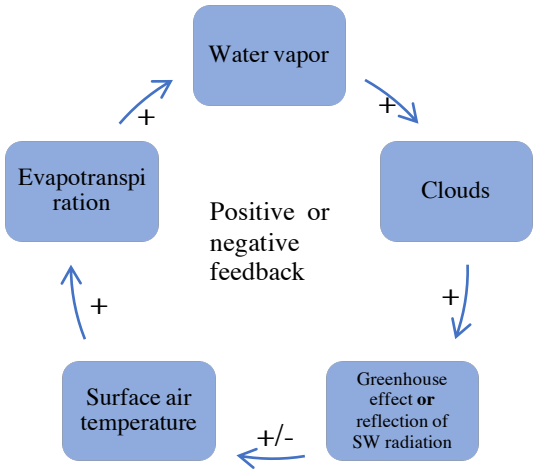

Fig. 9 Cloud feedback: Cloud radiative processes are integrated into the water vapor feedback (Fig. 8), which represents one possible cloud feedback among others. The sign of the feedbacks depends on net effect of the clouds on the surface temperature (details see text).

1.4 Mid-Holocene and artificial Green Sahara: Self-sustainability and feedbacks

It appears promising that, compared to today, the Sahara was once probably much greener during the mid-Holocene (circa 10000-5500 before present, e.g. Prentice and Jolly, 2000). Atmospheric feedbacks were important to establish a Green Sahara during the mid-Holocene. During the mid-Holocene, orbital forcing acted as a trigger for rapid climate change initiating vegetation feedbacks to drive the Sahara from a green into a desert state (Claussen et al., 1999). Similarly, in a climate engineered Green Sahara the irrigation could be the trigger to establish an artificial Green Sahara, but atmospheric

feedbacks could act differently under present-day environmental conditions than under mid-Holocene environmental conditions.

Nowadays climate models have still difficulties to simulate a Green Sahara, and scientist are debating since a long time about the role of feedbacks to sustain a Green Sahara during the mid-Holocene. The importance of atmospheric feedbacks for climate and climate transitions in the Sahara during the mid-Holocene were shown in previous studies (Charney, 1975; Levis et al., 2004; Patricola and Cook, 2008; Swann et al., 2014; Rachmayani et al., 2015; Pausata et al., 2016). Charney (1975) suggested the vegetation albedo feedback to explain the stable Green Sahara state. This feedback benefits from large albedo differences. However, in the mid-Holocene the bare soil in North Africa was wetter and darker than today and therefore the vegetation albedo feedback played a minor role for the Green Sahara state (Wang et al., 2008). This is corroborated by studies by Patricola and Cook (2008) and by Rachmayani et al. (2015), who suggested that the vegetation circulation feedback contributed more to precipitation in the Sahara than the negligible contributions of the albedo vegetation and the water recycling feedbacks. A more recent study proposed the dust precipitation feedback as another feedback to sustain a Green Sahara during the mid-Holocene (Pausata et al., 2016). However, general environmental conditions were different during the early- and mid-Holocene than today. Orbital parameters and expanded forests in Eurasia contributed to the self-sustainability of a Green Sahara (Swann et al., 2014). The larger forest cover triggered a remote circulation feedback by warming the Northern Hemisphere, which leads to a northward shift of the ITCZ.

The type of vegetation cover of the artificial Green Sahara differs substantially to the vegetation of the Sahara during the mid-Holocene. A climate engineered Sahara would consist of dense vegetation afforested with fast growing trees in contrast to a mid-Holocene Green Sahara. In the mid-Holocene the Green Sahara was steppe and savanna with scrub and sparse tree cover (Prentice and Jolly, 2000).

Under these circumstances a reevaluation of atmospheric feedbacks is necessary to evaluate their potential to establish an artificial Green Sahara (which is done in Chapters 2 and 3). Research questions and model configuration is given in Section 1.7. Before this, the second case study is introduced.

1.5 Biogeochemical feedbacks related to the ocean oxygen inventory

This section provides an overview of biogeochemical feedbacks, which could affect the ocean oxygen inventory on millennial timescales. These feedbacks are investigated in the second case study, because the strength and sign of these feedbacks could determine, if anthropogenic climate change could drive the ocean into an anoxic state. Ocean anoxia, or so called Oceanic Anoxic Events (OAEs), appeared already several times during the cretaceous era (from 145 to 66 Ma ago) (Schlanger and Jenkyns, 1976;

Jenkyns, 2010; Kidder and Worsley, 2010). The relevance of these feedbacks for OAEs during the cretaceous era are given in Section 1.6.

1.5.1 Oxygen productivity feedback

Ocean phosphate (PO_4) is the ultimate limiting nutrient in the ocean and determines productivity of marine organic matter on longer timescales (Tyrrell, 1999). An increase in oceanic PO_4 by weathering or other processes would stimulate marine productivity. A fraction of the newly formed organic matter is exported to the deep ocean. Bacteria transform the exported organic matter in an oxygen consuming process into dissolved nutrients and CO_2. This could drive an expansion of suboxia, which affects redox dependent benthic fluxes of PO_4. Low levels of oxygen lead to a preferential regeneration of PO_4 from organic matter and release of PO_4 from for example ferric oxyhydroxides (Ingall and Jahnke, 1994; Van Cappellen and Ingall, 1994). This results in a decreased burial efficiency of phosphorus and enhanced level of oceanic PO_4, which is one important feedback (Fig. 10) for the development of former OAEs (Mort et al. 2007b; Flögel et al. 2011). It could be also important for a development of an anthropogenic OAE (Palastanga et al. 2011; Niemeyer et al. 2017).

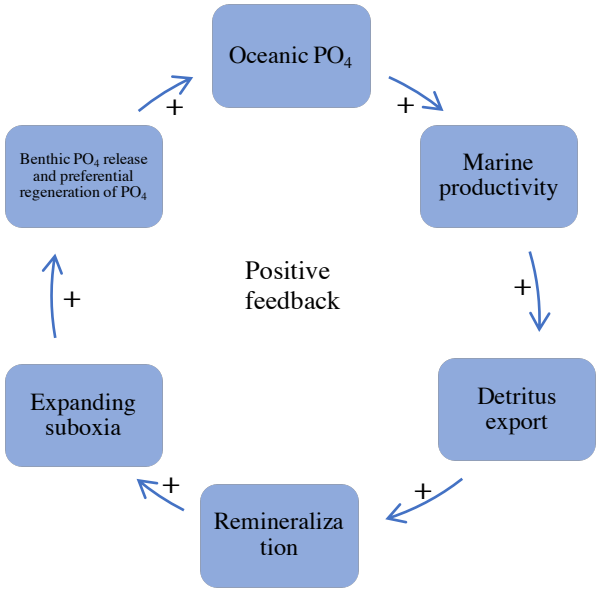

Fig. 10 The oxygen productivity feedback establish high concentrations of phosphate in the ocean. Ocean sediments with low oxygen supply promote redox conditions preferable for benthic PO_4 release and a low burial efficiency for organic bound PO_4. Possible triggers are enhanced weathering fluxes of phosphate or expanding suboxia in a warming climate.

1.5.2 Oxygen denitrification feedback

Nowadays PO_4 is supposed to be the ultimate limiting nutrient, as it limits marine productivity globally on long time scales, while nitrate limits marine productivity locally, and on shorter timescales (Tyrrell, 1999). Continuing from the oxygen

productivity feedback with its enhancement of marine productivity and enlarged suboxia, an oxygen denitrification feedback (Fig. 11) could develop. Enlarged suboxia increase the loss of nitrate due to denitrification. If nitrogen fixers are not able to balance this loss, the global ocean will become more nitrate limited, which could again hamper the expansion of suboxia. A recent study shows, that fixed nitrogen stimulation by denitrification in the same area could lead to a net runaway N loss feedback related to stoichiometric constraints of denitrification (Landolfi et al. 2013). However, the deoxygenation of the global ocean also depends on the ability of nitrogen fixers to close the newly developing gap of nitrate loss due to denitrification.

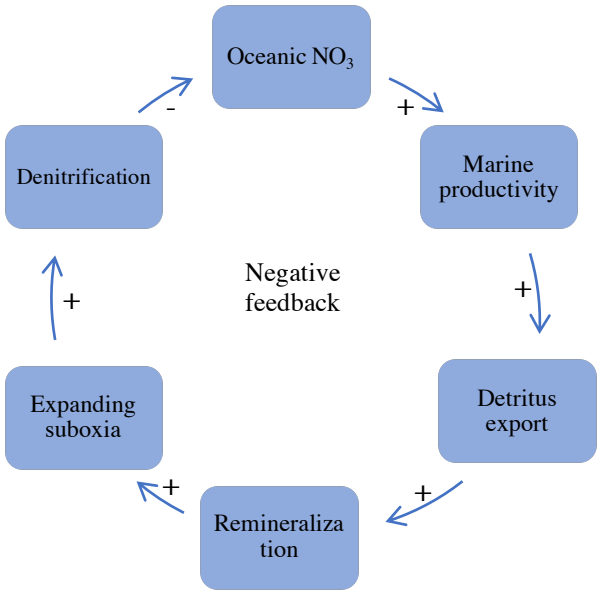

Fig. 11 The negative oxygen denitrification feedback is closely related to the oxygen productivity feedback and could limit this feedback by nitrate limitation. Expanding suboxia would lead to denitrification and a loss in nitrate, if it is not balanced by nitrogen fixers.

1.5.3 Phosphate burial feedback

The phosphate burial feedback (Fig. 12) does not directly affect oxygen levels, but it could affect the CO_2 forcing and duration of an OAE. For example, the duration of the cretaceous OAE 2 was approximately of the dimension of 100 ka. Enhanced marine productivity leads to enhanced burial of organic carbon, which reduces again atmospheric CO_2 concentration and global temperature. Reduced rates of PO_4 weathering would bring back the global ocean at some time to an equilibrium of the PO_4 inventory. During the last OAE2 enhanced productivity and a better preservation of organic matter are supposed important factors to remove carbon and PO_4 from the oceanic reservoir and affect in the end atmospheric CO_2 concentrations (Mort et al., 2007a).

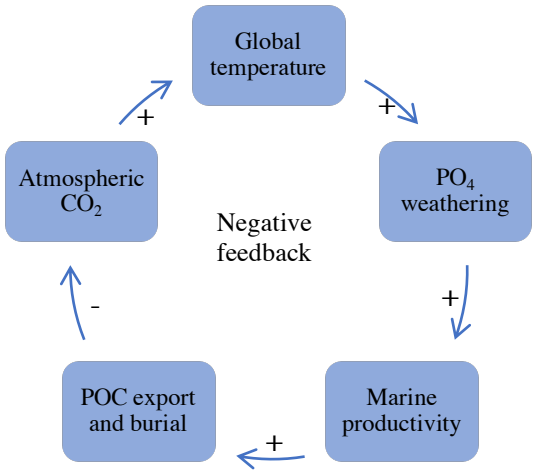

Fig. 12 The phosphate burial feedback could reestablish an equilibrium of the PO_4 fluxes. Enhanced burial of organic matter reduces the oceanic inventory of CO_2 and would lead to the removal of atmospheric CO_2 concentrations, colder global temperatures and cosenquentially to less PO_4 weathering.

1.6 Palaeo perspective: Oceanic anoxic events during cretaceous

In the cretaceous era (145 to 66 Ma ago) several OAEs appeared with durations in the range of 100 ka to 1 Ma. Crust activity led to enhanced CO_2 outgassing (Jones and Jenkyns, 2001; Kidder and Worsley, 2012) and, as a consequence, to high atmospheric CO_2 concentrations. CO_2 concentrations between 1000 to 3000 ppmv are suggested as a trigger of OAEs (Damsté et al., 2008; Méhay et al., 2009; Bauer et al., 2016). During OAE a warmer climate led to an enhanced supply of nutrients like phosphate (Blättler et al., 2011; Pogge von Strandmann et al., 2013), which increases the P inventory and could have led to the previously described oxygen productivity feedback (Fig. 10) (Monteiro et al., 2012). After the onset of the OAE, low-oxygen conditions enhance the recycling of P from the sediments and help to maintain high levels of productivity in the ocean (Van Cappellen and Ingall 1994; Mort et al. 2007b; Tsandev and Slomp 2009; Kraal et al. 2010). Under these high CO_2 concentrations and for large anoxia, limitation of ocean productivity could probably switch from P limitation to N limitation (Saltzman, 2005) and lead to the negative oxygen denitrification feedback (Fig. 11). This could have stimulated the enhanced nitrogen fixation (Kuypers et al., 2004).

Enhanced burial of organic carbon and PO_4 could return the Earth system into a climate state similar to pre-OAE conditions. Several processes could lead to the enhanced burial, for example a better preservation of organic material in anoxic sediments and higher marine productivity (Mort et al., 2007a), or a higher sea level, which enlarges the shelf areas, and increases burial of organic carbon on the shelf (Wallmann et al., 2016). However, environmental conditions were different during the cretaceous time in comparison to today. For example the present day bathymetry and circulation is different and climate warming is faster than during the cretaceous era. A reevaluation of these feedbacks is necessary to better predict the possible future oxygen state of the

ocean, which is done in Chapters 4 and 5. One has to consider hereby millennial timescales so that benthic and weathering fluxes can take effect.

1.7 Research Questions

This thesis investigates previously introduced feedbacks controlling state and transient development of two tipping elements for future climate scenarios in two case studies. The first tipping element is related to the vegetation state of the Sahara, with one stable state being a Green Sahara, and the other stable state a Desert Sahara. The second tipping element is related to the oxygen state of the global ocean one state, with a well oxygenated global ocean and only local oxygen minimum zones, in contrast to an ocean state with large scale anoxia. For the anoxic ocean state it is still questionable, if there are also states in between with large scale oxygen minimum zones (as proposed by Kidder and Worsley, 2012).

The simulations of the case studies are conducted under two future climate scenarios. In the Green Sahara case study, the NCAR's Community Earth System Model (Version 1.0.2) with a high-top atmosphere (CESM-WACCM) is used. CESM-WACCM is an atmosphere-ocean general circulation model, suitable to model atmospheric feedback in northern Africa. The dust cycle in CESM is still subject to large biases (Parajuli et al. 2016) and therefore dust concentrations are prescribed and not dynamically modelled. The Desert Green Sahara is simulated for present day environmental conditions and the artificial Green Sahara is simulated for a climate engineering scenario as an irrigated and afforested Sahara.

In the ocean anoxia case study, the Earth System Model (ESM) from the University of Victoria (UVic) Version 2.9 is used to conduct transient future climate projections for a business as usual scenario until year 5000. The UVic model is an Earth System Model of reduced complexity with a full carbon cycle and a Nutrient-Phytoplankton-Zooplankton-Detritus (NPZD) ocean biogeochemical model. Equations for simulating benthic fluxes and weathering of phosphorus are implemented in the UVic model to estimate their impact on productivity, remineralization and consequentially on the ocean oxygen state. An implemented sub-grid bathymetry improves the representation of benthic fluxes especially at the shelf and slope areas of the ocean. The simple one-layer atmospheric energy-moisture balance model reduces computational costs of the UVic model and makes it suitable for integrations of several thousand years.

Model simulations with CESM-WACCM and with the UVic ESM are conducted to address the following research questions:

1. Are atmospheric feedbacks able to sustain an artificial Green Sahara? And if not, to what extent is an artificial Green Sahara self-sustainable? What role do

the atmospheric feedbacks play in the self-sustainability of an artificial Green Sahara? (Chapter 2)

2. How does the artificial Green Sahara affect the tropical cyclone development? (Chapter 3)
3. Is it possible that anthropogenic climate change can drive the ocean anoxic on millennial timescales? How does phosphorus weathering and benthic phosphorus fluxes affect the development of ocean anoxia? What is the role of biogeochemical feedbacks in the development of future ocean anoxia? Does the oxygen-productivity feedback lead to a positive runaway feedback and turn the ocean anoxic? (Chapter 4)
4. What are the uncertainties for projection of phosphorus inventories and their consequences for the deoxygenation of the ocean? What role plays representation of the bathymetry, anthropogenic phosphorus fluxes and nitrate limitation for the deoxygenation of the ocean? (Chapter 5)

1.8 Author contribution

In this section the contribution of the different authors to Chapters 2, 3, 4 and 5 are listed.

Chapter 2 is based on the publication: Kemena, T. P., Matthes, K., Martin, T., Wahl, S., and Oschlies, A. (2017), Atmospheric feedbacks in North Africa from an irrigated, afforested Sahara. Clim Dyn., doi: 10.1007/s00382-017-3890-8.

T. P. Kemena initiated the study. T. P. Kemena, K. Matthes, A. Oschlies and S. Wahl conceived and designed the experiments. T. P. Kemena implemented the model code modifications. T. P. Kemena and S. Wahl performed the experiments. T. P. Kemena performed the analysis and produced all figures. T. P. Kemena wrote the manuscript with contributions from K. Matthes, T. Martin and A. Oschlies.

Chapter 3 is a manuscript in preparation by Kemena, T. P., Martin, T., Matthes, K., and Oschlies, A., Consequences of an Irrigated, Afforested Sahara on the Development of Tropical Cyclones in the North Atlantic in recent and in future climate, to be submitted to Geophysical Research Letters.

T. P. Kemena initiated the study. T. P. Kemena, T. Martin, K. Matthes and A. Oschlies conceived and designed the experiments. T. P. Kemena performed the experiments, performed the analysis and produced all figures. T. P. Kemena wrote the manuscript with contributions from T. Martin, K. Matthes and A. Oschlies.

Chapter 4 is based on the publication: Niemeyer, D., Kemena, T. P., Meissner, K. J., Oschlies A. (2017), A model study of warming-induced phosphorus–oxygen feedbacks in open-ocean oxygen minimum zones on millennial timescales. Earth Syst Dyn 8:357–367. doi: 10.5194/esd-8-357-2017. A. Oschlies, T. P. Kemena and K. J. Meissner initiated the study. T. P. Kemena and A. Oschlies conceived and designed the experiments. T. P. Kemena implemented the model code modifications. T. P. Kemena performed the experiments. D. Niemeyer performed the analysis and produced all figures with contributions from T. P. Kemena. D. Niemeyer wrote the manuscript with contributions from T. P. Kemena, K. J. Meissner and A. Oschlies. The publication is based on a master thesis from D. Niemeyer under supervision from A. Oschlies and mentoring from T. P. Kemena.

Chapter 5 is a manuscript in preparation by Kemena, T. P., Oschlies, A., Wallmann, K., Koeve, W., Landolfi, A. and Dale, A., Ocean phosphorus inventory and oceanic

deoxygenation: Large uncertainties in future projections on millennial timescales, to be submitted to Earth System Dynamics Discussions.

T. P. Kemena and W. Koeve initiated the study. T. P. Kemena, A. Oschlies and K. Koeve conceived and designed the experiments. T. P. Kemena implemented the model code modifications, performed the experiments, performed the analysis and produced all figures. T. P. K. wrote the manuscript with contributions from A. Oschlies, K. Wallmann, W. Koeve, A. Landolfi and A. Dale.

2. Atmospheric Feedbacks in North Africa from an Irrigated, Afforested Sahara

Tronje Peer Kemena[1] • Katja Matthes[1,2] • Thomas Martin[1] • Sebastian Wahl[1] • Andreas Oschlies[1,2]

Abstract

Afforestation of the Sahara has been proposed as a climate engineering method to sequester a substantial amount of carbon dioxide, potentially effective to mitigate climate change. Earlier studies predicted changes in the atmospheric circulation system. These atmospheric feedbacks raise questions about the self-sustainability of such an intervention, but have not been investigated in detail.

Here, we investigate changes in precipitation and circulation in response to Saharan large-scale afforestation and irrigation with NCAR's CESM-WACCM Earth system model.

Our model results show a Saharan temperature reduction by 6 K and weak precipitation enhancement by 267 mm/yr over the Sahara. Only 26% of the evapotranspirated water re-precipitates over the Saharan Desert, considerably large amounts are advected southward to the Sahel zone and enhance the West African monsoon (WAM).

Different processes cause circulation and precipitation changes over North Africa. The increase in atmospheric moisture leads to radiative cooling above the Sahara and increased high-level cloud coverage as well as atmospheric warming above the Sahel zone. Both lead to a circulation anomaly with descending air over the Sahara and ascending air over the Sahel zone. Together with changes in the meridional temperature gradient, this results in a southward shift of the inner-tropical front. The strengthening of the Tropical easterly jet and the northward displacement of the African easterly jet is associated with a northward displacement and strengthening of the WAM precipitation.

Our results suggest complex atmospheric circulation feedbacks, which reduce the precipitation potential over an afforested Sahara and enhance WAM precipitation.

Keywords:
Afforestation; Climate Engineering; Circulation; Irrigation; West African Monsoon

Tronje Kemena
e-mail: tkemena@geomar.de
[1] GEOMAR Helmholtz Centre for Ocean Research Kiel, Kiel, Germany
[2] Christian-Albrechts Universität zu Kiel, Kiel, Germany

2.1 Introduction

Afforestation is presently the only technically available climate engineering (CE) method to encounter climate change and is commonly associated with relatively low risk and low efficiency in comparison to other CE methods (Shepherd, 2009). Due to the low efficiency of afforestation, large-scale afforestation is necessary in order to have a significant impact on atmospheric CO_2, which implies a demand of large areas with enough seasonal rain to plant trees (Smith and Torn, 2013; Smith et al., 2016). These bio-productive areas are already widely utilized by agricultural industry. The land competition between food production and climate engineering effort could thus lead to negative impacts on food prices. To avoid this, an irrigated afforestation of deserts could be a favorable alternative.

Early studies (Kojima et al., 1995; Ozawa et al., 1995) proposed afforestation of deserts as one possible option to encounter climate change by carbon dioxide removal. More than 10 years later first studies discuss in detail the feasibility and effectiveness for the afforestation of the Sahara (Ornstein et al., 2009; Keller et al., 2014; Bowring et al., 2014). Ornstein et al. (2009) estimate that the irrigated afforestation of the Sahara as well as Australia would sequester enough CO_2 to balance global CO_2 emissions, but with the negative effect of major energy costs to pump and desalinate seawater.

Previous studies found that irrigated afforestation increases precipitation in the Sahara substantially (Ornstein et al., 2009; Bowring et al., 2014), and could thereby reduce energy costs for irrigation to make such a large-scale afforestation project more feasible. However, a detailed assessment of the atmospheric feedbacks induced by irrigated afforestation, which could explain changes in Saharan precipitation, is still lacking.

The North African climate system and in particular the Sahara region is strongly related to the West African Monsoon (WAM) dynamics. The WAM substantially drives seasonal and interannual variations in North African climate. During the WAM season from July to September the southwesterly winds transport moisture from the Atlantic into the continent driven by a meridional temperature gradient between land and ocean (Thorncroft et al., 2011). The moist southwesterly winds converge with the dry northeasterly winds originating in the Sahara to form the inner-tropical front (ITF). In contrast to oceanic regions, a surface wind convergence is not associated with a local precipitation maximum. The precipitation maximum of the WAM is determined by a maximum in air ascend throughout the troposphere, the location of the intertropical convergence zone (ITCZ), which is located between the African easterly jet (AEJ) and the tropical easterly jet (TEJ) (Nicholson, 2009). Precipitation patterns in North Africa are influenced for example by the location and strength of the ITCZ, AEJ, TEJ and the ITF.

Earlier studies suggested that droughts in the Sahel zone were connected to a meridional

southward displacement of the ITCZ (Kraus, 1977). A displacement of the ITCZ can be driven by cross-equatorial energy transports (Kraus, 1977), so that a warmer northern summer would lead to a northward displacement of the ITCZ and vice versa, in agreement with later studies (Broccoli et al., 2006; Devaraju et al., 2015; Swann et al., 2012; Swann et al., 2014). Regional temperature changes, for example in the Mediterranean Sea, could also play a key role (Park et al., 2016).

The zonal jets over North Africa are associated with strong wind shear and enhanced wave activity, which could trigger convection and precipitation (Nicholson, 2013). Grist and Nicholson (2001) determine dynamical processes shaping rainfall variability of the WAM in the Western Sahel zone. During wet (dry) years they found a stronger (weaker) TEJ and a weaker (stronger) and poleward (equatorward) displaced AEJ. Further, the meridional displacement of the AEJ is associated with a displacement of the WAM precipitation maximum in the same direction. A strengthening of the TEJ is typically connected with enhanced upper-level divergence of the meridional wind component, which could initiate enhanced low-level convection (Grist and Nicholson, 2001). In contrast to this, a strong AEJ is associated with a moisture divergence below the level of condensation, which could result in less WAM precipitation (Cook, 1999).

Self-sustainability is a looming issue in discussions that address the potential to establish a modern Green Sahara. It appears promising that, compared to today, the Sahara was once probably much greener during the entire early- and mid-Holocene (circa 10000-5500 before present, e.g. Prentice et al., 2000). Several studies suggest vegetation and dust feedbacks as key processes to establish a stable climate state with a Green Sahara. Lower surface albedo in the Sahara due to higher vegetation cover north of the ITCZ could lead to a northward shift of the Saharan desert, the so called Charney Feedback (Charney, 1975). Covering an area with vegetation would increase the surface temperature due to the absorption of shortwave (SW) radiation. Higher temperatures result in more moist static energy, what could destabilize the atmospheric air column and could affect precipitation strength and location of the ITCZ (Charney, 1975). More precipitation results in expanding vegetation and consequently leads to a positive feedback loop. This feedback benefits from large albedo differences. In the mid-Holocene the bare soil in North Africa was wetter and darker and therefore the vegetation albedo feedback played a minor role during this time (Wang et al., 2008), but for the drier present day conditions in the Sahara the feedback could be more important for afforestation efforts. During the mid-Holocene a vegetation circulation feedback was more relevant than the Charney feedback or local water-recycling to establish a Green Sahara (Patricola and Cook, 2007; Rachmayani et al., 2015). Enhanced vegetation leads to cooling by evapotranspiration, which weakens the AEJ and enhances precipitation in the Sahel zone and in the Sahara. The dust precipitation feedback could also help to sustain a Green Sahara. More vegetation cover reduces aeolian dust load, which promotes precipitation in the Sahara (Pausata et al., 2016). The dust could affect

incoming solar radiation or act as ice nuclei influencing cloud properties (DeMott et al., 2003). For example, precipitation can be suppressed by surface cooling due to scattering of short wave radiation by dust particles (Yu et al., 2015). Swann et al. (2014) conclude that the decrease in local albedo, appropriate orbital parameters and a remote circulation feedback due to expanded forests in Eurasia are relevant boundary conditions to sustain a mid-Holocene Green Sahara. Remote feedbacks of the Eurasian forests lead to a northward shift of the ITCZ (Swann et al., 2014). This remote feedback has also been found in present-day studies, where a large-scale afforestation (deforestation) in northern mid-latitudes leads to a local warming (cooling) and to a northward (southward) shift of the ITCZ (Swann et al., 2012; Devaraju et al., 2015).

For an assumed modern afforested Sahara orbital parameters and Eurasian forest cover differ from those of the early Holocene. The vegetation extend is larger and more dense in our afforestation scenario and therefore artificial irrigation is required. In case of afforestation a northward shift of the WAM region could reduce the required amount of irrigation. Ornstein et al. (2009) found seasonal precipitation from April to November in the Sahara with rates comparable to the present day WAM. Changes in the ITF could also affect Saharan precipitation. The location of the ITF is related to the Saharan heat low, which is further northward than the rain belt (Thorncroft et al., 2011) and associated with a shallow overturning (Nicholson, 2009). The overturning is shallow, because dry Saharan air holds low amounts of latent heat and therefore has less convection potential. A moistening of the Saharan air by enhanced evapotranspiration fluxes due to the afforestation could enhance the convection potential in the region of the ITF and, due to advection, also in the ITCZ. To summarize, the role of the ITF can change with the afforestation of the Sahara. Higher moisture availability due to anthropogenic moisture input from irrigation could change circulation patterns and precipitation in Northern Africa, because the meridional circulation plays a key role for the WAM precipitation (Thorncroft et al., 2011). On the other hand afforestation could lead to a net cooling at the surface due to enhanced evaporation (Bathiany et al., 2010; Betts, 2011), which could then again affect the ITF or the ITCZ. Under these different environmental conditions atmospheric feedbacks on precipitation in North Africa, for example due to changes in pattern, seasonality and strength of WAM precipitation, have to be reevaluated. This includes feedbacks related to changes in albedo, water cycle, moisture and near-surface energy fluxes.

Earlier studies focused more on efficiency to sequester atmospheric CO_2 (Ornstein et al., 2009; Keller et al., 2014) or feasibility by cost-benefit analysis (Bowring et al., 2014). Ornstein et al. (2009) recognized that the afforestation of the Sahara weakens the AEJ and enhances the TEJ, which could influence precipitation, but details are not further evaluated. Precipitation in the Sahara could contribute to the irrigation and would affect the feasibility of such a large-scale project. This study focuses on regional circulation and precipitation changes induced from an irrigation and afforestation of the

Sahara, and discusses atmospheric feedbacks on precipitation in more detail than any other study so far.

After an introduction of the experimental design in section 2.2, we provide the general effects on the water cycle as well as the radiation and energy budget in section 2.3. In section 2.4 effects on the WAM structure are presented and discussed in relation to atmospheric circulation feedbacks and its consequences for precipitation in the Sahara before the main results are discussed in section 2.5 and summarized in section 2.6.

2.2 Methods

2.2.1 The Model

We use the Community Earth System Model with high-top atmosphere (CESM-WACCM4), developed at the National Center for Atmospheric Research. CESM (Ver. 1.0.2) runs in a fully coupled model configuration with the Whole Atmosphere Community Climate Model (WACCM4) as the (high-top) atmosphere, the Parallel Ocean Program (POP2) coupled to the Community Ice CodE (CICE), and the Community Land Model (CLM4). WACCM4 is a superset of the Community Atmospheric Model version 4 (CAM4) and includes all physical parameterizations of CAM4. The model configuration CESM-WACCM4 participated in the Coupled Model Intercomparison Project Phase 5 (CMIP5) (Marsh et al., 2013).

The atmospheric model WACCM4 is a fully interactive chemistry-climate model which has been used independently in many studies of seasonal to decadal climate variability involving atmosphere-ocean interactions (e.g., Thiéblemont et al., 2015). The model domain extends from the Earth's surface to the thermosphere (5.1×10^{-6} hPa) and consists of 66 vertical levels (Garcia et al., 2007; Richter et al., 2010) on a horizontal latitude-longitude grid of 1.9°x 2.5°. The spatial resolution of WACCM4 is suitable to simulate reliable atmosphere-land interactions. WACCM4, with its high-top atmosphere, could resolve processes, related to the WAM due to a better representation of interactions between the lower stratosphere and the upper troposphere (Kafando et al., 2015).

POP2 and CICE are run on a 1°x 1° triangular horizontal grid with 60 vertical levels and are described in Holland et al. (2012) and Danabasoglu et al. (2012).

The land model CLM4 is coupled to the atmosphere and simulates biogeophysical processes like radiation interactions, momentum exchanges, turbulent fluxes, and heat transfer between atmosphere, vegetation and soil (Oleson et al., 2010; Lawrence et al., 2012). The hydrology module includes parameterizations for canopy interception, evaporation, infiltration, redistribution within the soil column, surface and subsurface runoff. An interactive biogeochemical module simulates vegetation and determines corresponding transpiration rates. Water for transpiration is provided by root extraction from the soil layers. The soil consists of 15 vertical layers from the surface to 50 m

depth (Oleson et al., 2010). CLM4 provides 15 Plant Functional Types (PFTs) to represent the individual properties of different vegetation groups with a prescribed distribution of PFT area fractions for every grid cell. At all times atmospheric CO_2 concentration and ozone depleting substances are set to constant 1960 conditions. Irrigation of the Sahara region (Fig. 2.1) is realized by the implementation of the interactive irrigation scheme from CLM4. An evaluation and a description of the CLM4 irrigation scheme can be found in Leng et al. (2013), a technical note can be found at the CESM homepage[1].

2.2.2 Experimental design

In this study we compare the results of an Afforested Sahara (AF) simulation to a Control (CTR) simulation. Each model simulation is conducted for 50 years. The first 20 years are taken as spin-up period and the subsequent 30 years are analyzed in the following, sufficient time span to focus on the tropics. For the complete simulation atmospheric CO_2 concentration is set to constant 1960 conditions, and aerosol as well as dust are prescribed as climatology from 1955. The spin-up period is sufficiently long enough to adapt the atmosphere to the afforestation in the AF simulation, which shows a negligibly small trend in global surface air temperature of +0.21 K/100 years, in the last 30 years.

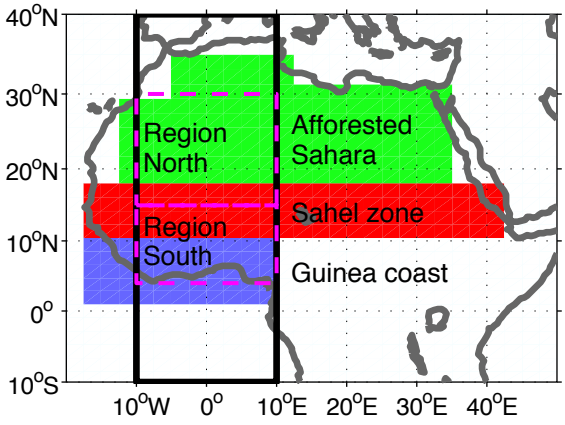

Fig. 2.1 Afforestation is applied in the Sahara (green). The Sahel zone (red) and the Guinea coast (blue) are shown as well. For this study we focus on the area of the black-framed box. Maximum meridional extend of the Sahara box is from 18°N to 33°N. Region North and South is depicted by the dashed-magenta-framed boxes.

Both experiments start from the same initial conditions with the exception that the AF experiment is initiated with a fully-grown tropical forest in the Saharan desert (see Figure 2.1 for the area under consideration). Initial conditions for the Saharan forest are taken from the tropical regions of Africa to reduce spin-up time. We apply TBET for the afforestation, which reaches largest net primary production, withstands high

[1] http://www.cesm.ucar.edu/models/cesm1.0/clm/CLMcropANDirrigTechDescriptions.pdf

temperatures and is able to store a substantial amount of CO_2 in stems and roots in comparison to shrub or grasses. Tropical trees require a continuous supply of moisture during all seasons. The irrigation is simulated by an interactive irrigation scheme described in the following subsection, which determines dynamic instead of constant prescribed irrigation rates. Irrigation is only applied in the afforested region.

2.2.3 Interactive Irrigation Scheme

The interactive irrigation scheme in CLM4 (Leng et al., 2013) determines irrigation rates for every grid point in the afforested region in the Sahara (Fig. 2.1). Whenever photosynthesis is limited by a water deficit, irrigation is applied until a target soil moisture level is reached. The target soil moisture level is determined by the irrigation factor, which linearly interpolates between the level of photosynthesis limitation and the level of moisture saturation. The irrigation factor is set to 70% similar to previous studies (Leng et al., 2013).

The irrigation is applied directly to the surface without interception by vegetation. The required amount of water is removed from the total liquid surface runoff. The surface runoff of every grid cell is assigned as a freshwater flux to ocean grid cells via the local river system. The irrigation scheme takes the required amount of water from the river runoff, but as the water of all African rivers is not sufficient to irrigate the entire Sahara, the irrigation algorithm leads to a negative river runoff (6.1×10^{12} m^3/yr). This amount of the additional required freshwater flux represents the required desalination effort and results in a salt flux into the ocean at the river mouths. Desalination plants are a proposed option to provide enough water for irrigation (Ornstein et al., 2009).

In the interactive irrigation scheme, the soil cannot take up all irrigated water immediately. This leads to an artificial surface runoff. In the following we only consider irrigation minus surface runoff to provide net water fluxes, in the following called effective irrigation or only irrigation.

2.3 Regional Afforestation Effects

In this section we investigate the regional Saharan feedback of the atmospheric and terrestrial hydrological cycle and of the atmospheric radiation budget to the irrigated afforestation of the Sahara. In the following section 2.4 we analyze how this regional changes are related to anomalies in the meridional circulation over North Africa and to precipitation anomalies of the West African Monsoon (WAM).

2.3.1 Temperature and Precipitation

The fully developed vegetation in the Sahara region changes the surface albedo and the moisture exchange between surface and atmosphere. The AF model run provides an afforestation-induced decrease in Saharan (average over the green box in Fig. 2.1) surface air temperature (SAT) of 6.3 K with some regional variation, i.e. slightly larger

cooling in the western Sahara with up to 8 K and less cooling in the eastern part of the Sahara with approximately 4 K (Fig. 2.2a). However, this local surface air temperature reduction has a negligible global net cooling effect of 0.04 K. The Saharan SAT anomalies also affect adjacent regions. A cooling can be found over the Mediterranean region, southern Europe, and the Sahel zone and a warming of 2 K can be depicted over the east Atlantic near the northwest African coast (Fig. 2.2a). Ornstein et al. (2009) derive a similar magnitude and spatial SAT distribution with a maximum decrease of 8 K in the West Sahara in the GISS climate model and Bowring et al. (2014) found a cooling by 7 K in winter and 10 K in summer. In contrast, Keller et al. (2014) found in a model with intermediate complexity, which neglects physical and dynamical processes in the atmosphere, a slight increase in SAT by approximately 0.5 K in the Sahara and adjacent regions through afforestation. The large differences in SAT in Keller et al. (2014) could be explained by the simplified representation of atmospheric processes in the UVic Earth system climate model with its 1-layer atmosphere.

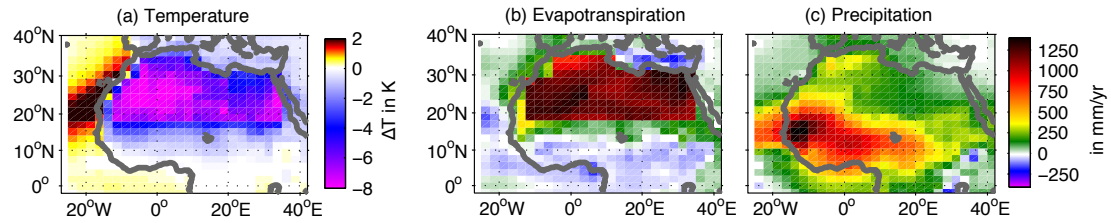

Fig. 2.2 Annual long-term (30-year) mean differences between the AF and the CTR experiments in (a) surface air temperatures in Kelvin [K], (b) evapotranspiration and (c) precipitation in millimeter per year (mm/yr).

The irrigation of the Sahara leads to a strong and uniform increase in evapotranspiration of 1186 mm/yr averaged over the Sahara and to a small positive remote effect on the evapotranspiration in adjacent regions (Fig. 2.2b). A substantial amount of the evaporated water is exported out of the Saharan region and precipitated over the Sahel zone, the coast of Guinea and the tropical Atlantic (Fig. 2.2c). The strongest increase in precipitation is located in the Sahel zone at the African west coast extending to the east and to the west. A smaller amount of the water directly re-precipitates over the Sahara. On average Saharan precipitation increases by 267 mm/yr with a relatively strong increase over the southwestern edge of the Sahara, a moderate increase in west Saharan areas of about 200 mm/yr and a weak increase in the east Sahara. Paleoclimate Modelling Intercomparison Project 2 (PMIP2) simulations show a similarly weak enhancement of precipitation not sufficient to sustain steppe in the Sahara in the mid-Holocene (Harrison et al., 2015). Claussen et al. (1999) found in their mid-Holocene simulations a stronger enhancement of precipitation in the Sahara by approximately 400 mm/yr (Claussen et al., 1999). These results are similar to our estimates, but smaller than those of earlier studies by Ornstein et al. (2009) and Bowring et al. (2014).

Ornstein et al. (2009) found an increase in precipitation by about 1000 mm/yr for about one half of the Sahara. Bowring et al. (2014) found an increase in Saharan mean

precipitation rates by 250 mm/year in the winter season and by 900 mm/year in the summer season, which are larger than our estimates with 35 mm/year for the winter season and 585 mm/yr for the summer season. We will later discuss these differences in precipitation between our and previous model results.

2.3.2 Saharan Radiation Budget

Changes in SAT, evapotranspiration and precipitation presented in Fig. 2.2 are related to changes in cloudiness and surface albedo, which directly affect the general radiation and heat budget. Both cloudiness and albedo affect the absorption of short-wave (SW) radiation at the surface and evapotranspiration increases the latent heat flux from the Sahara to the atmosphere.

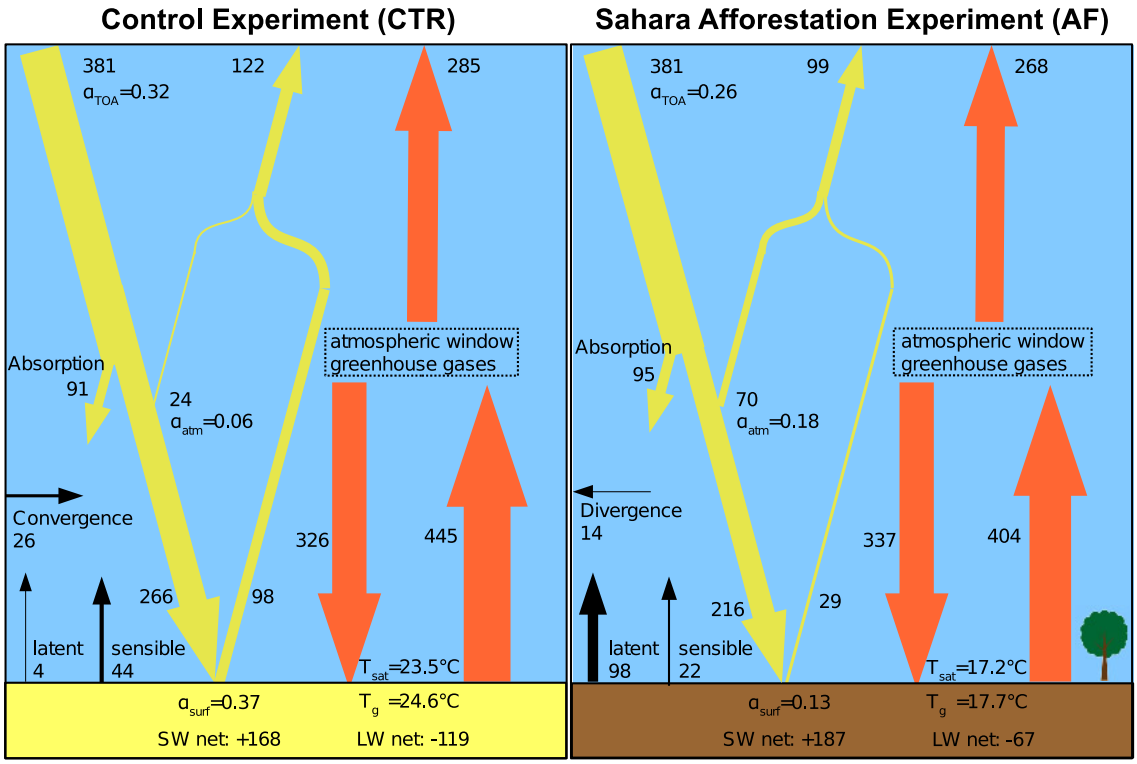

Fig. 2.3 Saharan radiation budget for the CTR (left) and for the AF experiment (right) as a 30-year annual average, fluxes are given in W/m^2. Yellow (red) arrows represent the budget for shortwave (longwave) radiation. Black arrows describe the latent, sensible heat fluxes and the heat flux divergence or convergence. The heat flux divergence and convergence is calculated as a residual of all other atmospheric heat fluxes. The figure includes also albedos (α) at the surface (α_{surf}), for the atmosphere (α_{atm}) and at the top of the atmosphere (α_{TOA}) and temperatures at the ground (T_g) and of the surface air (T_{sat}). For details see text.

The effects on the mean radiation budget of the Saharan region are summarized for the CTR and the AF experiments in Figure 2.3. The net SW radiation flux at the top of the atmosphere (TOA) is strengthened by 23 Wm^{-2} from the CTR (259 Wm^{-2}) to the AF experiment (282Wm^{-2}). This results from changes of the incoming SW radiation on its pathway to the surface in the AF experiment: atmospheric SW absorption increases slightly by 4 Wm^{-2} and the reflection of SW radiation in the atmosphere increases substantially by 46 Wm^{-2}, probably due to enhanced evaporation and atmospheric

moisture, which in turn enhances the cloud cover and atmospheric albedo (Fig. 2.3, α_{atm}). Less SW radiation reaches the surface in the AF experiment (216 Wm^{-2} as compared to 266 Wm^{-2} in the CTR experiment), but in combination with the adjusted surface albedo (Fig. 2.3, α_{surf}), the net SW absorption increases in the AF experiment by 19 Wm^{-2}.

The longwave (LW) radiation budget at the surface reflects the strength of the greenhouse effect and the equilibrium surface temperature. The AF surface temperature is shifted towards lower temperatures, i.e. 17.2°C, and therefore the local emission of LW radiation is reduced from 445 Wm^{-2} to 404 Wm^{-2}. The increase of atmospheric moisture results in an increase of reemitted LW radiation in the atmosphere by 11 Wm^{-2}.

In the AF experiment the irrigation substantially increases evapotranspiration and consequently the latent heat flux by 94 Wm^{-2}. The sensible heat flux into the atmosphere decreases from 44 Wm^{-2} in the CTR experiment by 50% to 22 Wm^{-2} in the AF experiment, because the temperature difference between soil (Fig. 2.3, T_g) and surface air (Fig. 2.3, T_{sat}) decreases from 1.1 K in the CTR to 0.5 K in the AF experiment.

The global atmospheric radiation budget is balanced by the latent and sensible heat flux. However, in the local budget the divergence of the atmospheric heat transport balances this budget. The heat flux convergence, calculated as the residual of all other atmospheric heat fluxes, of 26 Wm^{-2} in the CTR experiment changes into a heat flux divergence of 14 Wm^{-2} in the AF experiment. In general the afforestation in the Sahara leads to enhanced latent heat flux and a reduced surface temperature.

2.3.3 Soil and Atmosphere Water Budget and Self-Sustainability

A meaningful indicator for the self-sustainability of an afforested Sahara could be calculated from the Saharan soil to atmosphere moisture fluxes. The moisture exchange between the Sahara and the atmosphere is mainly driven by transpiration fluxes and therefore by the irrigation.

Figure 2.4 gives a summary of the local water budget of the Sahara for the CTR experiment (left) and the AF experiment (right). First we analyze how reasonable the irrigation rate in the AF experiment is and then compare the irrigation rate to other studies. According to the formulation of the irrigation scheme, irrigation is applied until a target soil moisture level is reached, whenever photosynthesis is limited by a water deficit. In the AF experiment an irrigation rate of 2625 mm/yr can be found in the Sahara where a large amount of the irrigated water is lost by drainage (65%). Such large loss by drainage were also found by Sacks et al. (2009), who applied the same irrigation scheme in CLM to agricultural lands on a global scale. However, observations support considerably lower loss rates, such as in field applications of irrigation methods in the

Murrumbidgee Irrigation Area in Southeast Australia (Ayars et al., 2006), where a drainage loss of only 6% and 0.05% for irrigation without and with a drainage reusing system was reported.

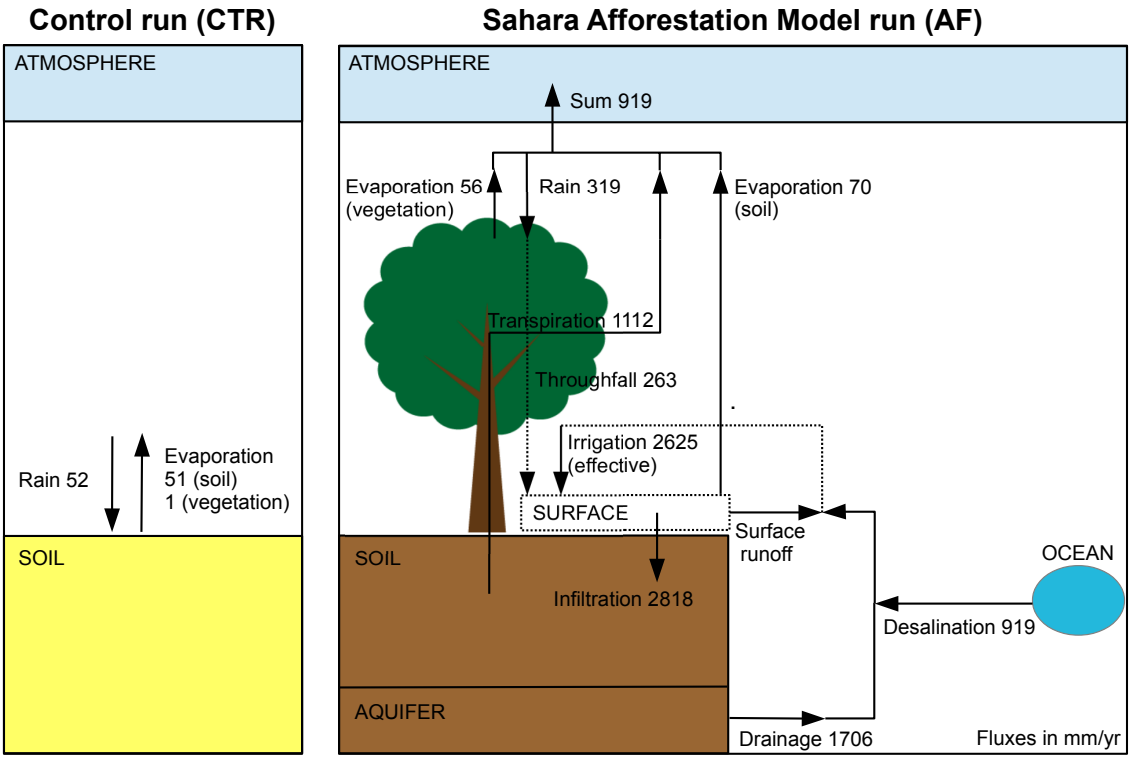

Fig. 2.4 Sahara water budget for the CLM of the control run (CTR) (left) and the afforested irrigated Sahara (AF) (right) as a 30-year annual average. All fluxes are in mm/yr averaged over the area of the Sahara (see black box in Fig. 2.1).

In the AF simulation 919 mm/yr (6.9×10^{12} m^3/yr) desalinated water is required to irrigate the Sahara, a value similar to the optimal 900 mm/yr found by Bowring et al. (2014). Bowring et al. (2014) prescribed different irrigation rates and found this optimal value under consideration of a cost-benefit analysis. Ornstein et al. (2009) estimate 1000 mm/yr precipitation and irrigation to provide enough water for Eucalyptus plantations in the Sahara.

In the arid climate of the Sahara, as simulated in CTR with a precipitation rate of 52 mm/yr, all precipitation evaporates directly back into the atmosphere and no water is stored in the soil. The precipitation increases in the AF experiment to 319 mm/yr, which is about half the precipitation experienced in central Europe and an order of magnitude larger than in the CTR run.

The balance between local precipitation and evapotranspiration is a good indicator for the self-sustainability of an afforested system. In our AF experiment evapotranspiration of 1238 mm/yr balances a precipitation of 319 mm/yr, thus only 26% of the deployed water is “recycled” regionally over the Saharan forest. The largest contribution to the total evapotranspiration (1112 mm/yr or 90%) originates from transpiration, the

remaining moisture flux is evaporation from the soil and from the vegetation. The difference between regional evapotranspiration and precipitation (919 mm/yr) has to be balanced by horizontal moisture flux by atmospheric advection to adjacent regions. Enhanced precipitation south of the Sahara could be obtained by advection fluxes from the Sahara (Fig. 2.2). This is in contrast to Ornstein et al. (2009), who derives a substantial amount of precipitation reprecipitating directly above the Sahara and increasing the degree of self-sustainability of the afforested Sahara. Furthermore they find a northward expansion of the West African Monsoon (WAM) into the Sahara region, whereas in our experiment the WAM precipitation mainly increases south of the Sahara, in the Sahel zone (Fig. 2.2c). We will present in the next section, why the WAM stays more likely south of the afforestation region.

2.4 Afforestation Effects on the West African Monsoon

2.4.1 Precipitation

The seasonal West African Monsoon (WAM) cycle starts with intense coastal rainfall near the Gulf of Guinea in April, and persists typically until the end of June (Fig. 2.5a). A secondary precipitation maximum develops near 10°N in the early summer. This meridional relocation of the precipitation maximum from the Guinean coast into the Sahel is the onset of the WAM over West Africa. The zonal mean between 10°W and 10°E gives a good estimate of the WAM characteristics as shown in the observations from the Tropical Rainfall Measurement Mission (TRMM[2], Huffman et al. (2007)) from 1998 to 2014 (Fig 2.5a).

In comparison to observations, the CTR experiment retrieves a distinct seasonal cycle in the meridional shift of the precipitation region from the southernmost maximum in May at around 5°S to the northern maximum around August at around 10°N (Fig 2.5b).

The maximum monsoon precipitation in the CTR experiment occurs in August with 8.5 mm/day similar to the maximum in the TRMM data with 9.1 mm/day. However, the meridional extent of the precipitation band is narrower in observations. The CTR experiment reproduces realistic monsoon rainfall rates and the seasonal cycle, but underestimates the intense coastal rainfall at 4°N in May and June.

In the CTR experiment, the coastal rainfall in May is located too far south, is too weak and appears one month too early in comparison to the TRMM data, which could probably be due to the warm bias in east Atlantic sea surface temperatures (Cook et al., 2012). This SST bias appears in many climate models and is responsible for a southward shift of the ITCZ and a related southward shift of precipitation in the East Atlantic (Richter and Xie, 2008). However, the representation of the WAM in the CTR

[2] http://trmm.gsfc.nasa.gov

experiment is comparable in amplitude and spatial structure to CCSM4 simulations with a finer horizontal (T85) resolution in Cook et al. (2012; their Fig. 2.1b).

The AF experiment with an afforested Sahara changes the seasonality, location and intensity of the WAM significantly (Fig. 2.5c). The summer maximum in precipitation is shifted by more than 400 km northward from 10°N to 14°N. The intensity increases by 48% to 12.6 mm/day in August and the 1 mm/day precipitation isoline reaches the northern Sahara. Irizarry-Ortiz et al. (2003) found for mid-Holocene simulations a slightly more northern precipitation maximum at 16°N peaking at a much weaker intensity of 0.25 mm/yr. In our simulation, the monsoon season in the Sahel zone is extended and starts already in April and the precipitation band still appears relatively broad similar to the CTR simulation. The precipitation patterns southward of the equator and at the Guinea coast are hardly affected by the irrigation.

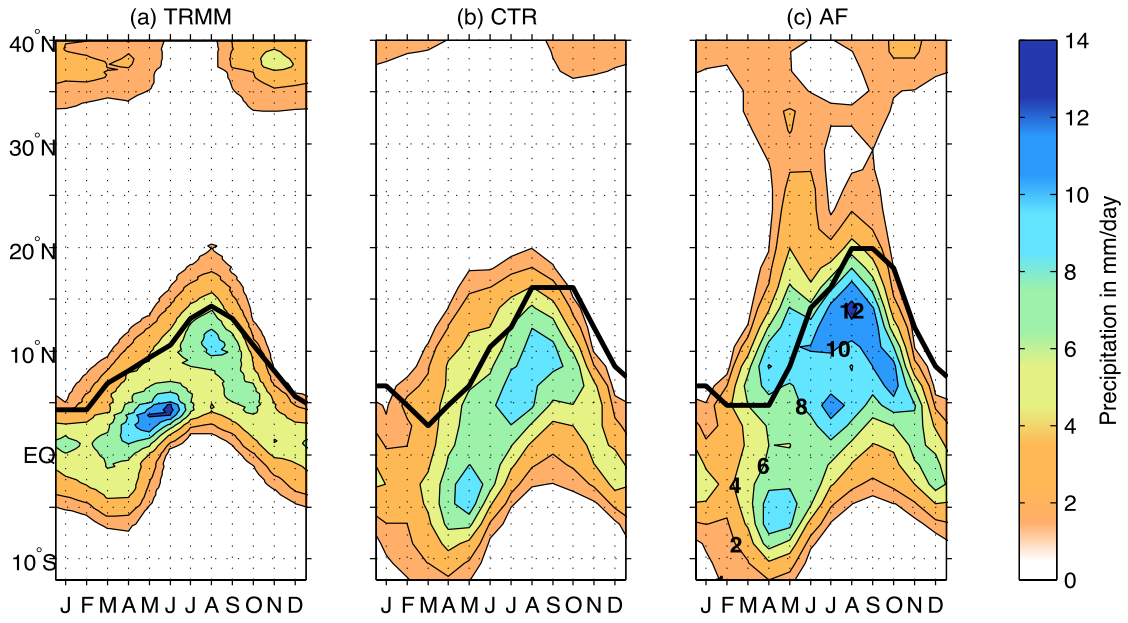

Fig. 2.5 Climatological seasonal cycle of precipitation averaged over the region of the West African Monsoon from 10°W to 10°E in mm/day for (a) the Tropical Rain Measuring Mission, (b) the CTR, and (c) the AF experiments. The black line indicates the position of the African Easterly Jet (AEJ) core calculated from MERRA (Rienecker et al. (2011); gmao.gsfc.nasa.gov/reanalysis/MERRA/) reanalysis data (a) and CESM-WACCM (b, c). The position and shift of the AEJ is discussed in section 4.4. MERRA and TRMM data cover the period January 1998 to October 2014. For the model data a 30-year average is performed.

2.4.2 Meridional Atmospheric Circulation

The meridional atmospheric circulation over northern Africa links processes over the Sahara, the coast of Guinea and the Sahel zone and plays an important role for the seasonality and regional patterns of precipitation over North Africa. Fig. 2.6 shows climatological averages of the meridional circulation averaged over the WAM area, in particular the vertical velocity (shading) as well as meridional winds (contours).

In January the local Hadley circulation is represented by ascending motion over the equator (negative values of the vertical velocity in Fig. 2.6a) and a broad zone with

descending motion (positive values in Fig. 2.6a) over North Africa in the CTR experiment (Fig. 2.6a). As air descends over the Sahara due to radiative cooling, the air is warmed adiabatically by compression, which consequentially leads to low values of relative air humidity. A stronger Hadley branch above the Sahara would lead to a further reduction in relative humidity, which could prevent the water vapor to condensate over the Sahara.

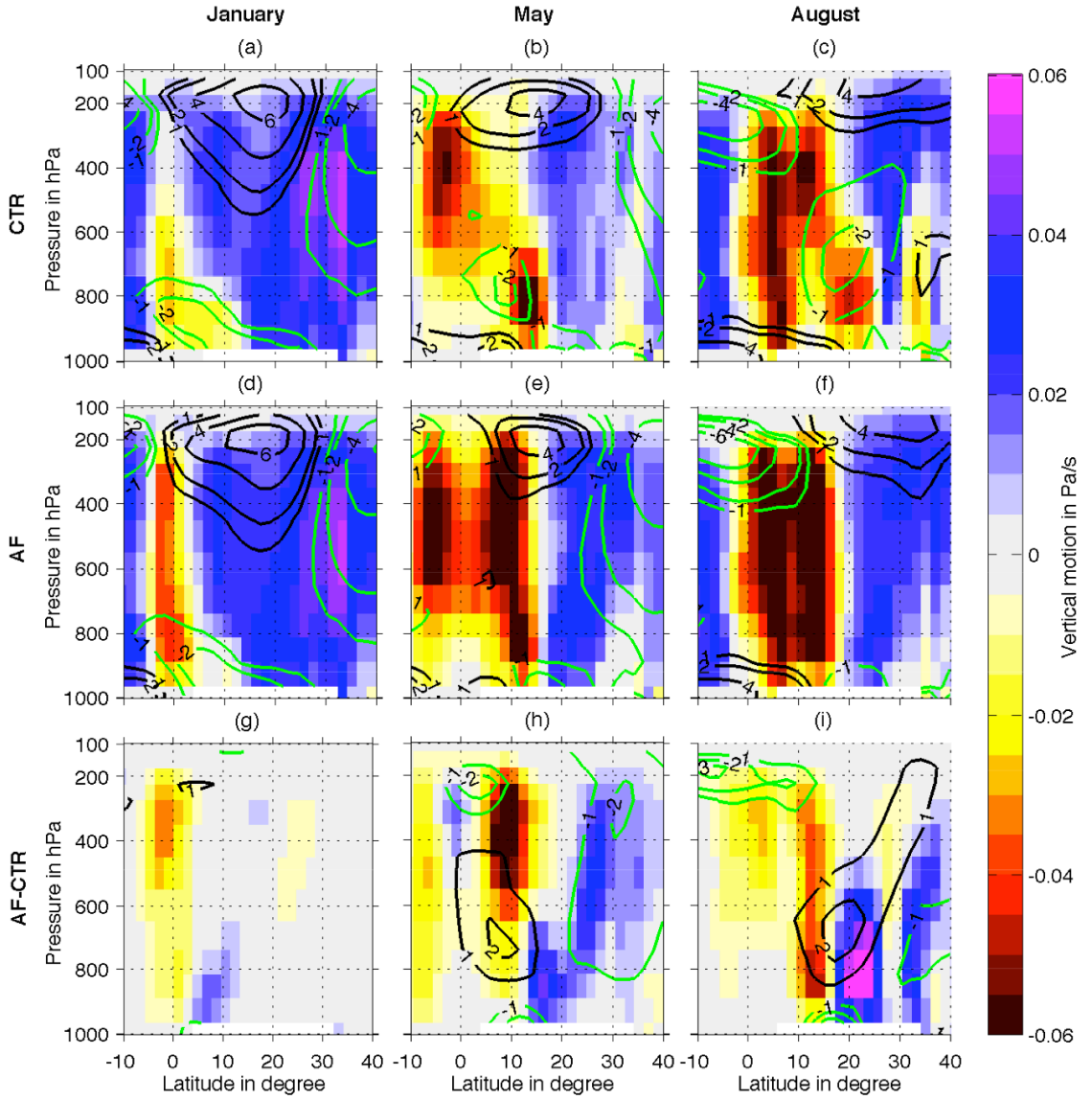

Fig. 2.6 Climatological 30-year averages of the meridional circulation averaged over the WAM area from 10°W to 10°E, shaded the vertical motion (red upward, blue downward) in Pa/s and in contours the meridional motion (green southward, black northward) in January, May and August for the CTR experiment (a-c), the AF experiment (d-f), and the differences between the AF and the CTR experiment (g-j).

In May the lower troposphere forms a shallow overturning cell ranging from the surface to 800 hPa and with northward surface winds until 14°N (Fig. 2.6b). At 14°N converging surface winds indicate the position of the inner-tropical front (ITF) (Fig. 2.6b). The simulated upward branch close to the equator (Fig. 2.6b) represents the

location of the rainbelt (see Fig. 2.5b), which is too far south compared to observations as already mentioned in the previous section.

Until August the ITF moves further northward and reaches 20°N (Fig. 2.6c), and marks the northward extend of the shallow overturning cell. During August two distinct upward branches appear: a northern one between 10°N and 15°N, strongest at the 400 hPa level which could be associated with the rainbelt of the WAM, in good agreement with the observed rainbelt close to 10°N (Nicholson, 2009). Nicholson (2009) shows that the position of the ITF does not coincide with the position of the upward branch in the upper troposphere, which agrees also with our results. The second upward branch in Figure 2.6c is located close to 5°N, which is not seen in observations in August. However, this is the location of the costal precipitation near the Guinea Coast, which occurs in observations during May (Thorncroft et al., 2011). This double structure of the upward branches is probably a model artifact and this could indicate that the precipitation is not able to migrate completely into the Sahel zone. Richter and Xie (2008) found that coupled general circulation models have a tendency to simulate double ITCZ in the eastern equatorial Atlantic, but with less influence on continental vertical motion. However, the structure of the shallow overturning cell in the Sahara and the upward branch in the Sahel zone is well represented in the CTR model run.

In the AF experiment, the large amount of additional humidity from the irrigated Sahara changes the atmospheric radiation and heat budget (Fig. 2.3, 2.4), which potentially affects the meridional circulation.

In January of the AF experiment, the equatorial upward motion of air increases, whereas the meridional circulation as compared to the CTR experiment is largely unchanged (Fig. 2.6d, g). In May the shallow overturning in the lower troposphere in the CTR experiment (Fig. 2.6b), is replaced by a deep upward branch centered at 8°N and a southward shift of the ITF to 10°N in the AF experiment (Fig. 2.6e). Both coincide with the strong precipitation maxima during May (Fig. 2.5c). A weak clockwise circulation anomaly with southward winds at the surface and northward winds at 800 hPa explains the vanishing of the shallow overturning cell. Additionally a counterclockwise cell in the upper troposphere above Guinea supports the strengthening of the upward branch (Fig. 2.6h).

The intensification of the deep upward branch continues in August in the AF experiment. Here, the ITF is shifted beneath the northern upward branch (Fig. 2.6f, i). Additional humidity is advected from the Sahara to the location of the ITF (Fig. A1 in the appendix A). The northern upward branch intensifies and leads to a stronger upper troposphere divergence (Fig. 2.6f). Below 500 hPa a clockwise circulation anomaly over the Sahara and the Sahel zone (Fig. 2.6i) develops in the AF experiment with descending air above the Sahara and ascending air above the Sahel zone. Similar to May the circulation anomalies and the strong upward motion promote local convection

and stronger monsoon precipitation, which is most prominent below the upward branch at 12°N (Fig. 2.5c).

We derive in the AF experiment a change in the structure of the monsoon circulation and hence monsoon precipitation. During the monsoon period, the ITF is shifted southward to the border between the Sahara and the Sahel zone and is now aligned to the meridional position of the monsoon precipitation. One reason for the ITF shift could be the temperature reduction in the Sahara (Fig. 2.2a), which shifts the surface temperature maximum from the Sahara into the Sahel zone. However, the displacement of the ITF, and its relation to the meridional circulation is more complex and will be examined next.

2.4.3 Meridional Circulation Feedbacks

The Hadley circulation of the tropical atmosphere is driven by the meridional gradient of diabatic heating, which is sustained by the gain due to latent heat flux and the loss due to radiative cooling. Changes in the meridional heating rate could affect the position and strength of the upward and downward branches of the Hadley cell. The impact of afforestation and irrigation on the atmospheric radiation budget are shown in Figure 2.7, here derived as anomalies in the net heating rates (Fig. 2.7a-c), as well as the longwave (LW) (Fig. 2.7d-f) and shortwave (SW) (Fig. 2.7g-i) components separately. Latent heating rates are not shown. In all seasons the anomalies of net heating rates in the lower troposphere show a warming in the south and a cooling in the north. Until August, the center of the anomalies moves further northward. However, these anomalies drive changes in the atmospheric meridional circulation. So in general a negative (positive) meridional gradient in the heating rate should drive a clockwise (counterclockwise) meridional circulation. A negative meridional gradient in the total heating rate appears at 850 hPa in May between 8°N and 20°N and in August between 14°N and 24°N (Fig. 2.7b, c).

The anomalies of the radiation budget are primarily driven by low-level LW radiation changes (Fig. 2.7d-f), with the strongest radiative cooling in August between 20°N and 30°N and a LW radiative heating driven by high-level clouds (Fig. A2 in the appendix A) between 10°N and 20°N. In contrast to this the SW radiation weakens this effect (Fig. 2.7g-h), which are driven by changes in cloud cover (Fig. A2 in the appendix A). The effect of different processes, e.g. cloud cover changes, on the heating rates will be examined next.

Figure 2.8 shows vertical profiles of temperature, cloud variables and heating rates to identify the driver of the negative meridional gradient in heating rates in Figure 2.7. Profiles are shown in May representative for the WAM season for two distinct regions, Region North and Region South (shown in Fig. 2.1, 2.7e). Region North is located between 15°-30°N and 10°W-10°E (Fig. 2.8, dashed lines), covers the Sahara and the

northern Sahel zone and is characterized by atmospheric low-level radiative cooling. Region South is located between 4°-15°N and 10°W-10°E (Fig. 2.8, solid lines), covers the southern Sahel zone and Guinea and is characterized by atmospheric low-level radiative warming. Furthermore Region South represents conditions of the upward branch of the Hadley circulation. The border between both regions (15°N) moves northward during the WAM season. Major driver of the negative meridional gradient in heating rates is the low-level radiative cooling in Region North (Fig. 2.8b) and high-level clouds in Region South (Fig. 2.8c).

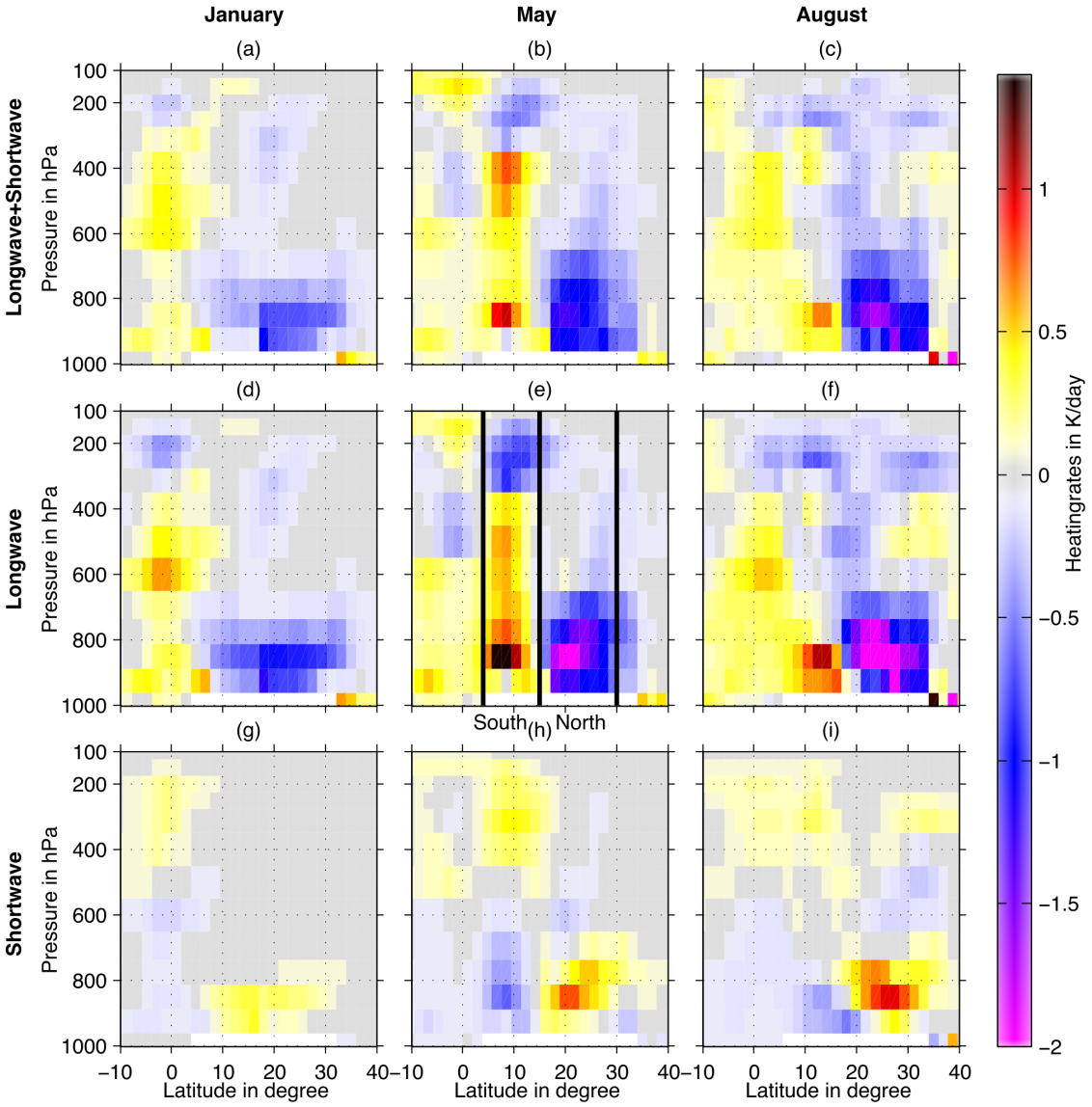

Fig. 2.7 Differences in mean heating rates in Kelvin per day (K/day) over the WAM area from 10°W to 10°E between the AF and the CTR experiment in January (a, d, g), May (b, e, h), and August (c, f, i) for the net heating rate (a-c), the long wave (LW) radiation (d-e), and the short wave (SW) radiation (g-i). The meridional extend of Region North and Region South are depicted in (e).

In Region North (Fig. 2.8, dashed lines) the change in the radiative budget is dominated by additional radiative cooling over the whole column, which is strongest at lower levels (Fig. 2.8a). Enhanced land to atmosphere moisture fluxes lead to a significant

increase in the humidity below 600 hPa (Fig. 2.8e), and to a substantial increase in the emission of LW radiation (Fig. 2.8a). This results in a strong radiative cooling of -1.3 Kelvin per day (K/d) at 850 hPa (Fig. 2.8a) and a reduction in the air temperature in the lowest atmospheric layer by 6.7 K (Fig. 2.8d). In the lower atmosphere cloud fraction (Fig. 2.8c) and moisture (Fig. 2.8f) increase, which slightly weaken the radiative cooling effect due to the absorption of SW radiation (Fig. 2.8a).

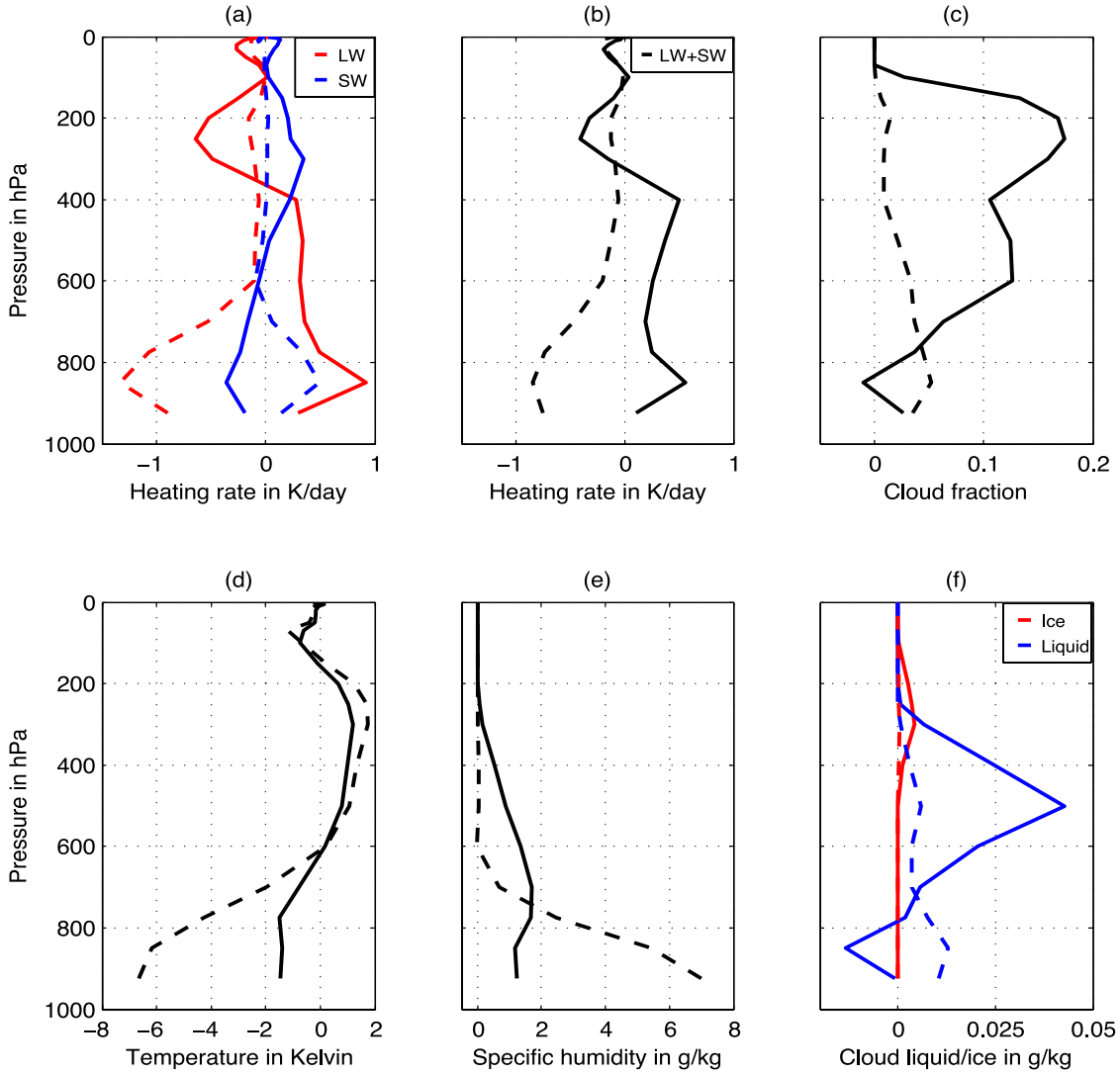

Fig. 2.8 Differences (AF-CTR) in heating rates in K/day (a, b), cloud fraction (c), temperature in K (d), specific humidity in g/kg (d), cloud ice in g/kg (e) and cloud liquid in g/kg (f) in May averaged over Region North (dashed line) and Region South (solid line). Region North represents in AF the region with descending air (10°E-10°W, 15°N-30°N) and Region South the region with ascending air (10°E-10°W, 4°N-15°N) for May. The regions are depicted in Figures 2.1 and 2.7e.

The slight increase in upper-tropospheric cloud cover (Fig. 2.8c) and in ice crystal concentration 0.4x10-3 g/kg at 300 hPa (Fig. 2.8f) leads to a weak negative heating rate (Fig. 2.8a), but this cooling has only minor effects on the temperatures (Fig. 2.8d). The increase in temperature between 600 hPa and 150 hPa (Fig. 2.8d) are more the result of latent heating or advection of warm air than the result of radiative processes. However

the net cooling between 600 hPa and 150 hPa is comparable small to the cooling below the 600 hPa pressure level (Fig. 2.8b).

Above Region South (Fig. 2.8, solid lines) the atmospheric column loses heat above 300hPa and gains heat below 300 hPa (Fig. 2.8b). The role of clouds in this region is more important than in Region North. Cloud cover increases in the middle and high troposphere (Fig. 2.8c), which influences the radiation budget directly (Liou, 2002). Low clouds act to cool the surface due to the reflection of SW radiation, whereas high clouds lead to warmer surface temperatures, because the reflection of SW radiation is less effective than the absorption of LW radiation and hence the greenhouse effect is enhanced. In our case the anomaly in high-level clouds from 400 hPa to the top of the troposphere (Fig. 2.8c) looks similar to the cooling anomaly in the heating rates at the same levels (Fig. 2.8b). At 400 hPa the absorption of the reemitted radiation from above, exceeds the enhancement of the radiative cooling and the LW heating rate remains positive down to the surface (Fig. 2.8a). The reduction in lower-troposphere air temperatures in experiment AF compared to CTR (Fig. 2.8d) are caused less by changes in the heating rates than by changes in the advection of cooler air from the Sahara. Similar to Region North, the temperature increase in the mid to high troposphere is caused by latent heating. Changes in specific humidity seem to play a minor role for heating rates in Region South and do not lead to a net cooling of the atmospheric column (Fig. 2.8e). Cloud ice content and cloud moisture content (Fig. 2.8f) show a maximum at 300 hPa of $4x10^{-3}$ g/kg and a maximum at 500 hPa of $42x10^{-3}$ g/kg, respectively.

In summary, the additional water vapor in the AF experiment acts as a radiative emitter in the lower atmosphere above Region North leading to large cooling rates in the lower troposphere. And the increase in high-level clouds above Region South causes a radiative heating in the lower atmosphere. These changes in the heating rates lead to the circulation anomalies described in section 2.4.2 (Fig. 2.6h, i). The circulation anomaly leads to a feedback on precipitation in Region North and South. In Region South the upward motion enhances convective processes and in Region North the downward motion diminishes convective processes. Furthermore the clockwise circulation anomalies could effect the meridional position of the ITF (Fig. 2.6h, i) and cause a weakening of the shallow meridional overturning cell in the Sahara and a strengthening of the Hadley cell (Fig. 2.6e, f).

The circulation feedbacks act during the whole WAM period (not shown) with the exception that the border between the region with ascending and descending air moves from 15°N in May to 19°N in August (Fig. 2.6e, f).

2.4.4 African Easterly Jet and Tropical Easterly Jet

Variations in the zonal jet systems, i.e. changes in the African Easterly Jet (AEJ) and in the Tropical Easterly Jet (TEJ) may directly affect the position and the strength of the West African Monsoon (WAM).

In comparison to observations the AEJ and the TEJ are well represented in the CTR experiment (Fig. 2.9, black line in Fig. 2.5). The zonal mean wind and the zonal mean temperature stratification of the atmosphere are shown in Figures 2.9a, b in May and August for the CTR experiment. In May the AEJ is represented with a distinct maximum located at 6°N and 700 hPa with easterly winds of about 11 m/s. The core of the AEJ moves northward and slightly upward until August to 16°N and 600 hPa with core velocities of about 12 m/s, which is comparable to reanalysis data (Wu et al., 2009). In May the TEJ is located at the equator in 200 hPa with easterly winds of about 6 m/s. This is much weaker and in opposite direction compared to the Subtropical Jet (SJ) which peaks around 30°N at 40m/s. In August the SJ and the TEJ both move further north. While the TEJ is strengthening and broadening with an absolute maximum of 21m/s at 12°N and 150 hPa, and a meridional spread with velocities above 15 m/s from 6°N to 18°N, the SJ is weakening. The TEJ and its maximum is located approximately 4° too far north compared to observations by Nicholson (2009), but shows a similar structure and strength.

The structure and the strength of both jet systems, the TEJ and the AEJ, change with the afforestation (Fig. 2.9 c, d; contour lines). The AEJ weakens (by more than 50% in May and by 25% in August) and shifts northward by about 4°, similar to the northward movement of the WAM precipitation maximum (Fig 2.5c). A weaker AEJ diverges less moisture to the west at lower levels before condensation can occur (Cook and Vizy, 2006) and the meridional extend of the WAM is confined by the position of the AEJ (Nicholson, 2009). Grist and Nicholson (2001) found in reanalysis data a similar relationship between AEJ and precipitation displacement. At the same time the TEJ strengthens during May nearly by 100% without meridional displacement. In August the TEJ core strengthens from 21 to 24 m/s, and further broadens in the AF experiment. A strong TEJ is connected to enhanced precipitation (Nicholson and Grist, 2001) and to strong upper-level divergence, which could promote low-level convection (Grist and Nicholson, 2001). The strengthening of the TEJ could also be caused by enhanced convective activity (Diongue et al., 2002).

The weakening of the AEJ could be explained by the weakening of the meridional temperature gradient between the Sahara and the Sahel zone and its relationship to the thermal wind (Fig. 2.9a, b; shaded). The AEJ is mainly driven by the positive meridional temperature gradient between the Sahara and the Sahel zone via geostrophy (Cook, 1999). The afforestation induced cooling over the Sahara by enhanced emission of LW radiation at lower atmospheric levels (see previous section) reduces the

meridional temperature gradient (Fig, 2.9 c, d; shaded). The reduction of the meridional temperature gradient in the near surface layers intensifies the northward pressure gradient force with height and leads to a weakening of the AEJ.

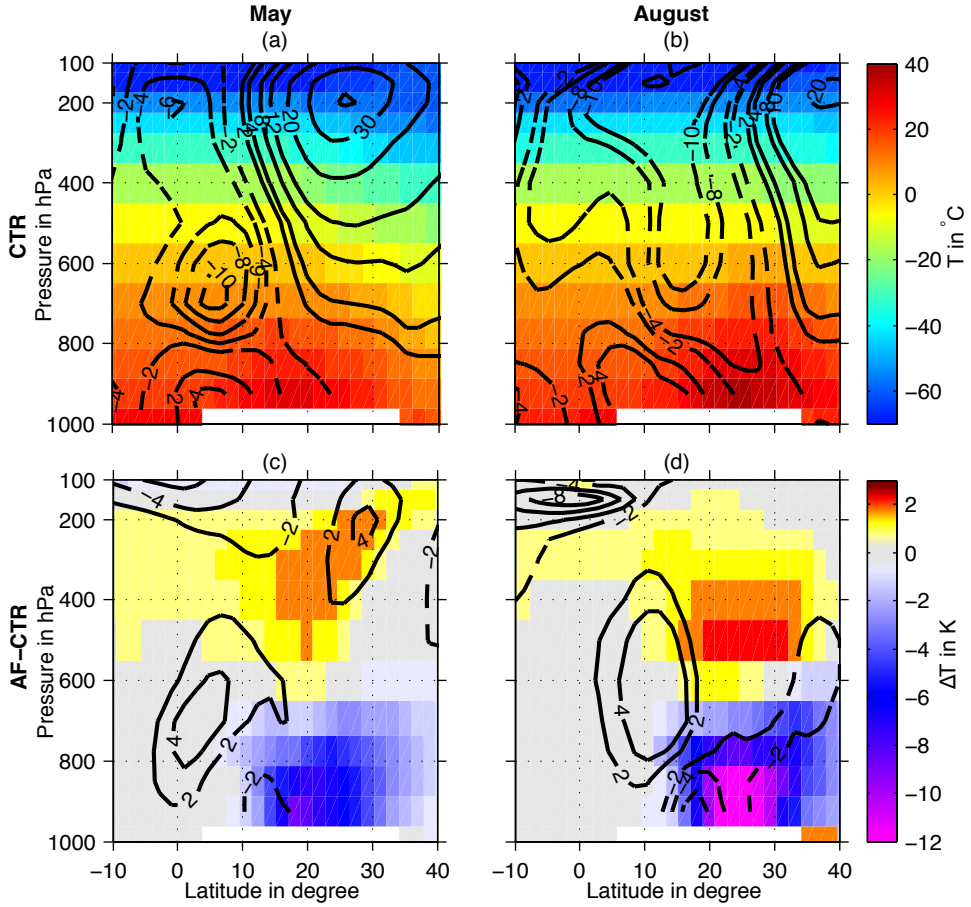

Fig. 2.9 Climatological 30-year averages of zonal velocities in m/s (contours) and of temperatures in K (shading) in May (a, c) and August (b, d) for the CTR experiment (a, b) and the differences between the AF and the CTR experiment (c, d) over the WAM area averaged from 10°W to 10°E.

Furthermore the warming signal in the subtropical upper troposphere over the Sahara could also explain parts of the anomalously strong TEJ. The warming in the upper troposphere changes the vertical temperature gradients, i.e. the lapse rate. The atmosphere above the Sahara switches from a dry to a moist environment from the CTR to the AF experiment, which leads to an adjustment of the vertical temperature profile.

The lapse rate in the CTR experiment in August averaged above the entire Sahara (not shown) between 750m and 5900m (500 hPa) amounts to -0.75 K/100m. This provides stable conditions for a dry air column. The atmospheric humidity of the Sahara increases in the AF simulation, so that the air column gets unstable and the moisture and temperature signal can be transported from the surface to higher altitudes. The lapse rate adjusts to -0.55 K/100m in the AF experiment, which results in stable conditions for the elevated moisture level in the atmosphere. In August the surface air temperatures in the AF experiment are 23.4°C, which is 9.1 K lower than in the CTR experiment, but the

difference in the lapse rate leads to an temperature increase with height from the surface to 500 hPa of 10.3 K, consistent with the warming signal at 500 hPa (Fig. 2.9d).

In summary the strengthening of the TEJ and the weakening of the AEJ during the extended WAM period in the AF experiment from May to August could enhance the WAM precipitation. In August the AEJ weakens by 25%, which is less in comparison to the 50% decrease in Patricola and Cook (2008) for a mid-Holocene scenario. The northward displacement by 4° of the AEJ from the CTR to the AF experiment is in accordance with the northward movement of the WAM precipitation maximum. Thermal wind induced differences in the zonal jet systems can be explained by the cooling between 600 hPa and the surface and the warming between 600 hPa and 100 hPa over the Sahara.

2.5 Discussion

In this study we concentrate on the main feedback mechanisms originating from an afforested Sahara and evaluate uncertainties. For atmospheric models it is still a challenge to simulate realistic WAM precipitation patterns, amplitudes and seasonality (Cook and Vizy, 2006) and there is still a large spread in its representation in current atmospheric models. The coupled ocean version of the low-top CAM4 is able to simulate a reliable West African Monsoon (WAM), Sahel rainfall and the typical rainfall patterns for present day conditions (Cook et al., 2012). CESM also shows similar results for future projections of Sahel precipitation as other CMIP5 models (Park et al., 2015).

Comparisons to palaeo-studies can assess the dynamics of climate models. Harrison et al. (2015) evaluated CMIP5 palaeo-studies and concluded that in general large-scale circulation changes are simulated satisfactorily, but improvements of key processes are needed to produce reliable regional projections. The vegetation feedback is one important mechanism to establish a Green Sahara state during the mid-Holocene (Patricola and Cook, 2008). Our model simulations reproduce a substantial weakening of the AEJ due to the enhanced latent heat fluxes and cooling of surface temperatures in the afforested areas, similar to previous mid-Holocene studies (Patricola and Cook, 2008; Rachmayani et al., 2015). However, our results differ considerably from those of Patricola and Cook (2008). Despite a similar weakening of the AEJ, most of the precipitation occurs south of the Saharan region and the circulation over the Sahara remains shallow without deep convection in our experiments. Particularities of the experimental design assuming an irrigated afforestation with large trees in contrast to natural vegetation cover with shrubs and grasses could have an influence on the development of precipitation in the Sahara. Irrigated afforestation leads to higher evapotranspiration fluxes and consequently results in lower surface temperatures in the Sahara. We suspect this could prevent the ITCZ to move further north, as the position of the ITCZ is also related to the meridional temperature maximum. The strong

evapotranspiration is related to the irrigation fluxes. Our irrigation fluxes are representative to other Sahara afforestation studies (Bowring et al., 2014; Ornstein, 2009). 90% of the evapotranspiration fluxes originate from transpiration fluxes, which yield from stomata opening and diffusion of carbon dioxide, essential for photosynthesis and ultimately CO_2 sequestration by afforestation. Because of present-day orbital forcing and less Eurasian vegetation cover compared to the mid-Holocene (Swann et al., 2014) conditions are less favorable for a northward migration of the ITCZ. However, a recent study that analyzed proxy data, indicated a general failure of PMIP3 models to simulate enhanced precipitation in the Sahara during the Holocene (Tierney et al., 2017). That study suggested that the vegetation and dust feedbacks are key processes for precipitation. Reduction in dust or increase in vegetation would promote precipitation in the Sahara to sustain a Green Sahara. Model simulations showed that dust reduction during the mid-Holocene could have led to a 500 km northward expansion of the WAM (Pausata et al., 2016). However, the representation of the dust cycle in North Africa in CESM is subject to considerable biases (Parajuli et al., 2016). A comprehensive evaluation of the North African dust-cycle would be needed, but is beyond the scope of this paper, before a reliable estimate of the impact of afforestation on dust emissions and precipitation in North Africa is possible.

Our results propose a northward expansion of the rainbelt during the WAM season into the Sahara as the main driving mechanism to increase precipitation in the Sahara upon afforestation. Ornstein et al. (2009) and Bowring et al. (2014) found a substantial enhancement of WAM precipitation in the southwestern Sahara. In our simulation only 26% of the irrigation is replaced by precipitation, and the WAM precipitation maximum is still south of the Sahara. We cannot determine exactly what causes the differences among the different model results, but we speculate that the different vertical resolutions among the model studies could play a crucial role for the results and for the adaptation of the WAM system to the afforestation. A higher vertical resolution in the atmospheric model component has been found to improve the simulation of Atlantic sea surface temperatures in the equatorial cold tongue, which affects the West Africa monsoon dynamics (Harlaß et al., 2015). The Planetsimulator (Bowring et al., 2014) uses only 10 vertical atmospheric layers and the GISS GCM ModelE (Ornstein et al., 2009) uses 20 vertical layers for the troposphere. In CESM-WACCM the troposphere is represented by 46 layers.

2.6 Summary

In this study we conducted two model simulations with CESM-WACCM under prescribed atmospheric CO_2 concentrations according to 1960, simulation AF with an afforested and irrigated Sahara and a reference simulation CTR with a desert Sahara. We showed that the irrigated afforestation of the Sahara leads to complex feedbacks between radiation budget, the atmospheric moisture cycle and the meridional

circulation, which limits the potential of irrigation-induced precipitation increases over the Sahara. Irrigation and afforestation of the Sahara enhances the simulated evapotranspiration by more than 1200 mm/yr, of which only 26% is re-precipitated locally over the Sahara. This is in contrast to other studies (Ornstein et al., 2009; Bowring et al., 2014), which found the increased precipitation large enough to replace a substantial amount of the required irrigation. In Ornstein et al. (2009) the WAM expands into the Sahara region and precipitation enhances for about one half of the Sahara by 1000 mm/yr. In our study the WAM maximum in precipitation is shifted northward from 10°N to 14°N, and therefore remains in the Sahel zone. Most of the moisture is transported southward by the atmospheric circulation, which would lead to higher desalination and pumping costs for the irrigation of the Sahara than in previous studies. Circulation feedbacks in CESM-WACCM are responsible for the WAM location in the northern Sahel zone. This is in contrast to the model study of Ornstein et al. (2009) who derived precipitation with patterns typical for the WAM in the Sahara starting in April and ending in November. Our results imply a positive atmospheric feedback, which establishes the WAM in the Sahel zone and inhibits precipitation above the Sahara.

Differences in precipitation response over the Sahara and of the WAM could be subject to the different model systems. For this reason we focus in our study on the processes that changes the WAM and further derive the relevance of these processes to feedback on precipitation over the Sahara (Fig. 2.10). An overview of the relevant processes is given in the following:

- Maximum surface temperatures determine the position of the ITF, the preferred position for initiating convection in the AF simulation and determining the position of the ITCZ (Fig. 2.10, green).
- WAM precipitation intensity and extend as well the meridional position depends partially on the intensity and location of the AEJ and the TEJ (Fig. 2.10, blue).
- Irrigation provides additional atmospheric humidity, which enhances precipitation over the Sahara. Humidity advection also enhances precipitation over the Sahel zone (Fig. 2.10, magenta).
- Meridional circulation anomalies could be amplified by feedback mechanisms, which affect precipitation in the Sahara and the Sahel zone, e.g. downward vertical air motion in the Sahara would inhibit convective processes (Fig. 2.10, red).

In the following we explain these processes more in detail with the help of schematic Figure 2.10. First we show why Saharan surface temperature is cooling and than we connect this with the position of the ITF.

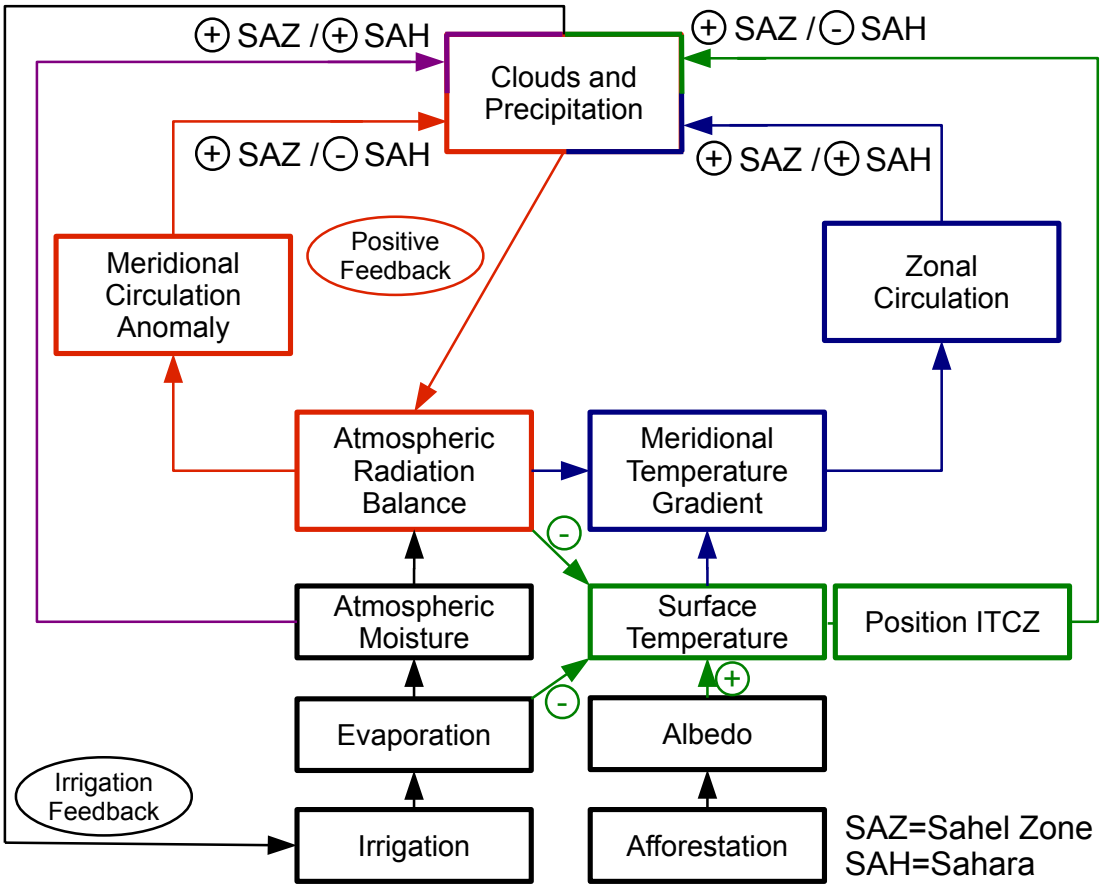

Fig. 2.10 Schematic overview over processes changing precipitation over the Sahel Zone (SAZ) and the Sahara (SAH), which are influenced by the irrigation and afforestation of the Sahara in CESM-WACCM. The enhanced level of atmospheric moisture increases the general potential for precipitation in both regions (purple). Distribution of precipitation between SAZ and SAH determines how effective irrigation is. More precipitation over the Sahara reduces the irrigation rate in the Sahara (Irrigation feedback). The positive feedback (red) maintains the meridional circulation anomaly over the Sahara and the Sahel zone and promotes precipitation over the SAZ and less precipitation over the SAH. Changes in the zonal jet system (blue) promote precipitation over the SAZ and the SAH. The cooling in the Sahara shifts the ITF south of the Sahara and promotes more precipitation over the SAZ and less over the SAH (green). For more details see text.

The afforestation itself increases the local surface albedo and respectively the absorption of SW radiation by 19 Wm^{-2} (Fig. 2.3). The albedo difference between trees and bare soil plays only a minor role for the radiation balance, because low-level clouds in the AF experiment significantly reduce the incoming SW radiation. The main driver for the surface cooling is the increase in evapotranspiration by 94 Wm^{-2} (Fig. 2.3), which is dominated by plant transpiration. The transpiration rate depends on different factors, such as gross primary production, atmospheric carbon dioxide concentration and the individual plant type. The Lower surface temperatures in the AF experiment reduce the sensible heat flux to the atmosphere. The net effect of the adapted radiation

budget is a temperature reduction of 6.3 K in the Sahara in the AF experiment, whereas the effect on global surface temperature is with 0.04 K negligibly small. We note, that the atmospheric CO_2 concentration in CESM-WACCM is held constant at 1960 conditions and therefore any GHG-induced warming due to CO_2 increase or afforestation induced cooling due to CO_2 reduction is not simulated in the model runs.

However, the temperature reduction in the Sahara (Fig. 2.10, green) shifts the temperature maximum from the Sahara into the Sahel zone, which could explain the southward displacement of the ITF. Under dry Sahara condition (in the CTR experiment), the position of the ITF plays a minor role for the position of the rainbelt, similar to observations (Nicholson 2009). This relationship could change under moist Sahara conditions in the afforested, irrigated Sahara (AF) experiment. The strong cooling in the Sahara acts like a border for the meridional displacement of the ITF.

The adaptation of the zonal circulation (Fig. 2.10, blue) to an irrigated afforestation favors more precipitation over the Sahel zone and a slight northward movement of the WAM. The increased humidity and the changes in the vertical and meridional temperature profile over the Sahara and the Sahel zone change zonal circulation features such as the AEJ and the TEJ. The irrigation-induced evapotranspiration increases the humidity content of the Saharan lower atmosphere, which in turn enhances the LW emissivity and cools the lower atmospheric levels. This cooling decreases the vertical and meridional temperature gradient and alters therefore the geostrophic components of the zonal circulation. The reduction of the meridional temperature gradient in the Sahara leads to an geostrophic adjustment of the AEJ with a weakening of up to 50% and a northward shift by approximately 4°. The northward shift of the AEJ appears simultaneously with a northward shift of the WAM maximum. This relationship between the meridional position of the AEJ and the WAM maximum precipitation has also been found in observations (Nicholson, 2009). The TEJ enhances from May to August together with intensified precipitation and upper level divergence. The weakening and northward shift of the AEJ and the enhancement of the TEJ could increase the precipitation during the WAM and could also be relevant for the early onset of the WAM in May in the AF experiment in comparison to the CTR.

The general southward export of humidity from the Sahara and the gain of humidity over the Sahara increase precipitation in and south of the Sahara (Fig. 2.2), which has in general a positive effect on precipitation in the Sahel zone and in the Sahara (Fig. 2.10, magenta). But the irrigated afforestation leads also to changes in the meridional circulation.

The meridional circulation (Fig. 2.10, red) adapts with subsidence over the Sahara and ascent over the Sahel zone, enhancing the Hadley circulation (Fig. 2.6). This could diminish convective processes in the Sahara and could enhance convective processes in the Sahel zone. The increased humidity over the Sahara (Fig. 2.8e) and the enhanced

high-level cloud coverage over the Sahel zone (Fig. 2.8c) drive a meridional gradient in the heating rates (Fig. 2.7h, i) and with this a meridional circulation anomaly (Fig. 2.6h, i) between both regions.

The meridional circulation anomaly leads to advection of additional humidity from the Sahara to the Sahel zone (Fig. 2.2). The additional humidity would enhance convective processes in the Sahel zone and lead to more high-level cloud development in the Sahel zone. This increases the meridional gradient in the heating rate and would also suppress convective processes over the Sahara. This positive circulation feedback maintains the circulation anomaly.

Furthermore less precipitation in the Sahara leads to an irrigation feedback (see Fig. 2.10). More irrigation is required in the Sahara, which also leads to an increase in evaporation and would drive the previously described positive feedback.

Finally, the intervention in the climate system in North Africa due to the irrigated afforestation of the Sahara leads to a number of processes, which could interact with each other. In this study with CESM-WACCM, we derive a qualitative analysis of the individual processes and we are only able to make quantitative estimates for all processes. Nevertheless, this study indicates that several factors exist, which reduce the precipitation potential over the Sahara and make the Sahara less favorable for large-scale afforestation efforts. It would also be conceivable, that additional climate states exists under which the WAM is able to migrate into the Sahara, as it was found in Ornstein et al. (2009).

However, we note here that such large-scale irrigation can disturb the global atmospheric water budget and could lead to global teleconnections. Climate change could also affect the response of the climate system. Under increasing greenhouse gas concentrations the transpiration would be reduced, because the partial carbon dioxide pressure is reduced and the stomata have to be opened less (Allaway and Mansfield, 1967). Reduced transpiration rates would affect the loss of irrigated water to the atmosphere and the evapotranspiration induced surface cooling. Possible global teleconnections and the effect of climate change are subject of a follow-on study.

Acknowledgements:

This work is a contribution to the DFG-funded Priority Program SPP 1689 and was partly performed within the Helmholtz-University Young Investigators Group NATHAN, funded by the Helmholtz-Association and GEOMAR, the Helmholtz Centre for Ocean Research Kiel. The CESM-WACCM simulations have been performed at the Deutsche Klimarechenzentrum (DKRZ) in Hamburg, Germany. We thank two anonymous reviewers for their helpful comments.

2.7 Appendix A

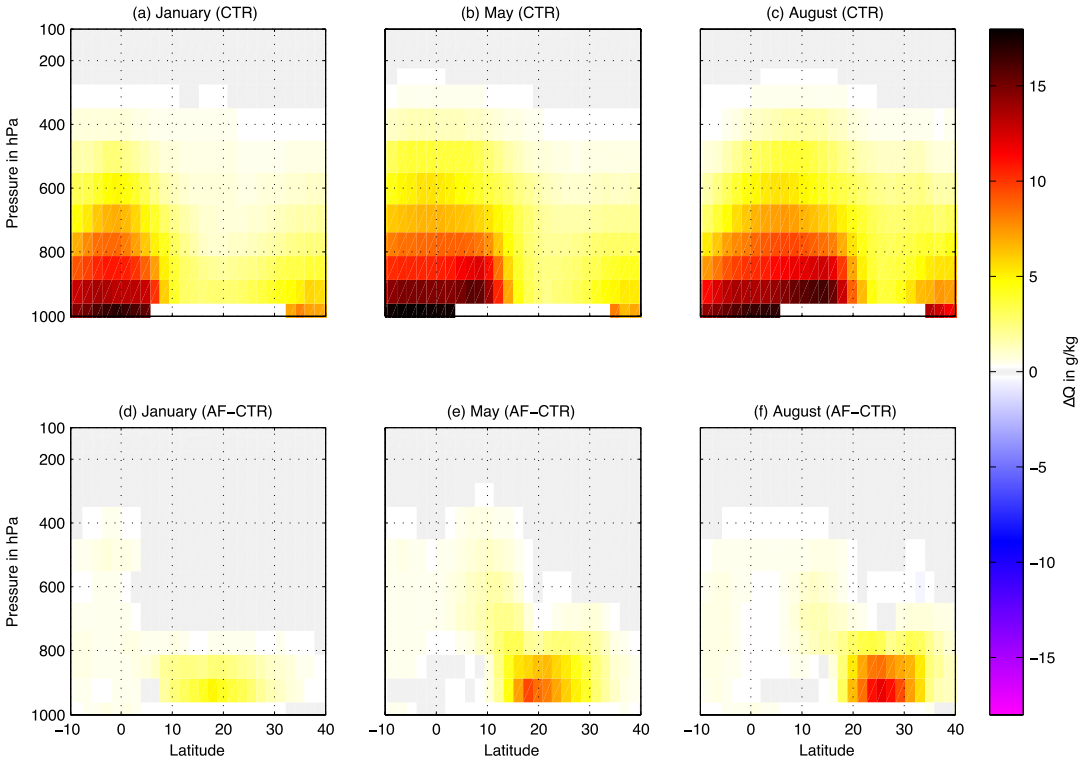

Fig. A1 Climatological differences in specific humidity in g/kg averaged over the WAM area from 10°W to 10°E in January (a,c), May (b, e), and August (c, f) for the CTR experiment (a-c) and the difference between the AF and the CTR experiment (d-f).

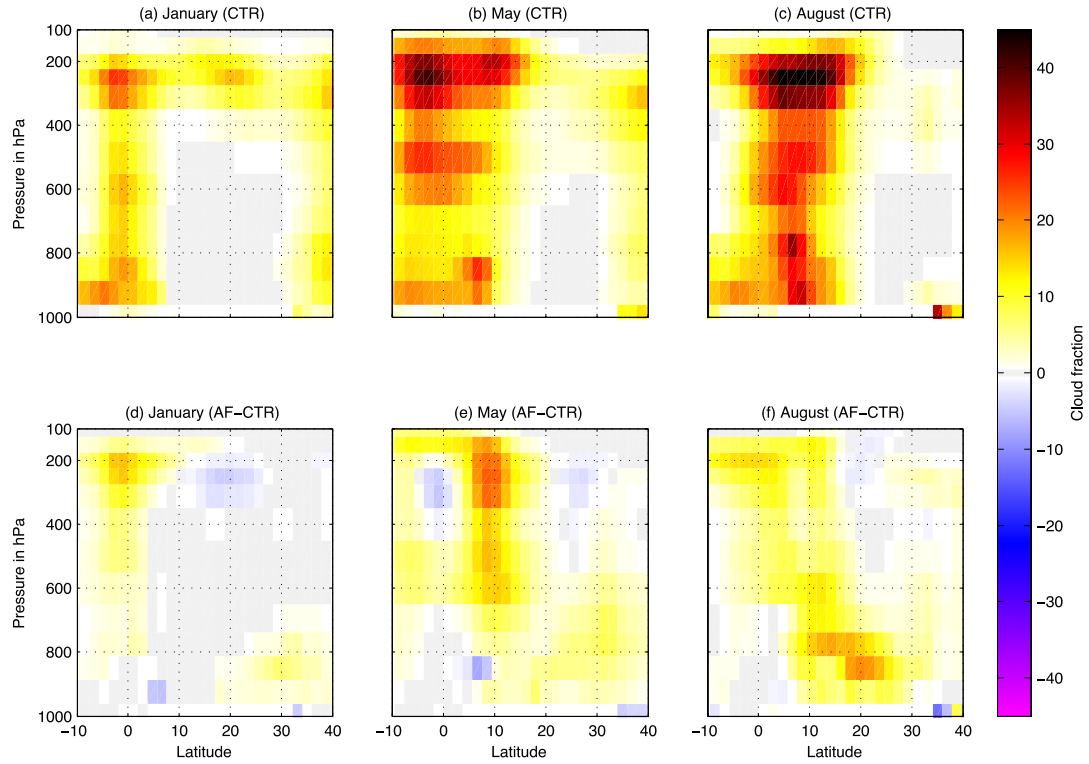

Fig. A2 Climatological cloud fraction in % averaged in the WAM area from 10°W to 10°E in January (a,c), May (b, e), and August (c, f) for the CTR experiment (a-c) and the difference between the AF and the CTR experiment (d-f).

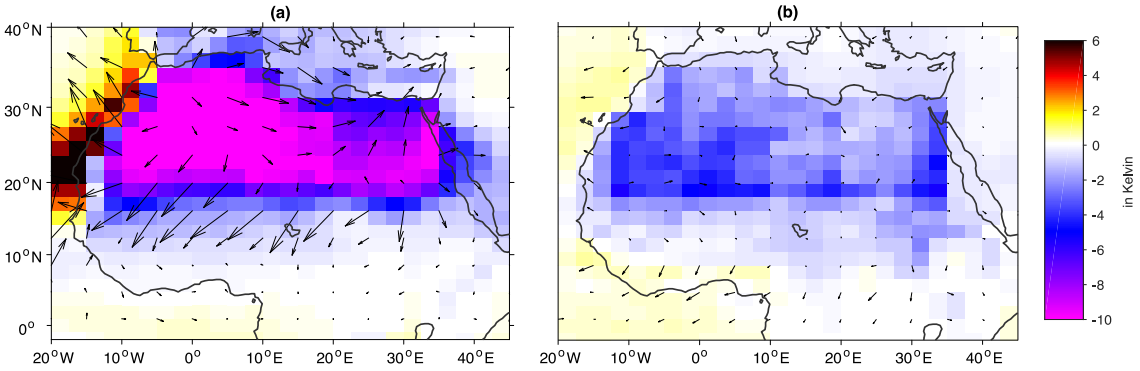

Fig. A3 Seasonal summer (a) and winter (b) long-term (30-year) mean differences between the AF and the CTR experiments in surface air temperatures in Kelvin [K] (shaded) and surface wind anomalies (arrows).

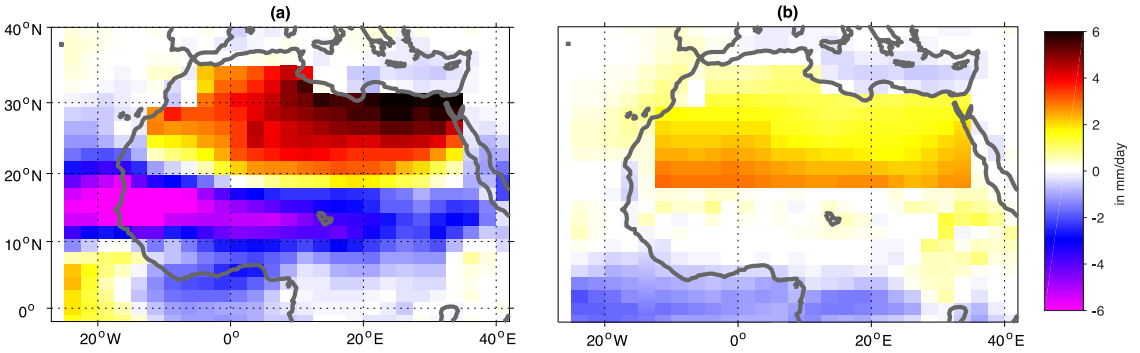

Fig. A4 Seasonal summer (a) and winter (b) long-term (30-year) mean differences between the AF and the CTR experiments in the atmospheric vertically integrated moisture flux convergence in mm/day. The moisture flux is derived from evapotranspiration minus precipitation and convergences have to be balanced by horizontal moisture advection.

3. Consequences of an Irrigated, Afforested Sahara on the Development of Tropical Cyclones and Hurricanes in the Atlantic under recent and future climate

Tronje P. Kemena[1] • Thomas Martin[1] • Katja Matthes[1,2] • Andreas Oschlies[1,2]

Abstract

Afforestation of the Sahara might be potentially effective to mitigate climate change but requires substantial amounts of irrigation to sustain the planted trees. Enhanced evapotranspiration would moisten the Saharan air, but its impact on the global atmospheric hydrological cycle is widely unexplored. Here, we report new model results for present-day and worst-case climate change experiments that highlight the consequences of an afforested Sahara for tropical cyclone (TC) development over the Atlantic. We identify advection of humid air from the Sahara to the Atlantic as the main driver for the intensification of TCs. Humidity induced changes in mid-tropospheric relative humidity, sea surface temperatures, vertical wind shear and maximum potential intensity provide substantial contributions to the intensified TC and hurricane development and therefore to a larger number of hurricanes. The Saharan afforestation has considerably larger impacts on TC development than a worst-case global warming scenario.

Keywords:
Hurricanes; Tropical Cyclones; Afforestation; Climate Engineering; Irrigation

Tronje Kemena
e-mail: tkemena@geomar.de
[1] GEOMAR Helmholtz Centre for Ocean Research Kiel, Germany
[2] Christian-Albrechts Universität zu Kiel, Germany

3.1 Introduction

In September 2017, the number of hurricanes and major hurricanes was well above the average and the activity of tropical storms was 3.5 times higher than the long-term average for September[3]. The destruction and the casualties of hurricane Irma and Maria (September, 2017) raise again questions about climate change and its impact on hurricane development. Hurricane Irma counts to one of the most intense hurricanes observed in the Atlantic with wind speeds up to 295 km/h (82 m/s). In the Atlantic, tropical cyclones (TCs) with wind speeds of 120 km/h (33 m/s) or higher are categorized as hurricanes and TCs with wind speeds of 180 km/h (50 m/s) or higher are classified as major hurricanes. An intensification of TCs in wind speed would result in more and stronger hurricanes with significant additional costs for society and economy (Narita et al., 2009). However, questions arise regarding how climate engineering may also affect physical phenomena and in particular TCs.

Irrigation and afforestation of the Sahara has been recently considered as a climate engineering method to sequester substantial amounts of CO_2 from the atmosphere (Ornstein et al., 2009; Keller et al., 2014; Bowring et al., 2014; Cheng et al., 2017). The irrigated, afforested Sahara leads to an intensification of rainfall in the Sahel zone (Kemena et al., 2017), which has been shown to be related to a more intense Atlantic hurricane development (Landsea and Gray, 1992; Latif and Keenlyside, 2011; Wang and Gillies, 2011). Furthermore, the irrigated, afforested Sahara would substantially change air mass characteristics over the Saharan thermal low and nearby the African easterly jet in the Sahel zone (Kemena et al., 2017). It has been shown previously that more than 80% of all major hurricanes in the Atlantic are formed from African easterly waves (Landsea, 1993), which originate from the Saharan thermal low and the West African Monsoon zone (Chen et al., 2008). Exactly these regions are affected by the irrigated afforestation (Kemena et al., 2017) and could therefore affect TC development during their genesis phase.

Our hypothesis is that intensification of TCs could not only be driven by climate change, but also occur unintentionally as a side effect from climate engineering. As a case study, we analyze model results from an irrigated afforestation of the Sahara scenario and compare it to a business-as-usual scenario. We investigate parameters like sea surface temperatures (SSTs), vertical wind shear, environmental humidity level in the Main Development Region in the Atlantic (MDR; defined below) with business-as-usual climate change and Sahara afforestation scenarios to determine their impact on TC development. This has to our knowledge not been investigated by any other study.

[3] National Hurricane Center (http://www.nhc.noaa.gov), Atlantic Tropical Weather Summary for September 2017

The mentioned parameters are steering the development and intensity potential of TCs over the Atlantic (Gualdi et al., 2008; Camargo, 2013) as explained in the following.

A warm sea surface, high humidity and low wind shear are suitable for formation and development of TCs in the Atlantic. Most TC tracks can be found in the MDR, which extends from the west coast of Africa to the Caribbean Sea in the North Atlantic. The MDR ranges meridionally from 10°N to 25°N, because close to the equator the Coriolis force is too weak to sustain a TC and north of 25°N most TCs recurve to the open ocean without landfall on the American continent (Colbert and Soden, 2012). TCs receive their energy from the ocean surface, so warmer SSTs are connected to an increase in TC activity (Saunders and Harris, 1997; Steenhof and Gough, 2007; Saunders and Lea, 2008). The minimum SST have to be above 27°C to sustain a TC (Gray 1968; Webster et al. 2005; Steenhof and Gough 2007). Vertical wind shear could inhibit the genesis of TCs and could also weaken or limit the intensification of TCs during its lifecycle (DeMaria, 1996; Wang and Holland, 1996; Frank and Ritchie, 2001; Wang et al., 2004; Wong and Chan, 2004; Paterson et al., 2005; Zheng et al., 2007). Earlier model simulations suggest an environmental wind shear strength of more than 10 m/s to start the dissipation of TCs (Wong and Chan, 2004; Paterson et al., 2005). Vertical wind shear between the 850 and 200 hPa levels explain 44% variability of TC activity in the central MDR (Aiyyer and Thorncroft, 2006). Environmental humidity levels in the mid-troposphere could influence storm size (Hill and Lackmann, 2009), intensification (Braun et al., 2012; Wu et al., 2012; Wu et al., 2015) and landfall (Kimball, 2006) of TCs. For example the Saharan Air Layer supplies the MDR with dry air at mid tropospheric levels, which slows down the intensification of TCs (Dunion and Velden, 2004). A measure of the theoretical maximum intensity of a mature TC is given by the maximum potential intensity (VMAX) (Bister and Emanuel, 2002), which was used and validated in several studies (Yu et al., 2010; Camargo et al., 2013; Ting et al., 2015; Yan et al., 2015; Polvani et al., 2016). VMAX gives a theoretical measure of maximum potential wind velocities in the TC.

Our findings will contribute to the scientific discussion, whether or not irrigated afforestation of the Sahara should be considered as a climate engineering option for atmospheric CO_2 removal. A comparison of the afforested Sahara scenario to results from a worst-case climate change scenario will indicate, which of these two scenarios has more negative consequences for tropical cyclone and hurricane development.

This study is structured as follows; In Section 3.2 the model setup and calculation of TC development indices related to SST, relative humidity, wind shear and VMAX are presented. In Section 3.3 results for the afforestation and for a worst-case climate change scenario are presented for SST and VMAX (Section 3.3.1), relative humidity (Section 3.3.2) and wind shear (Section 3.3.3) during the hurricane season (ASO) and their seasonal cycle (Section 3.3.4). This is followed by conclusions and discussions in Section 3.4.

3.2 Model Setup and TC Development Indices

We conduct a model study with the Community Earth System Model with high-top atmosphere, CESM-WACCM, (Marsh et al. 2013) employing different land use schemes for the Sahara region as described in Kemena et al. (2017).

In our Control (CTR) and afforested Sahara (SAH) experiments, we simulate 50 years with atmospheric CO_2 concentration set to constant 1960 conditions. The latter 30 years are taken for analysis. In the SAH experiment irrigation is needed to establish a forest in the Sahara, which results in a net flux of water from the irrigated Sahara to the atmosphere of 919 mm/yr (Kemena et al., 2017). This is mainly driven by enhanced transpiration fluxes. More details about the experimental design of the SAH experiment can be found in Kemena et al. (2017). The climate change experiment follows the World Climate Research Programme's Coupled Model Inter-comparison Project Phase 5, with the twenty-first century Representative Concentration Pathways-Scenario 8.5 (Taylor et al., 2012). Here, we perform two experiments, one without afforestation (RCP8.5) and one with afforestation (RCP8.5SAH), each 100 years long covering the period from year 2000 to 2100. The differences between the two periods 2080 to 2099 and 2000 to 2019 are used for the analysis of the impact of climate change and afforestation.

For presenting our results we concentrate on TC development in the so-called main development region (MDR; 80°W-20°W, 10°N-25°N, as used in Doi et al. (2013)). A schematic overview of the involved processes and pathways is given in Figure 3.1. The location of the MDR is shown in Figure 3.2 (black box).

In this study we analyze the following indices and evaluate their effect on TC development in the MDR for the peak hurricane season from August to October similar to other studies (Gualdi et al., 2008; Camargo, 2013; Ting et al., 2015):

- Sea surface temperatures (SSTs)
- Maximum of the cyclone potential intensity (VMAX)
- Mid tropospheric relative humidity (RH_{700})
- Vertical wind shear ($U_{|850\text{-}200|}$)

The maximum of the cyclone potential intensity (VMAX) is calculated as defined in Bister and Emanuel (2002):

$$VMAX^2 = \frac{C_K}{C_D}\frac{SST}{T_0}(CAPE^* - CAPE) \tag{3.1}$$

with C_K and C_D the heat exchange and drag coefficients, sea surface temperature (SST), outflow temperature (T_0), convective available potential energy (CAPE) and convective available potential energy for a saturated air parcel (CAPE*). The calculation of CAPE, CAPE* and T_0 takes vertical profiles of pressure, temperature, and mixing ratio into account. CESM-WACCM is able to reproduce spatial patterns of VMAX comparable to patterns calculated from observational data and from a multi-model mean of 25 CMIP5 models (Polvani et al., 2016). Mid tropospheric relative humidity is calculated at the 700 hPa level (RH_{700}). Local environmental relative humidity is a good indicator for TC development in the Atlantic (Hill and Lackmann, 2009; Wu et al., 2012). The vertical wind shear index is represented by the absolute zonal wind speed difference between the 850 hPa and 200 hPa levels ($U_{|850-200|}$). Since meridional wind shear has no significant contribution to absolute wind shear and climate warming-induced wind shear in the MDR in the Atlantic (Vecchi and Soden, 2007), we do not consider it. As wind shear is a nonlinear function, it is crucial in which order spatial, temporal averages and wind shear differences are calculated. In the following we call it regional (local) wind shear, when zonal velocities are spatially averaged before (after) absolute wind shear difference is calculated.

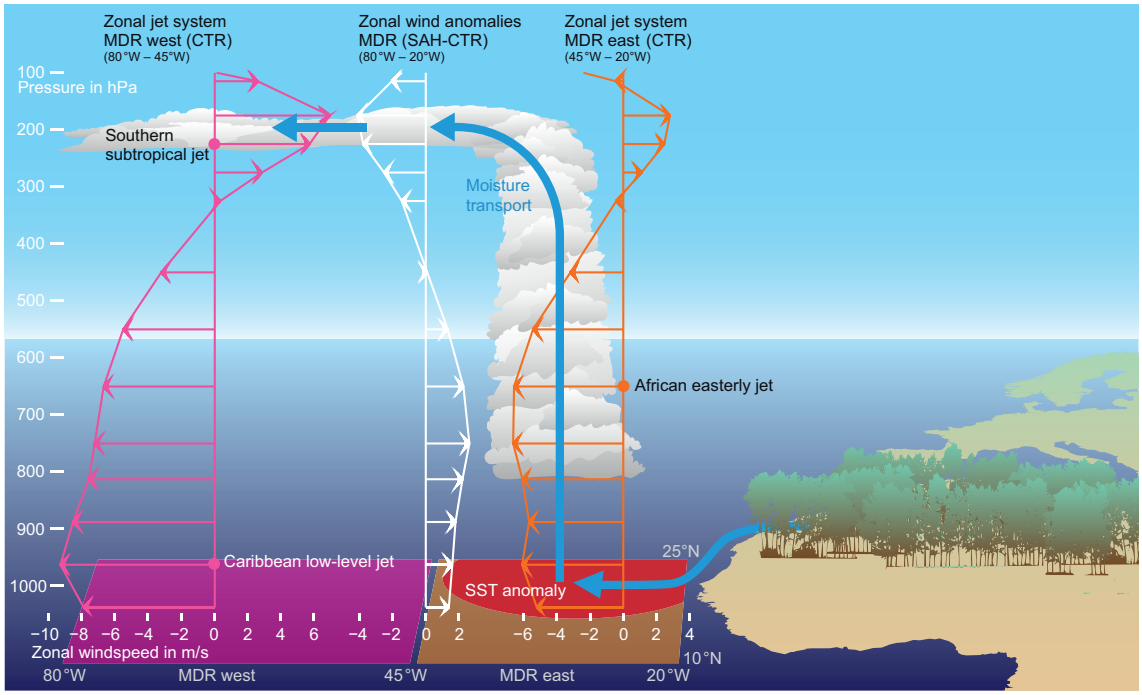

Fig. 3.1 Schematic overview of changes in the Main Development Region (MDR) during August to October driven by an afforested, irrigated Sahara. The vertical wind profile of the SAH experiment is given for MDR west (80°W-45°W, purple arrows) and MDR east (5°W-20°W, orange arrows). The profile of wind anomalies between the SAH and the CTR experiments are given for the whole MDR (white arrows). Humidity is advected from the Sahara into the MDR and initiate deep convection (blue arrows). This enhances the greenhouse effect, reduces the latent heat flux and leads to more high-level clouds in the MDR east. Warmest SST anomalies can be found in the northeast MDR (red ellipse). See text for more details.

The impact of changes in dust load over the MDR on the TC development is not analyzed. Increasing vegetation cover in the Sahara would reduce the Saharan dust

export to the Atlantic, but CESM is still subject to considerable biases in dust fluxes (Parajuli et al. 2016) and therefore aerosol as well as dust are prescribed as climatology.

3.3 Effects on Tropical Cyclone (TC) Development

An afforested, irrigated Sahara is a tremendous source of additional water reaching transpiration fluxes of 1112 mm/yr averaged over the Sahara region (Kemena et al., 2017). The mean zonal atmospheric circulation transports the water from the Sahara into the MDR. This affects environmental parameters steering the development of TCs during the hurricane season with the following three main effects: (i) Warmer SSTs (see Fig. 3.1, SST anomaly) increase the maximum cyclone potential intensity VMAX (Section 3.3.1). (ii) The advected humidity (Fig. 3.1, blue arrows) raises the relative humidity at 700 hPa (RH_{700}) (Section 3.3.2), where the gain of water vapor enhances the greenhouse effect and reduces ocean to atmosphere latent heat fluxes. (iii) The geostrophic adjustment of zonal wind velocities (see Fig. 3.1, white arrows) to the adapted vertical profile in temperature affects the vertical wind shear between 850 hPa and 200 hPa ($U_{|850\text{-}200|}$). The wind shear diminishes in the western part of the MDR and enhances in the southeastern part (Section 3.3.3).

The MDR region is split into a western and eastern box (separated at 45° W, see Fig. 3.1 purple and brown boxes), because the zonal jet systems (Fig. 3.1, purple and brown arrows) differ between these boxes, which affect the wind shear analysis.

3.3.1 SSTs and VMAX

In the SAH experiment, the artificial forest enhances transpiration rates and increases local atmospheric humidity in the Sahara. Easterlies advect this anomalous water content into the eastern MDR (Fig. 3.1, blue arrows, Fig. S3.1, S3.2). The additional water content over the MDR perturbs the atmospheric radiation balance (described later), which leads to higher SSTs in the MDR with maximum anomalies of approximately 4 K in the northeast edge of the MDR (Fig. 3.2a).

These higher SSTs leads to a significant increase in maximum potential intensity (VMAX) of TCs over the Atlantic (Fig. 3.2b). The maximum in VMAX anomalies with approximately 50 m/s can be found in the northeast edge of the MDR. The Anomaly in SSTs is the main driver for the VMAX anomalies (Fig. S3.3). The adaptation of the atmospheric temperature profile lead to a small spatially uniform reduction in VMAX (Fig. S3.3c) as the temperature profile affects convective available potential energy, which is taken into account in VMAX.

In contrast to the strong changes in the SAH experiment the RCP8.5 experiment shows comparable weak changes of VMAX in the MDR (Fig. 3.3b). The spatially uniform SST anomalies (Fig. 3.3a) over the MDR increase VMAX (Fig. S3.4a), but the

adaptation of the vertical atmospheric temperature profile compensates the SST effect (Fig. S3.4c).

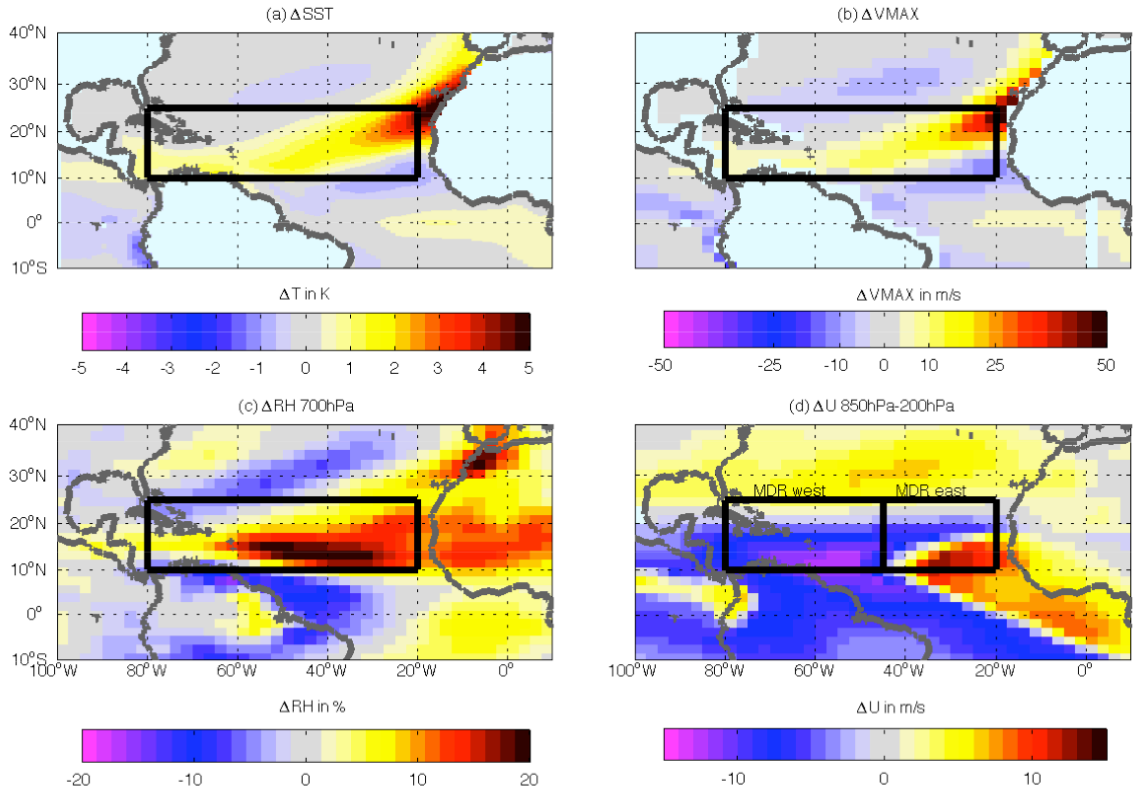

Fig. 3.2 Differences between the SAH and the CTR simulations for sea surface temperatures (SSTs) in K (a), maximum potential intensity (VMAX) in m/s (b), relative humidity at 700 hPa (RH700hPa) in % (c), local (description in section 2) vertical wind shear (U850-200hPa) in m/s calculated as absolute difference of zonal velocities from the 850 and 200 hPa levels (d) averaged over August, September and October. The black boxes denote the MDR west and east (d) and the MDR (a, b, c).

In the SAH experiment, the main drivers for the SSTs changes are the local greenhouse effect, ocean to atmosphere latent heat flux and cloudiness, explained in the following. The high water vapor content increases the greenhouse effect by more than 9 W/m^2 and reduces the latent heat flux from ocean to atmosphere by nearly 11 W/m^2 averaged over the MDR (not shown). The surplus of humidity also changes the cloud coverage, which reduces incoming shortwave radiation and leads to a net surface cooling of about 8 W/m^2 in the MDR (not shown), which almost compensate the additional greenhouse effect. In the eastern (western) MDR more (less) mid- and high-level clouds and less (more) low-level clouds appear (Fig. S3.5). Due to the increase in cloudiness, the warming in the MDR is partially compensated or reversed. However, in the northeast corner of the MDR low-level clouds are transformed into high-level clouds, which lead to a surface warming due to the higher transmissivity of high-level clouds (not shown). The advected water affects not only SSTs, but also directly the TC development in the MDR as shown next.

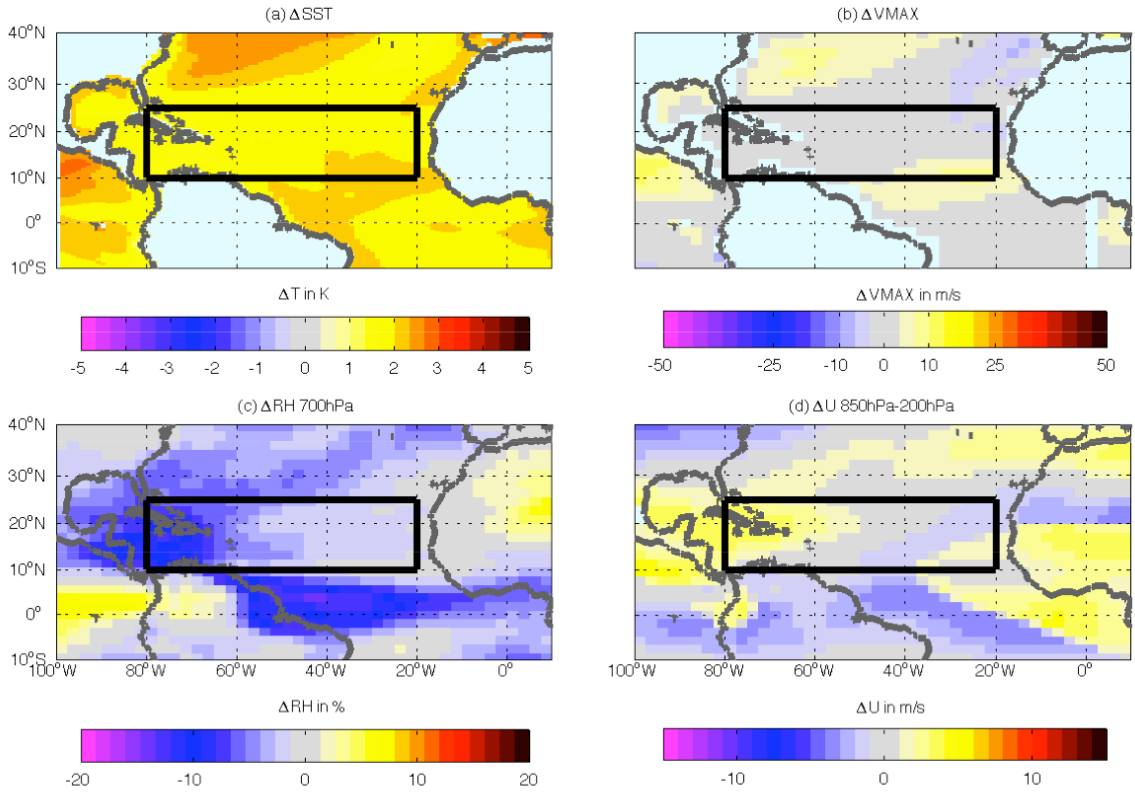

Fig. 3.3 Differences between the periods 2099-2080 and 2019-2000 of the RCP8.5 simulation in maximum potential intensity in m/s (a), sea surface temperatures in K (b), relative humidity at 700 hPa in % (c), vertical wind shear in m/s calculated as absolute difference of zonal velocities from the 850 and 200 hPa level (d) averaged for the month August, September and October. The black box denotes the MDR.

3.3.2 Advection of Humidity and RH_{700}

An important measure for intensification rates of TCs in the Atlantic is the environmental relative humidity level (Wu et al., 2012). In the CTR simulation, the air, which is advected from North Africa to the MDR, is dry and low in relative humidity. Water advection from the afforested Sahara increase humidity level over the MDR with the strongest humidity gain at the 850hPa level (Fig. S3.1). The humidity anomaly is distributed between the 700hPa level and the surface layer in the eastern part of the MDR close to the African coast and it weakens towards the west (Fig. S3.2). This increase in water content also affects the relative humidity levels. RH_{700} raises from 44% to 51% averaged over the MDR with a local maximum difference in the relative humidity of about 20% (Fig. 3.2c) in the southern part of the MDR around 40°W. This is in contrast to the results of the global warming experiment RCP8.5 (Fig. 3.3c), in which the RH_{700} weakens from 44% to 40% in the MDR without distinct spatial patterns.

3.3.3 Wind Shear $U_{|850-200|}$

Vertical wind shear is defined as the absolute difference in zonal wind velocity between the 850 and 200 hPa level. The vertical profile of the zonal wind component is shown for the CTR simulation in each MDR box separately (Fig. 3.1, Fig. S3.6a, b). In the MDR west box (Fig. 3.1 purple profile, Fig. S3.6a) the southern subtropical westerly jet and the Caribbean low-level jet with easterly velocities cause a total wind shear of 14 m/s. In contrast to this in the MDR east box easterlies dominate the vertical wind profile with the African easterly jet at 650 hPa (Fig. 3.1, orange profile, Fig. S3.6b), which leads to a total wind shear of 7 m/s.

Afforestation leads to an adjustment of the geostrophic wind in the atmosphere, which affects wind shear. A vertical flux of sensible heat and latent heat changes the atmospheric temperature profile (Fig. S3.6c, d; shaded). The geostrophic adjustment of zonal wind velocities (Fig. S3.6c, d; contour lines) results in a reduction of $U_{|850-200|}$ (regional wind shear, Fig. 3.1) from 14 (8) m/s to 8 (1) m/s in the west (east) box. To calculate regional wind shear first zonal velocities are spatially averaged before absolute wind shear differences are calculated. For the local wind shear the calculation order is reversed.

The spatial response in $U_{|850-200|}$ (local wind shear, Fig. 3.2d) is more inhomogeneous because of the less pronounced extend of the subtropical jet into the eastern MDR box. In the south east of the MDR, vertical wind shear is in general low and the imposed wind changes lead to an increase in local wind shear, in contrast to the rest of the MDR (Fig. 3.2d). The vertical wind shear increases (decreases) in the southern part of the MDR east (west) box south of 20°N with a local maximum anomaly of +(-)12 m/s. This leads in total to a box wide average local wind shear decrease in the MDR west box by 5 m/s and to an increase in the MDR east box by 1 m/s.

In the RCP8.5 experiment we find a to the RCP8.5 simulation comparable weak response in vertical wind shear over the MDR (Fig. 3.3d). Local maxima are in the order of 2 m/s, a magnitude smaller than the impact of the afforestation.

3.3.4 Seasonal Cycle of TC Indices

In Figure 3.4 the seasonal cycle of the TC indices is presented for simulations with afforestation (Fig. 3.4, green) and without afforestation (Fig. 3.4, red). In the SAH (RCP8.5SAH) experiment VMAX increases by at least 5 m/s during July to October (November), which is attributed to higher SSTs (Fig. 3.2a, b). SST anomalies due to afforestation are strongest during autumn and weakest during spring. In contrast to this, the RCP8.5 (Fig. 3.4, red lines) experiment shows no remarkable difference in the seasonal cycle of VMAX compared to the CTR. Global warming leads to the strongest impact on SSTs in the MDR (Fig. 3.4b) with direct impact on VMAX, but the adaption of the vertical temperature profile leads to a compensation of the SST effect on VMAX (similar to the months ASO in Fig. S3.4c).

The additional advection of water in the SAH (RCP8.5SAH) experiment, compared to the advection of dry air in CTR (RCP8.5) from the Sahara to the Atlantic, leads to an increase in relative humidity over the MDR with the highest increase at the 850 hPa level by 12% (13%). At 700 hPa the water advection due to afforestation leads to substantial higher relative humidity from July to September (Fig. 3.4c). In contrast to the afforestation, climate change plays a minor role for the relative humidity. In the RCP8.5 and RCP8.5SAH experiment relative humidity at the 700 hPa level slightly decreases over time from the beginning to the end of the 21th century (Fig. 3.4c).

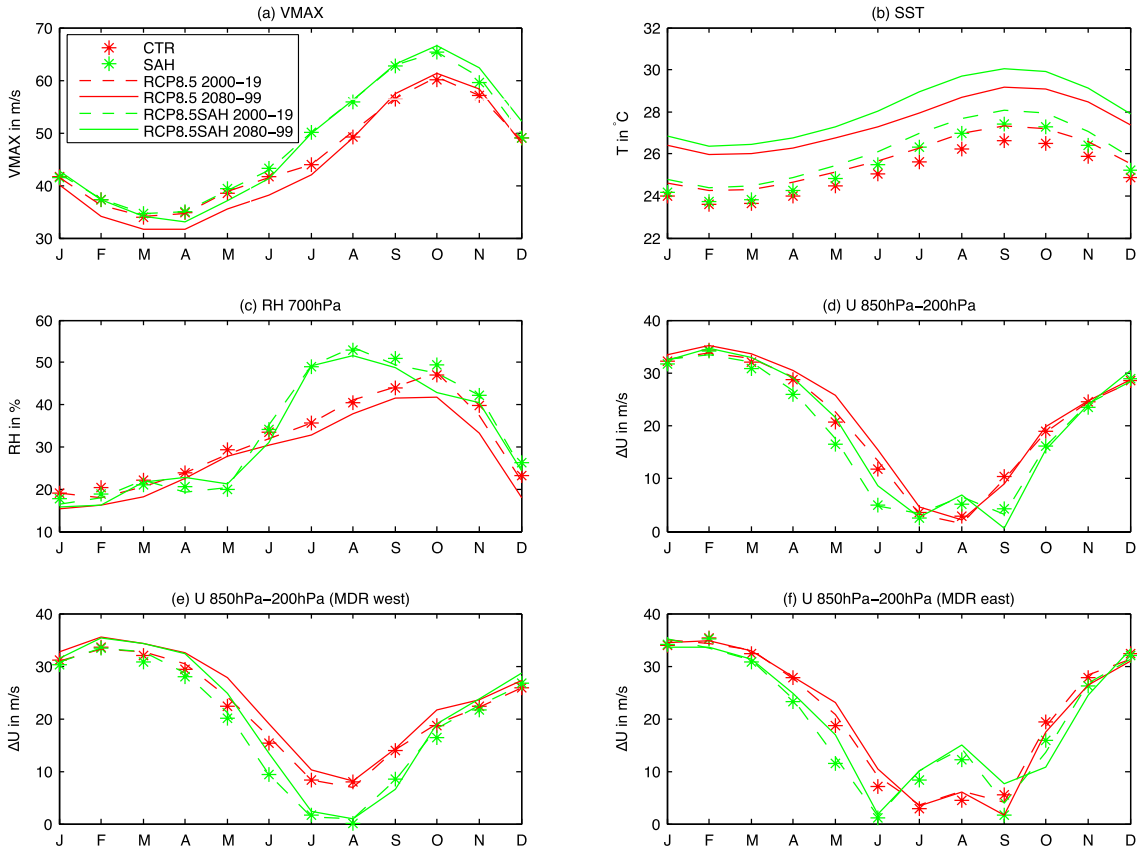

Fig. 3.4 Climatological seasonal cycle of VMAX in m/s (a), SSTs in °C (b), relative humidity in % (c) averaged over the MDR and regional vertical wind shear in m/s calculated as absolute difference of zonal velocities from the 850 and 200 hPa level averaged over the MDR (d), MDR west (e) and MDR east (f) for all four experiments as indicated in the legend. RCP8.5 simulation are averaged from 2000 to 2019 or from 2080 to 2099 respectively.

The annual cycle of the vertical wind shear in CTR is comparable to results from observations (Aiyyer and Thorncroft, 2006). In the afforestation experiments (SAH and RCP8.5SAH) the regional wind shear is generally weaker than in the respective CTR and RCP8.5 experiments with an exception for August (Fig. 3.4d). Wind shear of more than 10 m/s leads to dissipation of TCs (Wong and Chan, 2004; Paterson et al., 2005). The afforestation of the Sahara leads to wind shear below this threshold from June through September, which is a one-month earlier and longer period of suitable wind shear conditions for TCs than in the experiments with afforestation. In the east MDR,

the afforestation leads to enhanced wind shear in July and August (Fig. 3.4f). This is in contrast to the west MDR, where wind shear weakens in July and August (Fig. 3.4e).

3.4 Conclusions and Discussion

Irrigation and afforestation of the Sahara was proposed as a climate engineering method to reduce atmospheric CO_2 concentrations. This method could be technically feasible and beneficial (Ornstein et al. 2009; Bowring et al. 2014), but so far a comprehensive study of its potential negative side effects on climate phenomena has not been conducted. Based on modelling results of the current study, we provide evidence that the environmental conditions in the Atlantic, which will develop from this climate engineering method, would intensify Atlantic TCs. The sensitivity of TC development indices in the MDR to afforestation is examined and compared to model results from a worst-case climate change scenario. Therefore 3 different model experiments are conducted; a worst-case scenario (RCP8.5), a climate-engineering Saharan afforestation scenario (SAH) and a combined global warming plus climate-engineering scenario (RCP8.5SAH). From our model studies we infer that afforestation of the Sahara would lead to an intensification of Atlantic TCs. An intensification of TCs results in more and stronger hurricanes. The number of hurricanes increases under an intensification of TCs, because a larger fraction of TCs would be classified as hurricanes.

The intensification of TCs imply significant costs for society and economy (Narita et al., 2009) and an additional risk for the population, that lives in the areas affected by Atlantic TCs. Trends in observation indicate an intensification of hurricanes in the Atlantic (Webster et al., 2005; Elsner et al., 2008) likely driven by climate change. We show here that afforestation of the Sahara will have a much larger impact on TC development than the impact of the worst-case climate change scenario at the end of this century. This raises the question, whether an irrigated afforested Sahara can be considered as an option for CO_2 removal taking into account the additional risk for life and additional costs due to intensification of TC.

For the afforestation experiments (SAH and RCP8.5SAH), we identified the export of water from the irrigated Sahara into the tropical Atlantic as the main driver for the TC intensification. This additional water export enhances substantially relative humidity over the MDR (Fig. 3.2c), which could drive deep level convection and cloud development. The environmental relative humidity at 700 hPa increases during the months August, September and October with a local maximum of 20% in the central southern MDR. This increase could have a substantial impact on TC development. An increase of 10% in environmental relative humidity could already lead from a weakening TC to a rapidly intensifying one (Wu et al. 2012). The humid air over the MDR perturbs the atmospheric radiation balance. This strengthens the greenhouse effect and reduces ocean to atmosphere latent heat fluxes (not shown). SSTs substantially warm as a response (Fig. 3.2a), which explains the increase in VMAX

(Fig. 3.2b, S3.4a). Geostrophic adjustment of zonal wind velocities (Fig. S3.6) leads to a spatially uniform reduction in vertical wind shear over the MDR with a region of enhanced vertical wind shear in the southeast MDR (Fig. 3.2d). We expect also, that vegetation cover in the Sahara would reduce the export of dust and therefore the dust load over the MDR, which is inversely correlated to TC activity (Evan et al., 2006).

The impact of climate change on TC development is weak in comparison to the impact of the afforestation (compare Fig. 3.2 and Fig. 3.3). SAH shows local maxima in VMAX anomalies of 50 m/s (Fig. 3.2b), whereas the RCP8.5 simulation shows an increase in VMAX of less than 10 m/s (Fig. 3.3b), which is comparable to results from CMIP5 models (Camargo 2013; Ting et al. 2015). In the RCP8.5 simulations the relative humidity at the 700 hPa level tends to decrease in the MDR west and shows no signal in the MDR east.

Our results give reasons to reassess the risk potential of this “green” climate engineering method for afforestation projects with irrigation. Irrigation adds water to the atmosphere, which could act as driver to modify circulation and weather phenomena as we showed in this study.

Acknowledgements:

This work is a contribution to the DFG-funded Priority Program SPP 1689 and was partly performed within the Helmholtz-University Young Investigators Group NATHAN, funded by the Helmholtz-Association and GEOMAR, the Helmholtz Centre for Ocean Research Kiel. The CESM-WACCM simulations have been performed at the Deutsche Klimarechenzentrum (DKRZ) in Hamburg, Germany.

3.5 Supplementary S3

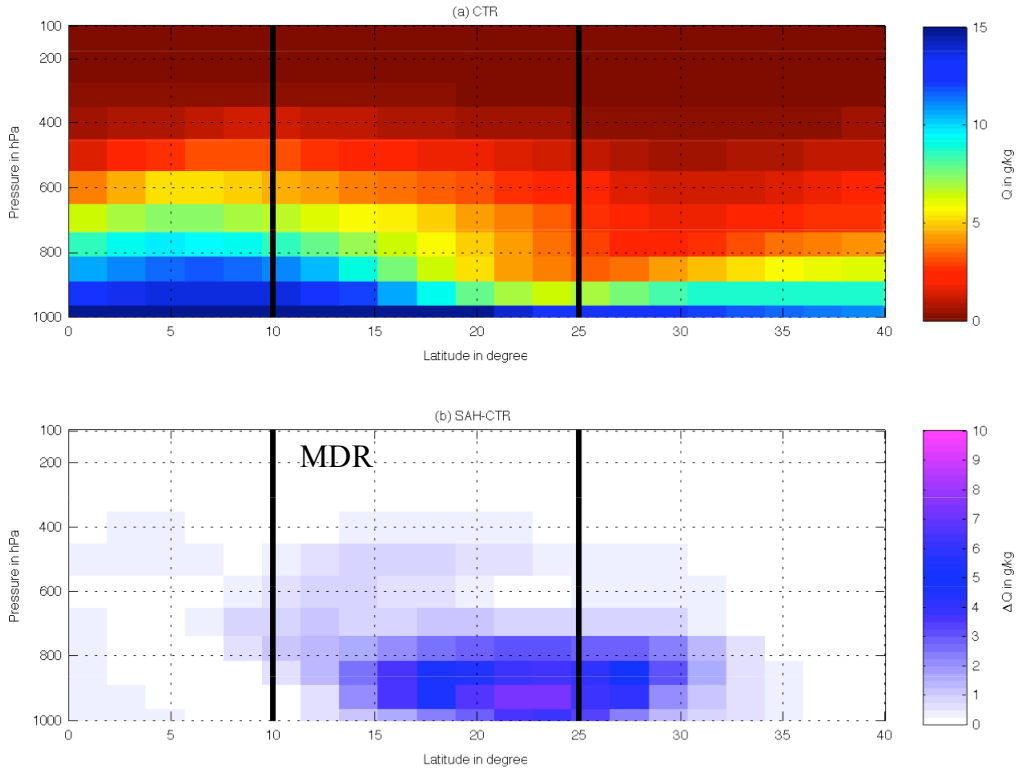

Fig. S3.1 Meridional section of specific humidity in g/kg for the CTR experiment (a) and the differences between the SAH and the CTR experiments (b) at 20°W (Eastern corner of the MDR) averaged over August, September and October. The black lines depict the northern and southern boundary of the MDR.

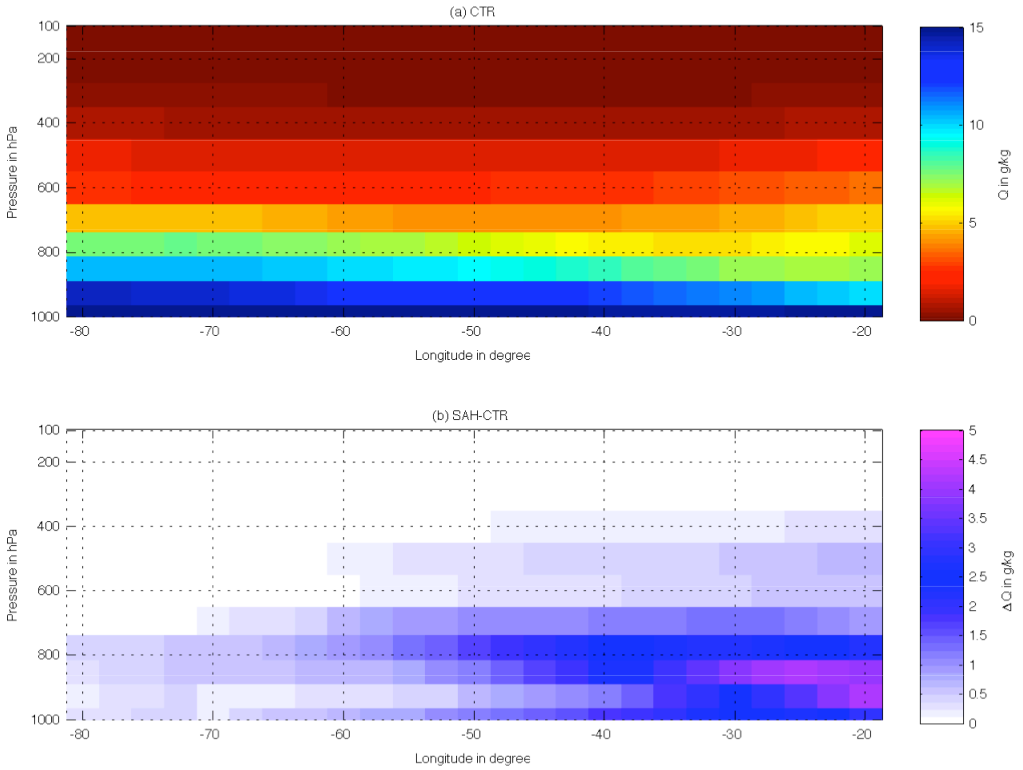

Fig. S3.2 Zonal section of specific humidity in g/kg for the CTR experiment (a) and the differences between the SAH and the CTR experiments (b) averaged meridionally over the MDR and over August, September and October.

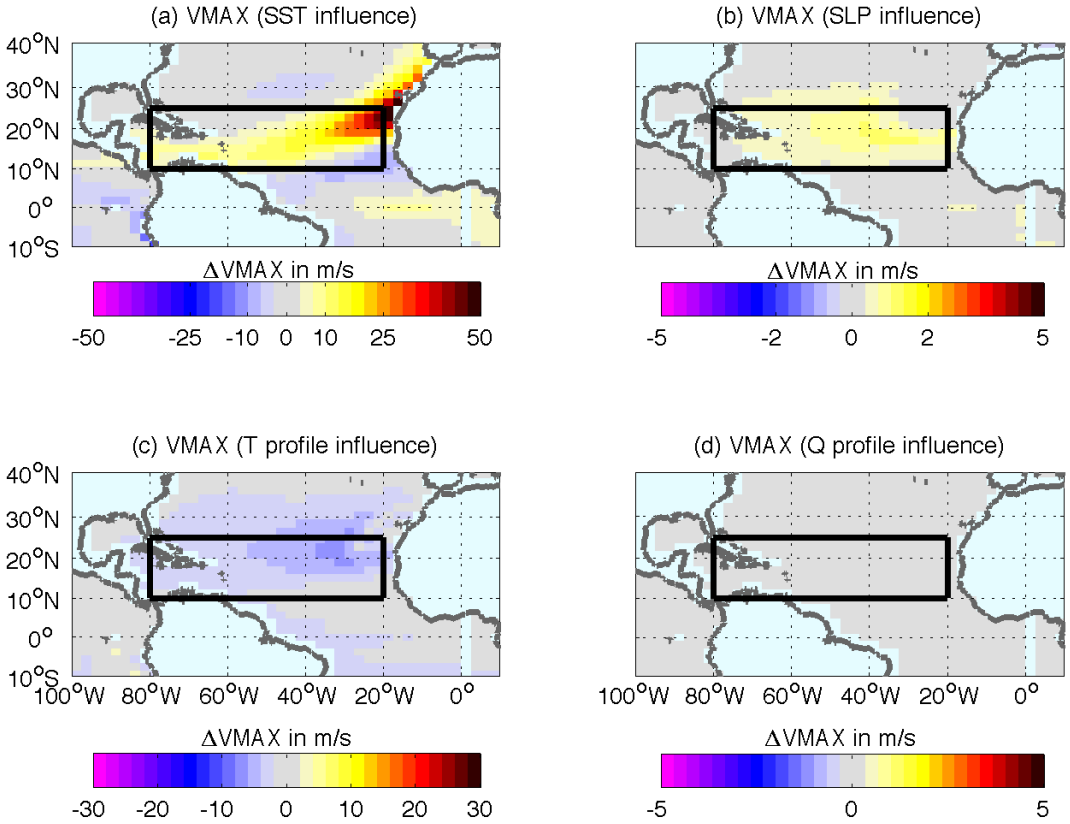

Fig. S3.3 Effect of SSTs (a), sea level pressure (b), temperature profile (c) and humidity profile (d) on VMAX in m/s for SAH minus CTR anomalies (shown in Fig. 5b). For example to calculate the effect of SSTs (a), we use exclusively values from the CTR simulation with exception of SSTs to recalculate the SAH minus CTR anomalies Fig. 5b. SSTs are used from the SAH and CTR simulation, respectively. The black box denotes the MDR.

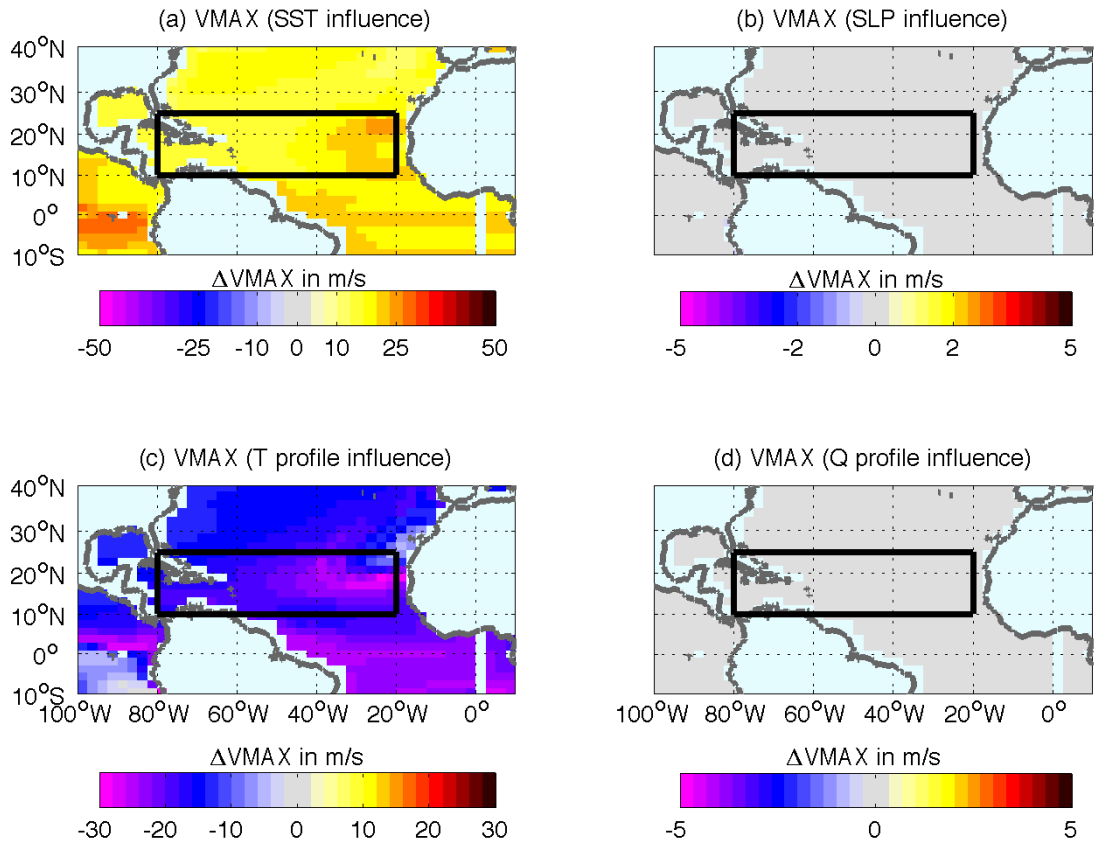

Fig. S3.4 Effect of SSTs (a), sea level pressure (b), temperature profile (c) and humidity profile (d) on VMAX in m/s for RCP8.5 periods 2099-2080 minus period 2019-2000 anomalies (shown in Fig. 6a). For example to calculate the effect of SSTs (a), we use exclusively values from the period 2019-2000 with exception of SSTs to recalculate Fig. 6a. SSTs are used from both periods of the RCP8.5 simulation, respectively. The black box denotes the MDR.

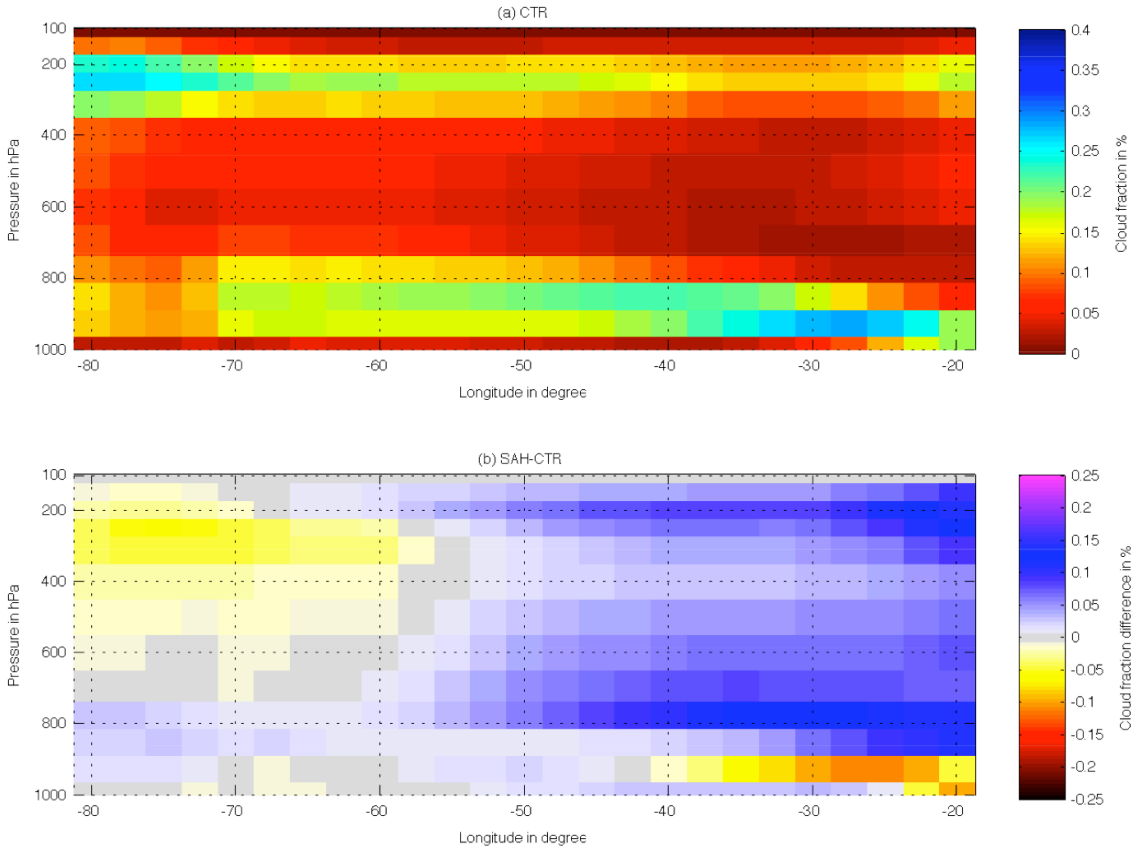

Fig. S3.5 Zonal sections of cloud fraction in % for the CTR experiment (a) and the differences between the SAH and the CTR experiments (b) averaged meridionally over the MDR and from August through October.

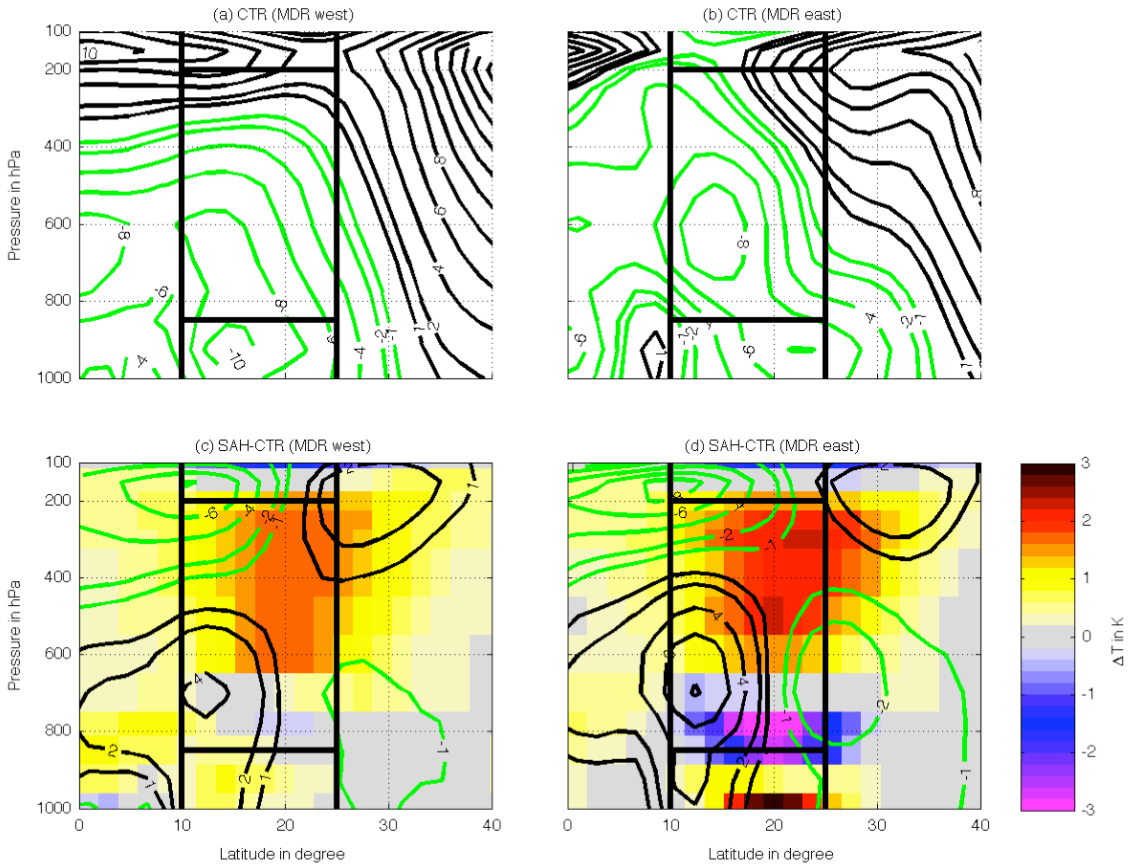

Fig. S3. 6 Meridional section of zonal wind velocities in m/s for the CTR experiment contour lines (a, b) and the differences between the SAH and the CTR experiments, contour lines (c, d) over MDR west (left column) and MDR east (right column) averaged over August, September and October. Differences in atmospheric temperature in K between the SAH and the CTR experiments are shown shaded in (c, d). Vertical black lines depict the meridional extent of the MDR and horizontal black lines depict the 850 and 200 hPa levels.

4. A model study of warming-induced phosphorus-oxygen feedbacks in open-ocean oxygen minimum zones on millennial timescales

Daniela Niemeyer[1] • Tronje P. Kemena[1] • Katrin J. Meissner[2] • Andreas Oschlies[1]

Abstract

Observations indicate an expansion of oxygen minimum zones (OMZs) over the past 50 years, likely related to ongoing deoxygenation caused by reduced oxygen solubility, changes in stratification and circulation, and a potential acceleration of organic matter turnover in a warming climate. The overall area of ocean sediments that are in direct contact with low oxygen bottom waters also increases with expanding OMZs. This leads to a release of phosphorus from ocean sediments. If anthropogenic carbon dioxide emissions continue unabated, higher temperatures will cause enhanced weathering on land, which, in turn, will increase the phosphorus and alkalinity fluxes into the ocean and therefore raise the ocean's phosphorus inventory even further. A higher availability of phosphorus enhances biological production, remineralisation and oxygen consumption, and might therefore lead to further expansions of OMZs, representing a positive feedback. A negative feedback arises from the enhanced productivity-induced drawdown of carbon and also increased uptake of CO_2 due to weathering-induced alkalinity input. This feedback leads to a decrease in atmospheric CO_2 and weathering rates. Here we quantify these two competing feedbacks on millennial timescales for a high CO_2 emission scenario. Using the UVic Earth System Climate Model of intermediate complexity, our model results suggest that the positive benthic phosphorus release feedback has only a minor impact on the size of OMZs in the next 1000 years. The increase in the marine phosphorus inventory under assumed business-as-usual global warming conditions originates, on millennial timescales, almost exclusively (>80%) from the input via terrestrial weathering and causes a 4 to 5-fold expansion of the suboxic water volume in the model.

Daniela Niemeyer
e-mail: dniemeyer@geomar.de
[1] GEOMAR Helmholtz Centre for Ocean Research Kiel, Germany
[2] Climate Change Research Centre and ARC Centre of Excellence for Climate System Science, University of New South Wales, Level 4 Mathews Building, Sydney, New South Wales, 2052, Australia

4.1 Introduction

Oxygen minimum zones (OMZs) have more than quadrupled over the past 50 years and it has been suggested that this expansion is related to recent climate change (Stramma et al., 2008; Schmidtko et al., 2017). However, current CO2 emission-forced models are challenged to reproduce this expansion in detail (Stramma et al., 2012; Cabré et al., 2015). There are at least three different processes that can have an impact on the size of OMZs in a warming climate: ocean warming and its impact on solubility of O2 in the ocean (Bopp et al., 2002), changes in ocean dynamics, e.g. stratification, convective mixing and circulation (Manabe & Stouffer, 1993; Sarmiento et al., 1998), biological production effects (Bopp et al., 2002) including possible CO2-driven changes in stoichiometry (Oschlies et al., 2008) and CO2 induced changes in ballasting particle export (Hofmann & Schellnhuber, 2010). Here we investigate how changes in biological production and subsequent remineralisation can affect OMZs in addition to the above-mentioned thermal and dynamic effects. We focus on changes in the phosphorus (P) cycle. P is the main limiting nutrient on long timescales (Tyrell, 1999; Palastanga et al., 2011) and we examine possible effects of changes in the P cycle on millennial timescales.

The major source of P for the ocean is river input (Filippelli, 2008; Payton & McLoughlin, 2007; Föllmi, 1996, Palastanga et al., 2011; Froelich et al., 1982), which is determined by terrestrial weathering of apatite (Filippelli, 2002; Föllmi, 1996). The main factors controlling terrestrial weathering are temperature, precipitation and vegetation. Higher temperatures are generally associated with enhanced precipitation and in many places with higher terrestrial net primary productivity (Monteiro et al., 2012), which all tend to increase weathering rates (Berner, 1991).

It is difficult to determine how much of the globally weathered P enters the ocean in a bioavailable form. Today, about 0.09-0.15 Tmol a^{-1} of prehuman, potentially bioavailable P is transported globally by rivers including dissolved organic and inorganic P, particulate organic P and ironbound P (Compton et al., 2000). About 25% of this potentially bioavailable P is trapped in coastal estuaries and will not enter the open ocean (Compton et al., 2000). Ruttenberg (2003) estimated a bioavailable P flux under preindustrial conditions including dissolved P and bioavailable particulate P (=35% of total particulate P) of 0.24-0.29 Tmol P a^{-1} excluding the atmospheric input (Ruttenberg, 2003). Marine organisms take up P most easily as dissolved inorganic P (DIP). Riverine measurements suggest that only a small fraction of the total P (0.012 to 0.032 Tmol a^{-1}) enters the ocean as DIP (Filippelli, 2002; Harrison et al., 2005; Compton et al., 2000; Wallmann, 2010; Palastanga et al., 2011; Ruttenberg, 2003). However, passing through estuaries can increase the fraction of DIP by 50% (Froelich, 1984) to 80% (Berner & Rao, 1994).

After taking up the bioavailable P for photosynthetic production of biomass, a large fraction of the newly produced organic matter is exported out of the euphotic zone as detritus (6.42 Tmol P a^{-1} according to the model study by Palastanga et al., 2011) and the vast majority of this exported organic matter is remineralised in the deeper ocean by bacteria (6.26 Tmol P a^{-1}; Palastanga et al., 2011), which is an oxygen consuming process. A small fraction of the exported organic matter is deposited at the sediment surface (0.16 Tmol P a^{-1}; Palastanga et al., 2011), about 20% of the deposited P is buried in the sediments on long time scales (0.032 Tmol P a^{-1}; Palastanga et al., 2011) and the remaining 80% (0.13 Tmol P a^{-1}; Palastanga et al., 2011) is released back into the water column as DIP, where it is again available for the uptake of marine primary producers (Palastanga et al., 2011; Wallmann, 2010).

The processes of burial and release of P are redox-dependent. Under oxic conditions the burial rate is high, while under suboxic conditions the benthic release of P is elevated (Ingall & Jahnke, 1994; Kraal et al., 2012; Wallmann, 2010; Slomp & Van Cappellen, 2007; Flögel et al., 2011; Lenton & Watson, 2000; Tsandev & Slomp, 2009). The redox-dependent release of P into the water column and the decrease in marine oxygen due to remineralisation therefore represent a positive feedback loop on marine biological production (see Fig. 4.1). Although the feedbacks between ocean and atmosphere are complex (Sabine et al., 2004), we assume that an enhanced detritus export into the ocean interior results in an increased marine uptake of atmospheric CO2 (Sarmiento & Orr, 1991). Consequently, surface air temperatures decrease with decreasing atmospheric CO_2 concentrations, which, in turn, leads to lower weathering rates (see Fig. 4.1).

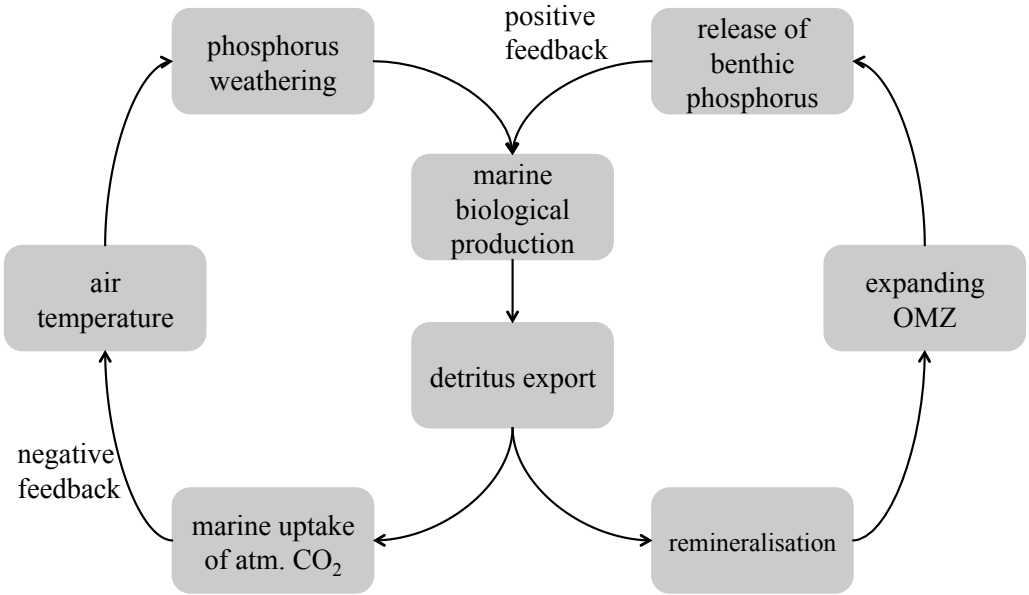

Fig. 4.1: Possible feedbacks in the global phosphorus cycle under climate warming conditions.

These redox-dependent benthic P fluxes have been investigated in a previous study with the HAMOCC global ocean biogeochemistry model by Palastanga et al. (2011). Palastanga et al. (2011) show that doubling the input of dissolved P from rivers results in an increased benthic release of P. This leads to a rise in primary production as well as in oxygen consumption, which in turn affects the oxygen availability in sediments. The benthic release of P acts therefore as a positive feedback on expanding oxygen minimum zones on timescales of 10,000 to 100,000 years (Palastanga et al., 2011).

Other studies on marine oxygen deficiency focused on the geological past, especially the mid-Cretaceous warm period (120-80 Ma ago) (Tsandev & Slomp, 2009; Handoh & Lenton, 2003; Bjerrum et al., 2006; Föllmi et al., 1996). Several periods of oceanic oxygen depletion have been inferred from sediment data of black shales (Schlanger & Jenkyns, 1976), for example for the Cretaceous oceanic anoxic event 2 (OAE) at the Cenomanian-Turonian boundary (93.5 Myrs). Whether processes such as surface warming, sea-level rise (Handoh & Lenton, 2003), and possibly a slow-down of the ocean overturning circulation and vertical mixing (Monteiro et al., 2012; Tsandev & Slomp, 2009; Ruvalcaba Baroni et al., 2014) - as assumed for the Cretaceous - will lead to widespread oxygen depletion in the future, is a reason of concern. Consequently, a better understanding of biogeochemical processes associated with Cretaceous OAE might help assess the risk of possible future events of low marine oxygen concentrations (Tsandev & Slomp, 2009).

In contrast to previous studies that focus on the geological past, we investigate possible future changes over the next 1000 years using an Earth System Climate Model of intermediate complexity to investigate the feedbacks between the P cycle and OMZs under the extended Representative Concentration Pathways-Scenario 8.5 (RCP 8.5) of the Intergovernmental Panel on Climate Change (IPCC) AR5 report. The RCP 8.5 scenario is characterised by an increase in atmospheric CO2 concentrations and associated with an increase in radiative forcing of up to 8.5 W m^{-2} by year 2100 (in comparison to preindustrial conditions) and is also known as the "business as usual" scenario (Riahi et al., 2011).

4.2 Methods

4.2.1 UVic Model

The University of Victoria Earth System Climate Model (UVic ESCM) version 2.9 (Weaver et al., 2001; Eby et al., 2009) is a model of intermediate complexity and consists of a terrestrial model based on TRIFFID and MOSES (Meissner et al., 2003) including weathering (Meissner et al., 2012), an atmospheric energy-moisture-balance model (Fanning & Weaver, 1996), a CaCO3-sediment model (Archer, 1996), a sea-ice model (Semtner, 1976; Hibler, 1979; Hunke & Dukowicz, 1997) and a three-

dimensional ocean circulation model (MOM2) (Pacanowski, 1996). The ocean model includes a marine ecosystem model based on a nutrient-phytoplankton-zooplankton-detritus model (Keller et al., 2012). The horizontal resolution of all model components is 1.8° latitude x 3.6° longitude. The ocean model has 19 layers with layer thicknesses ranging from 50 m at the sea surface to 500 m in the deep ocean. We use a sub-grid scale bathymetry as described in Somes et al. (2013) to simulate benthic fluxes of phosphorus. The sub-grid bathymetry is inferred from the ETOPO2v2[https://www.ngdc.noaa.gov/mgg/global/etopo2.html] and represents global spatial distributions of continental shelves, slopes and other topographical features (1/5°). For the topography used here, the shelf (0-200 m) covers 6.5%, the slope (200-2000 m) 11.7% and the deep sea (>2000 m) 81.9% of the global ocean. Downward fluxes of organic matter are intercepted by the sub-grid bathymetry related to the fractional sediment cover for each ocean grid box, and benthic fluxes of phosphorus are calculated based on the transfer functions described in the following section.

4.2.2 Phosphorus Cycle in UVic Model

Earlier applications of the UVic ESCM assumed a fixed marine P inventory. We included a representation of the dynamic P cycle for this study. It consists of a modified terrestrial weathering module (Meissner et al., 2012) and a redox-sensitive transfer-function for burial and benthic release of P (Flögel et al., 2011; Wallmann, 2010).

The continental-weathering module developed earlier for fluxes of dissolved inorganic carbon (DIC) and alkalinity (Meissner et al., 2012; Lenton & Britton, 2006), is based on the following equations:

$$F_{DIC,w} = F_{DIC,w,0} * \lfloor f_{Si} + f_{Ca} \cdot \left(\frac{NPP}{NPP_0}\right) \cdot \left(1 + 0.087 * (SAT - SAT_0)\right) \rfloor \quad (4.1a)$$

$$F_{DIC,w} = F_{DIC,w,0} * f(NPP, SAT) \quad (4.1b)$$

$$F_{Alk,w} = F_{Alk,w,0} * \left(\frac{NPP}{NPP_0}\right) \cdot \lfloor f_{Si} * (1 + 0.038) * (SAT - SAT_0) * 0.65^{0.09} * (SAT - SAT_0) \rfloor + f_{Ca} * \left(1 + 0.087 * (SAT - SAT_0)\right) \quad (4.2)$$

Where $F_{DIC,w}$ and $F_{Alk,w}$ represent the globally integrated flux of DIC and alkalinity via river runoff, f_{Si} and f_{Ca} stand for the fraction of silicate (0.25) and carbonate (0.75) weathering, and NPP and SAT are the global mean net primary production on land and global mean surface air temperature over land (in degrees Celsius). The index 0 stands for preindustrial values.

We added the following flux to account for P weathering ($F_{DP,w}$) with the same dependencies on globally and annually averaged net primary production (NPP) and surface air temperature (SAT) as those for DIC:

$$F_{DP,w} = F_{DP,0} * f(NPP, SAT) \quad (4.3)$$

The global river input of dissolved inorganic P (DIP) is the only continental source for P in the model. The global DIP input is distributed over all coastal points of discharge scaled according to their individual volume discharge. The pre-industrial DIP input to the ocean ($F_{DP,0}$) is assumed to be in steady state and in equilibrium with the total globally integrated preindustrial net burial of P ($BUR_{P,0}$):

$$F_{DP,0} = BUR_{P,0} \tag{4.4}$$

We use an empirical transfer function for BUR_P and for the benthic release of DIP (BEN_{DIP}) derived from observations across bottom-water oxygen gradients (Wallmann, 2010; Flögel et al., 2011). The release of dissolved inorganic P (BEN_{DIP}) is calculated as follows:

$$BEN_{DIP} = \frac{BEN_{DIC}}{r_{reg}} \tag{4.5}$$

Benthic release of dissolved inorganic carbon (BEN_{DIC}) is calculated from an empirical transfer function (Fig. 4.2 in Flögel et al., 2011) to determine BEN_{DIP} fluxes at the ocean bottom. In our model configuration POC is remineralised completely at the ocean bottom and no ocean-to-sediment-fluxes of POC occur, i.e. $BEN_{DIC} = RR_{POC}$, where RR_{POC} denotes the rain rate of particulate organic carbon to the sediment. Wallmann (2010) calculated r_{reg} by a regression of observational data to bottom-water oxygen concentrations:

$$r_{reg} = \frac{RR_{POC}}{BEN_{DIP}} = Y_F + A * exp\left(\frac{-[O_2]}{r}\right) \tag{4.6}$$

The regeneration ratio is calculated by dividing the depth-integrated rate of organic matter degradation in surface sediments (RR_{POC}) by the benthic flux of dissolved inorganic P into the bottom water (BEN_{DIP}). Parameters are defined as $Y_F = 123 \pm 24$, $A = -112 \pm 24$ and $r = 32 \pm 19$ and O_2 is in µmol/l (Wallmann, 2010). Under oxic conditions r_{reg} is higher than the Redfield ratio (106; Redfield et al., 1963) and under oxygen-depleted conditions r_{reg} reduces to 10 (Wallmann, 2010).

The rain rate of POP (RR_{POP}) is calculated by the rain rate of POC (RR_{POC}) divided by the Redfield ratio. As a result BUR_P can be calculated as follows:

$$BUR_P = RR_{POP} - BEN_{DIP} \tag{4.7}$$

The burial of P (BUR_P) in the sediment is equal to the rain rate of particulate organic P (RR_{POP}) minus BEN_{DIP} (Flögel et al., 2011). If the benthic release overcomes the rain rate of POP at depths below 1000 m, the burial is set to zero. Following Flögel et al. (2011), this condition is not applied to shallower sediments because these deposits receive both marine particles and high fluxes of riverine particulate phosphorus.

4.3 Model Simulations

Two model simulations were performed. Our control simulation, called simulation REF hereafter, includes neither weathering, benthic release, nor burial of P. The global amount of P in the ocean is therefore conserved in this simulation over time. The second simulation, called WB, includes P weathering as well as benthic burial and release of P but excludes additional anthropogenic input. The spin up was performed by computing the burial and benthic release according to Eq. (4.6). The weathering fluxes were set to a value to compensate the burial rate (Eq. 4.4) during the spin up but not thereafter.

After a spin-up of 20,000 years under preindustrial boundary conditions, we forced the model with anthropogenic CO_2 concentrations following the RCP 8.5 scenario of the IPCC AR5 assessment (Meinshausen et al., 2011; Riahi et al., 2011). The CO_2 emissions in the UVic ESCM reach 105.6 Pg CO_2 a^{-1} in year 2100. Between years 2100 and 2150 the models are forced with constant CO_2 emissions (105 Pg CO_2 a^{-1}), followed by a linear decline until year 2250 to a level of 11.5 Pg CO_2 a^{-1} and then linearly to zero emissions in year 3005 (see Fig. 4.2a). Simulated atmospheric CO_2 concentrations peak in year 2250 with 2148.6 ppmv and equal 1835.8 ppmv in year 3005 (see Fig. 4.2a).

4.4 Simulated preindustrial equilibrium

The UVic ESCM has been validated under present day and preindustrial conditions in numerous studies (Eby et al., 2009; Weaver et al., 2001). In particular, Keller et al. (2012) recently compared results of its ocean biogeochemical component to observations and previous model formulations. We therefore concentrate our validation on the new model component in this study, the P cycle.

Estimates of preindustrial burial rates vary over a wide range in the literature. The comprehensive review by Slomp (2011) reported a burial rate of 0.032-0.35 Tmol P a^{-1} for the total ocean while Baturin (2007) suggests a burial rate of 0.419 Tmol P a^{-1} based on observational data described in detail by Wallmann (2010). The burial rate diagnosed by the UVic ESCM in simulation WB for the total ocean under preindustrial boundary conditions (0.38 Tmol P a^{-1}), is within range of these earlier estimates. The burial at the continental margin (0-200 m) accounts for 50-84% of total burial corresponding to 0.016-0.175 Tmol P a^{-1} calculated in Slomp (2011). Ruttenberg (2003) estimated a burial rate at continental margins of 0.15-0.22 Tmol P a^{-1}, while the UVic ESCM calculated a burial rate of 0.33 Tmol P a^{-1} for the continental margins in year 1775. The open ocean burial contributes only a minor part to total burial (0.04-0.13 Tmol P a^{-1}; Ruttenberg, 2003; in the UVic it is 0.046 Tmol P a^{-1}).

To conserve marine P during long model spin ups, the dissolved weathering flux of P under preindustrial conditions is set equal to the diagnosed total burial rate during the spin-up, 0.38 Tmol P a^{-1}. Following the method of calculating the reactive P flux (defined in Ruttenberg (2003) as the sum of >50% of TDP (=DOP) plus 25-40% of

particulate P flux), our result fits well with estimates summarised by SLOMP (2011) ranging from 0.13 Tmol P a^{-1} (natural P flux) to 0.36 Tmol P a^{-1} (modern P flux) and Ruttenberg (2003) (0.16-0.32 Tmol P a^{-1}).

Global values for benthic release under preindustrial conditions equal 0.78 Tmol P a^{-1} in the UVic ESCM (simulation WB), while Ruttenberg (2003) described a range from 0.51 Tmol P a^{-1} to 0.84 Tmol P a^{-1} based on pore water measurements (Colmann & Holland, 2000) for coastal regions. For the deep sea Colmann & Holland (2000) specified the benthic release value with 0.41 Tmol P a^{-1}. In the UVic ESCM the benthic release for continental margins was calculated as 0.4816 Tmol P a^{-1} and for the open ocean as 0.2951 Tmol P a^{-1}.

4.5 Results

4.5.1 Simulated Climate

The global mean atmospheric surface temperature, as simulated by the WB run, increases until year 2835 and peaks at 23.1°C, i.e. 9.9°C above pre-industrial levels. Simulation REF shows similar changes in temperature with an increase until year 2855 and a peak at 23.3°C (see Fig. 4.2a). Both simulations show a slight recovery in temperatures after the peak (REF: 23.2°C; WB: 23.1°C; year 3005). Atmospheric temperatures in the WB-simulation are slightly lower than in the reference simulation, due to slightly lower carbon dioxide concentrations in the atmosphere, caused by increased global ocean alkalinity (REF: 2.498 mol m^{-3}; WB: 2.481 mol m^{-3}; both for year 3005), the enhanced biological pump and a rise in detritus export rate (see Sect. 3.2), and therefore increased marine uptake of atmospheric CO_2. The impact of the negative feedback via enhanced biotically and chemically induced marine uptake of atmospheric CO_2 on surface air temperatures is thus small compared to the CO_2 induced warming in a high-emission scenario.

Given that the response in temperature is similar for both simulations compared to considerable differences in biological productivity (see below), differences in oxygen concentration mainly originate from biogeochemical changes, which will be discussed in Sect. 3.3.

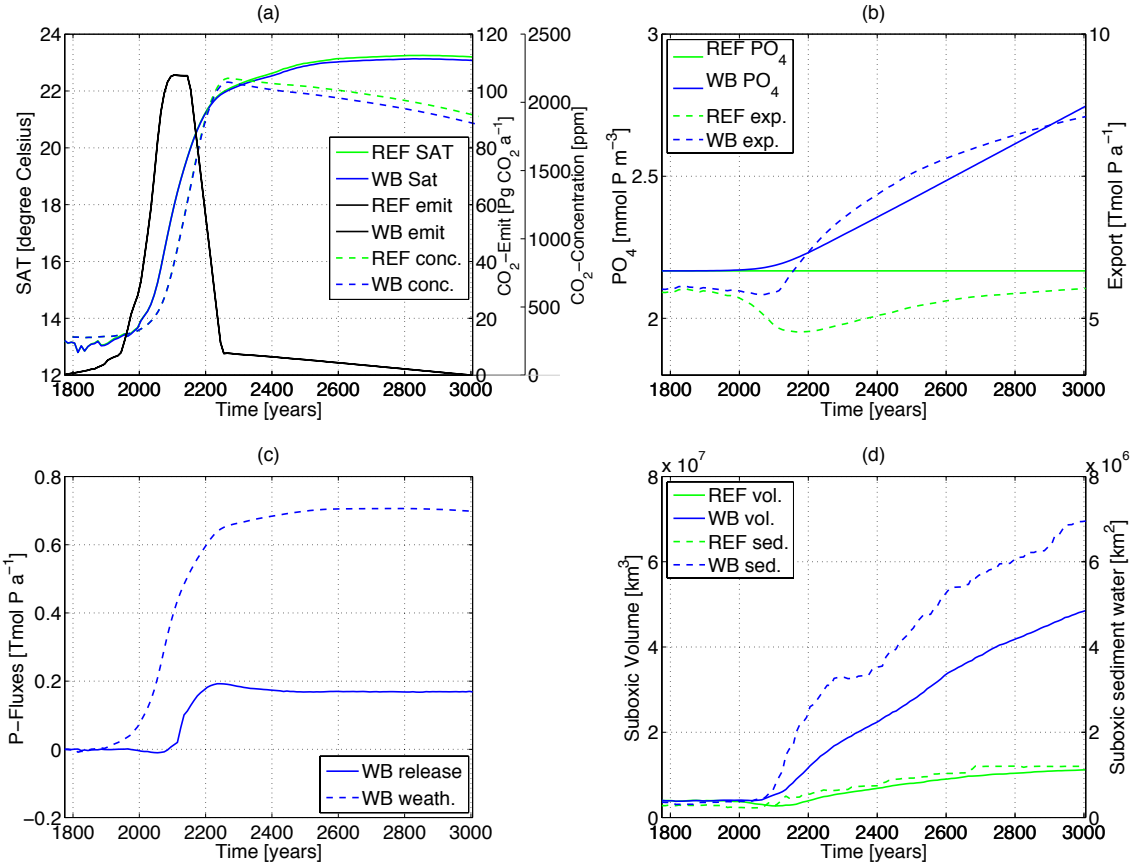

Fig. 4.2: Global and annual mean time series of (a) surface air temperature in degree Celsius (solid lines), CO_2-emissions in Pg CO_2 a^{-1} (black solid line (for both simulations)) and CO_2-concentration in ppm (dashed lines); (b) global mean phosphorus concentration in mmol P m^{-3} (solid lines) and export rate in Tmol P a^{-1} at 130 m depth (dashed lines); (c) anomalies of phosphorus input via sediment in Tmol P a^{-1} (solid line) and anomalies of phosphorus weathering input in Tmol P a^{-1} (dashed line); (d) suboxic volume (<0.005 mol m^{-3}) of the ocean in km^3 (solid lines) and surface of ocean bottom layer with O_2 concentrations below 0.005 mol m^{-3} in km^2 (dashed lines). The control simulation (REF) is shown in green, simulation WB in blue.

4.5.2 Phosphorus Dynamics

The weathering rate (see Fig. 4.3b) and associated flux of P into the ocean via river discharge more than doubles relative to the pre-industrial situation in our WB-simulation and leads to an enhancement in global mean oceanic P concentrations by 27% over 1000 years (see Fig. 4.2b). At the same time, benthic burial acts as the only P sink in our model (see Fig. S4.1), mitigating the total increase in marine P. The P concentration remains constant in the control run REF.

The weathering input in the WB-simulation is largest north of 30°N (0.338 Tmol P a^{-1} in year 3005; see Fig. 4.3a), while south of 30°S (0.138 Tmol P a^{-1}) and in the low latitude Pacific Ocean the input is lowest (0.117 Tmol P a^{-1}). Weathering fluxes into the low latitude Indian and Atlantic Oceans equal 0.187 and 0.267 Tmol P a^{-1}, respectively.

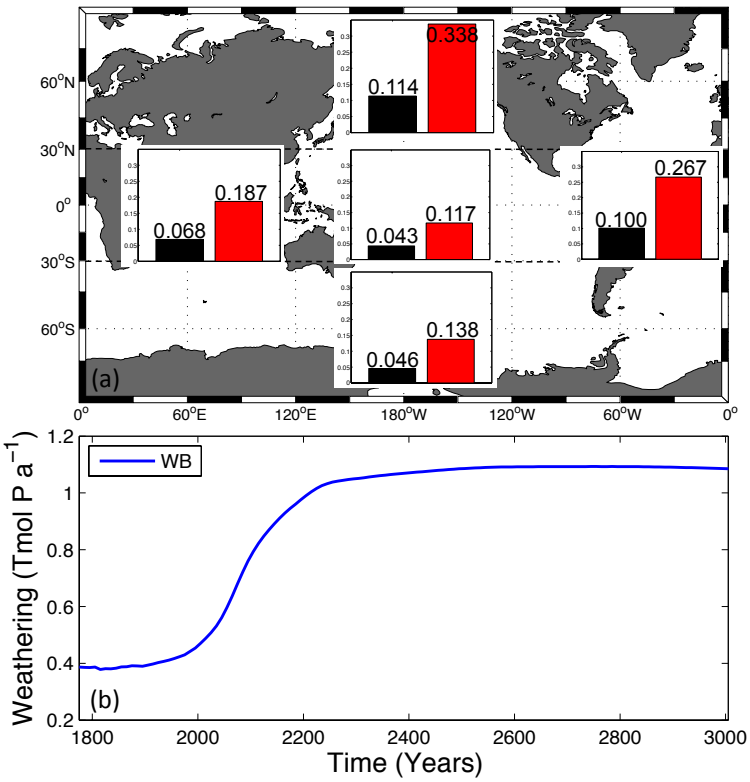

Fig. 4.3: (a) Phosphorus weathering input (in Tmol a^{-1}) into the tropical Pacific Ocean (middle), tropical Atlantic Ocean (right, middle), tropical Indian Ocean (left, middle), Northern Oceans (=oceans north of 30° N; upper middle) and Southern Ocean (=ocean south of 30° S; lower middle) in 1775 (black bars) and 3005 (red bars). (b): Annual mean averaged phosphorus weathering input (global sum) of 1775 until year 3005.

Increasing P concentrations as well as climate warming result in an increase in net primary production in the ocean (ONPP). Globally integrated ONPP ranges between 43.8 Tmol P a^{-1} (REF) and 44.1 Tmol P a^{-1} (WB) under preindustrial conditions and 65 Tmol P a^{-1} (REF) and 116.4 Tmol P a^{-1} (WB) at year 3005 (see Fig. S4.1). The main areas of ONPP increase are located in the tropical ocean, where higher temperatures favour net primary production in the model (results not shown).

Due to enhanced P inventory and enhanced ONPP, the WB-simulation also has a higher export rate (8.6 Tmol P a^{-1}, computed at 130m depth; see Fig. 4.2b) when compared to the reference run (5.5 Tmol P a^{-1}) in year 3005. In the REF simulation, the export rate declines until year 2175 (4.8 Tmol P a^{-1}) in response to enhanced stratification, associated declining nutrient supply and stronger nutrient recycling in the upper layers (Schmittner et al., 2008; Steinacher et al., 2010; Bopp et al., 2013; Moore et al., 2013; Yool et al., 2013; Kvale et al., 2015). The export rate recovers to reach 5.5 Tmol P a^{-1} at the end of the simulation in experiment REF.

The globally integrated remineralisation rate in the aphotic zone (results not shown) ranges between 5.1 Tmol P a^{-1} (WB) and 5.2 Tmol P a^{-1} (REF) in year 1775. Simulation WB is characterized by a strong increase in remineralisation until 3005 with a

maximum of 8.1 Tmol P a^{-1} (in year 3005), while in the reference run the remineralisation rate first decreases, followed by a moderate increase to 5.3 Tmol P a^{-1}. Regions with highest remineralisation are located on the continental margins, especially in the Indian Ocean.

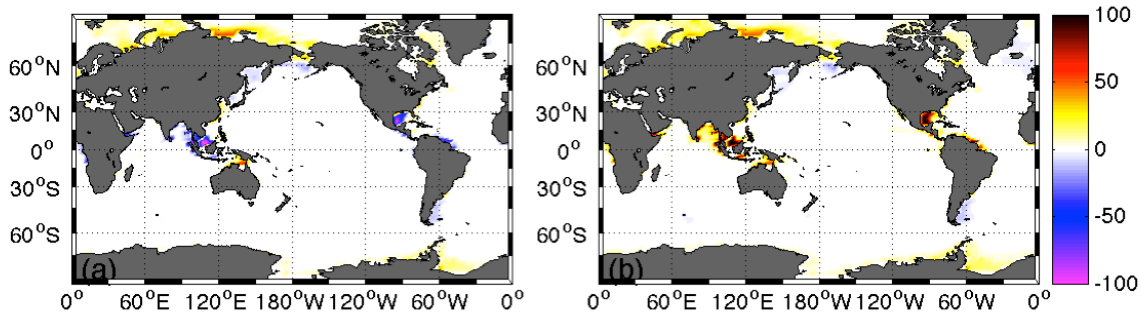

Fig. 4.4: Difference (year 3005 minus year 1775) in (a) burial and (b) benthic release flux in mmol P m^{-2} a^{-1} for simulation WB.

The P burial in the WB-simulation equals 0.38 Tmol P a^{-1} in year 1775 and decreases by 44.3% to 0.2 Tmol P a^{-1} in year 3005 (see Fig. S4.1). One reason for this decrease is the redox-state of the bottom water. The strong expansion of the area of ocean bottom waters with O_2 concentrations below 0.005 mol m^{-3} (see Fig. 4.2d) in the WB simulation leads to a decrease in benthic burial of P despite an increase in the rain rate of particulate organic P, RR_{POP}. In general, burial rates are largest along the coastal margins, where 87.9% of the total flux is buried in 1775. Highest increases in burial rates between years 1775 and 3005 are located in the Arctic Ocean (see Fig. 4.4a), whereas burial rates decrease in the Bay of Bengal and the Gulf of Mexico where low-oxygen bottom waters expand (see Fig. 4.5).

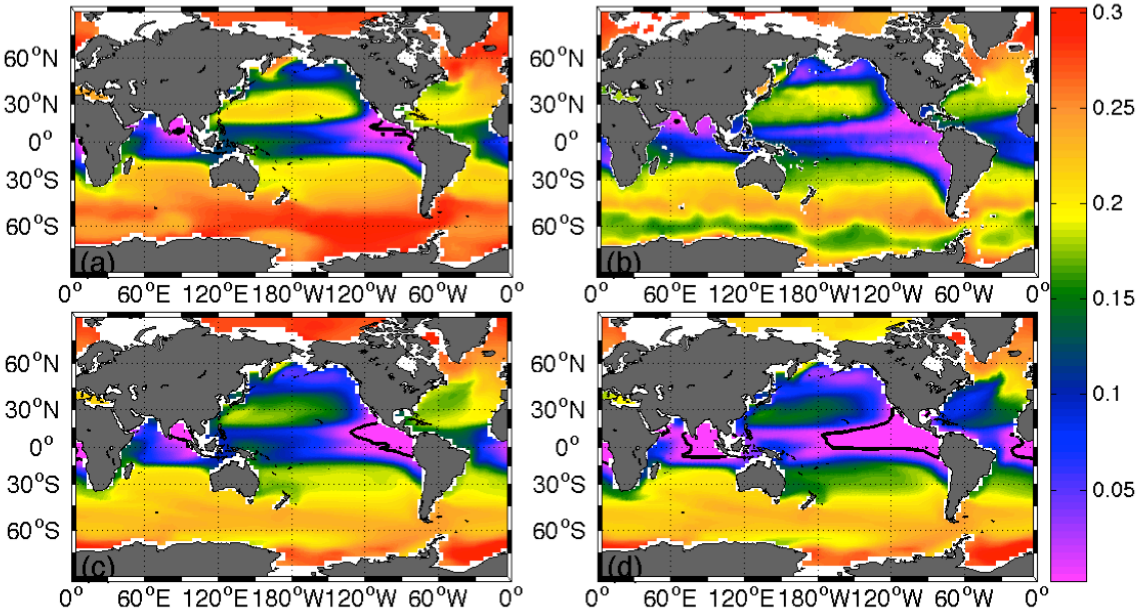

Fig. 4.5: Oxygen concentration in mol O_2 m^{-3} at 300m depth simulated by the (a) control simulation at year 1775 (representative for both REF and WB model runs in year 1775), (b) the World Ocean Atlas in 2009, (c) the control

simulation at year 3005 and (d) simulation WB at year 3005. The black contour lines at 0.005 mol m^{-3} highlight the oxygen minimum zones (OMZs).

The benthic P release in the WB simulation increases by 119% until year 3005 to 1.7 Tmol P a^{-1} (see Fig. S4.1). As mentioned above, the benthic release is a redox-dependent process, which commonly takes place at the coastal margins (Wallmann, 2010; in our model under preindustrial conditions 62% of total release is from coastal margins). This means that an increase in suboxic bottom water area (see Fig. 4.2d) leads to an enhanced release of benthic P in WB. A rapid increase between years 1775 and 3005 can be found in the Bay of Bengal, the Gulf of Mexico and in the Arctic Ocean (see Fig. 4.4b).

In our model simulations, both the weathering-induced P flux into the ocean (see Fig. 4.2c) as well as the net P released from the sediments (see Fig. 4.2c) show a strong increase under continued global warming, which explains the increase in the marine P inventory in the WB simulation (see Fig. 4.2b). However, the simulated increase in the weathering input has a much stronger (about 4 times larger) impact on the P budget and therefore on the expansion of OMZs than the benthic release feedback (see Fig. 4.2c). We note that even at the end of the thousand-year simulation, the P cycle has not yet reached a new steady state in experiment WB. Weathering rates are high in the warm climate and burial of P has not increased to counteract the supply by weathering (see Fig. 4.3b and S4.1). The release of P from sediments also adds to this imbalance. As a result, the marine P inventory is still increasing almost linearly at the end of our simulation. Extending the simulation until year 10,000 reveals that the ocean - as well as the coastal regions - do not become anoxic despite a more than 3-fold increase in oceanic P inventory (see Sect. 4.3.3 and Fig. S4.2) while the P cycle still exhibits a strong imbalance between sources and sinks.

4.5.3 Oxygen Response

The black contours in Fig. 4.5 indicate the lateral extent of OMZs for a depth of 300 m (see Fig. S4.3 for a depth of 900 m). In year 1775, the suboxic volume, defined here as waters with oxygen concentrations of less than 5 mmol m^{-3}, equals 3.9×10^6 km^3 in both simulations (see Fig. 4.2d). An observational estimate of today's suboxic water volume equals $102 \times 10^6 \pm 15 \times 10^6$ km^3 for oxygen concentrations less than 20 mmol m^{-3} (Paulmier & Ruiz-Pino, 2009), which is considerably larger than the volume of O_2<20 mmol m^{-3} waters in our WB-simulation ($WB_{2005} = 15.8 \times 10^6$ km^3). However, in consideration of the studies of BIANCHI ET AL. (2012) and their calculated OMZ volume of $2.28\text{-}2.78 \times 10^6$ km^3, as well as World Ocean Atlas ($WOA_{2005} = 4.12 \times 10^5$ km^3), it can be concluded that estimations of the volume of OMZs vary over a wide range and that our results are within this range. Comparing our results with observational data from the WOA, a generally good agreement can be found with regard to the spatial distribution

of low-oxygen waters (see Fig. 4.5). The suboxic areas are located in the upwelling regions of the tropical eastern Pacific and eastern Atlantic as well as in the Indian Ocean (see Fig. 4.5; representative for both simulations in 1775).

During our transient simulations, we find a considerable expansion of OMZs until year 3005 in both simulations (see Fig. 4.2d and Fig. 4.5). The expansion of the suboxic volume between 300 and 900 m is particularly pronounced in the WB simulation where the OMZs account for 4.85×10^7 km^3 in year 3005, i.e. an increase by a factor 12.4. The control simulation (REF) shows a much smaller increase in the volume of OMZs (1.12×10^7 km^3 between 300 and 900 m depth). As both simulations display similar climates (see Fig. 4.2a), the difference in the oxygen fields is largely due to the differences in the simulated P cycle.

The sea-floor area in contact with suboxic bottom waters, which directly impacts the redox-sensitive benthic burial and P release, shows an increase by more than a factor of 19 ($WB_{1775}=3.59 \times 10^5$ km^2; $WB_{3005}=6.95 \times 10^6$ km^2) in the WB simulation (see Fig. 4.2d) compared to a factor of 4 increase in the REF simulation ($REF_{1775}=2.79 \times 10^5$ km^2; $REF_{3005}=1.2 \times 10^6$ km^2). Our present-day results ($WB_{2005} = 3.8 \times 10^5$ km^2) compare well with data of the WOA ($WOA_{2005} = 2.48 \times 10^5$ km^2).

Somewhat unexpectedly, in our study an increase in continental weathering does not result in an anoxic ocean under current topography and seawater chemistry - at least not until year 10,000. At the preindustrial state (year 1775), 0.12% of all coastal margins are characterized by oxygen concentrations below 0.005 mol m^{-3}. While this portion increases by about a factor of 50 to 5.57% by year 3005, this is too low for the generation of widespread coastal anoxia. Conversely, the global mean oxygen concentration starts to increase again in year 3415 when it has reached a minimum of about two thirds of the pre-industrial oxygen inventory in the WB simulation (see Fig. S4.1). This suggests that the positive feedback between the release of benthic P and marine net primary production is - in this study for present day bathymetry and geography - not the decisive factor for a rapid transition into an anoxic ocean.

4.6 Uncertainties

Although the model's subcomponents for weathering, burial and benthic release rates are highly simplified in this study, the simulated global P fluxes fall within the range suggested by earlier studies and observational estimates (Palastanga et al., 2011; Filippelli, 2002; Baturin, 2007; Wallmann, 2010). The weathering fluxes are calibrated against global mean burial rates under an implicit steady-state assumption, although it is unclear whether the pre-industrial P cycle in the ocean was in equilibrium (Wallmann, 2010). The relatively high P weathering fluxes as well as the assumed indefinite P reservoir in the shelf sediments in our simulations might lead to an overestimation of the effects on the P cycle and OMZs.

In our model, the increase in the P inventory results in a strong increase in ONPP. Contrary to other studies, e.g. Gregg et al. (2005) or Boyce et al. (2010), in our study the temperature effect overcompensates the stratification effect as described by Sarmiento et al. (2004), Taucher & Oschlies (2011) and Kvale et al. (2015) and thus leads to an increase in ONPP also in the reference run. While the net effect of warming on ONPP is not well constrained and differs considerably among models, the impact of changing environmental conditions on export production appears to be better constrained (Taucher & Oschlies, 2011). In agreement with simulations by other models, experiment REF shows a stratification-induced decline in export production, while the increase in P induces an increase in export production in WB. Although we use a coarse resolution model, the applied sub-grid scale bathymetry allows the calculation of more accurate benthic burial and release fluxes than otherwise possible with such a model. It should also be noted that the benthic release feedback on OMZs might have been more efficient under Cretaceous boundary conditions because the shelf area was considerably larger due to higher sea levels (late Cretaceous shelf area: 46×10^6 km^2; present day shelf area: 26×10^6 km^2 (Bjerrum et al., 2006)). Cretaceous topography might therefore have induced a stronger benthic release feedback as shown in Tsandev & Slomp (2009).

Filippelli (2002) showed in his study that due to the anthropogenic activities the global, total present-day river input of P has doubled in the last 150 years. In our study the direct anthropogenic influence, such as agricultural input of P into the system, is excluded and should be considered in future studies even though the human impact is projected to decrease until year 3500 (Filippelli, 2008). Filippelli (2008) and Harrison et al. (2005) estimated a rate of 0.03 Tmol P a^{-1} and 0.7 Tg P a^{-1} (=0.023 Tmol P a^{-1}), respectively, for anthropogenic P delivered to the ocean as a result of fertilization, deforestation and soil loss as well as sewage in year 3000. In comparison to our simulated maximum weathering value of 1.09 Tmol P a^{-1} until year 3005, the direct anthropogenic impact seems to be small.

4.7 Conclusions

This study constitutes a first approach to estimate the potential impact of changes in the marine P cycle on the expansion of global ocean OMZs under global warming on millennial time scales. Model simulations show that the warming-induced increase in terrestrial weathering (see Fig. 4.3b) leads to an increase in marine P inventory (see Fig. 4.2b) resulting in an intensification of the biological pump, corroborating the findings by Tsandev & Slomp (2009). As a consequence, oxygen consumption as well as the volume of OMZs increase in our simulations by a factor of 12 over the next millennium (see Fig. 4.2d and 4.5).

The positive feedback involving redox-sensitive benthic P fluxes - where the expansion of OMZs leads to an increase in benthic release of P (see Fig. 4.2c and Fig. S4.1), which in turn enhances biological production and subsequent oxygen consumption (Wallmann 2010) - has only limited relevance for the expansion of OMZs in this study. Instead, a negative feedback dominates that involves enhanced weathering and P supply to the ocean, an intensification of the biological carbon pump and associated marine uptake of atmospheric CO_2. The atmospheric CO_2 impacts the surface air temperature through a negative feedback loop, which limits the warming and weathering and, eventually, the expansion of the OMZs. We can therefore conclude that, based on the parameterizations used in this study, the P weathering and biological pump feedback outcompetes the redox-sensitive benthic P-release feedback on millennial timescales. Although the ocean does not become anoxic in our simulations, the benthic P-release feedback may have played a role in past oceanic anoxic events. An increase in shelf areas due to higher sea levels, such as during the Cretaceous, would have led to a more powerful benthic P-release feedback as a much larger sediment area could have been in contact with low-oxygen bottom waters. Whether this different bathymetry alone could result in a more dominant benthic P-release feedback needs to be investigated in future studies.

Acknowledgments

The model data will be available at:

http://data.geomar.de/thredds/catalog/open_access/niemeyer-et-al_2016/catalog.html.

This work is a contribution to the Sonderforschungsbereich (SFB) 754 “Climate-Biogeochemical Interactions in the Tropical Ocean” and the BMBF project PalMod. We thank M. Eby for his excellent help with the UVic ESCM and K. F. Kvale and J. Getzlaff for proofreading. KJM is thankful for UNSW Science Silver- and Goldstar Awards.

4.8 Supplementary S4

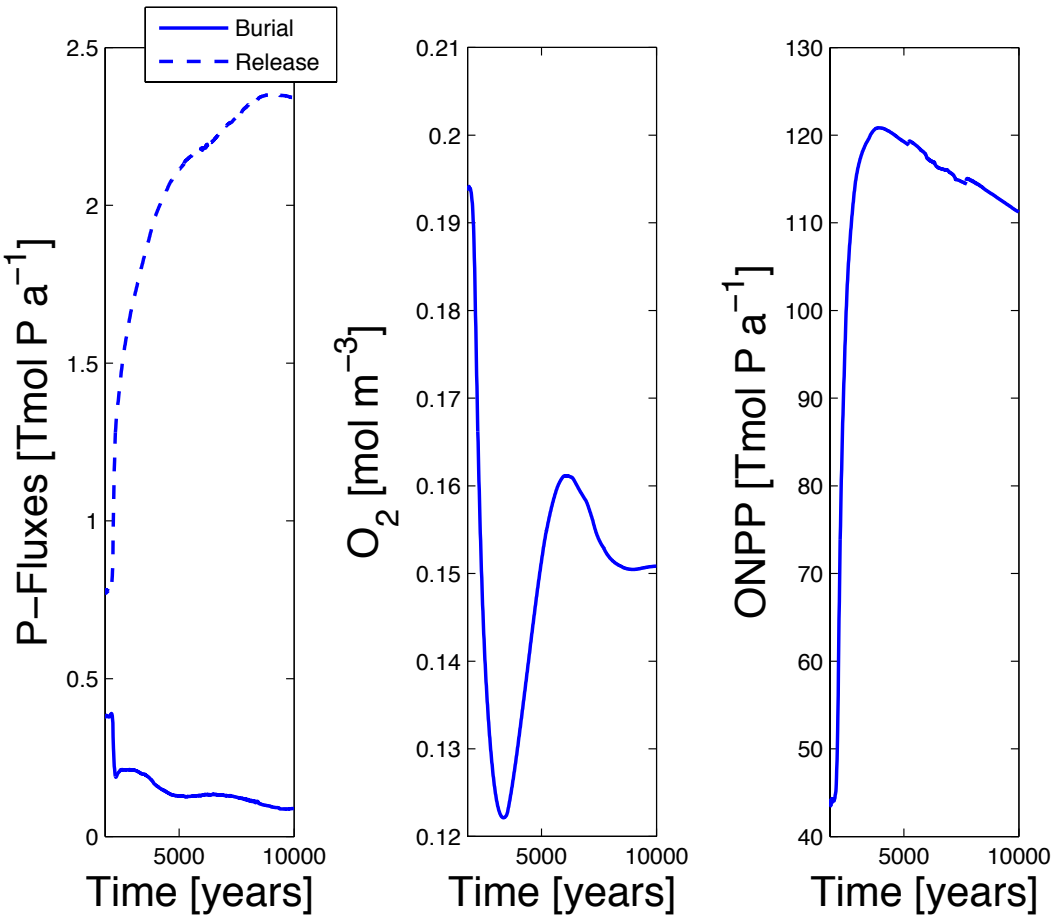

Fig. S4.1: Global mean and annual mean time series of phosphorus burial (blue solid line; left), phosphorus release (blue dashed line; left), oxygen (blue solid line; middle) and ONPP (blue solid line; right) for simulation WB until year 10,000.

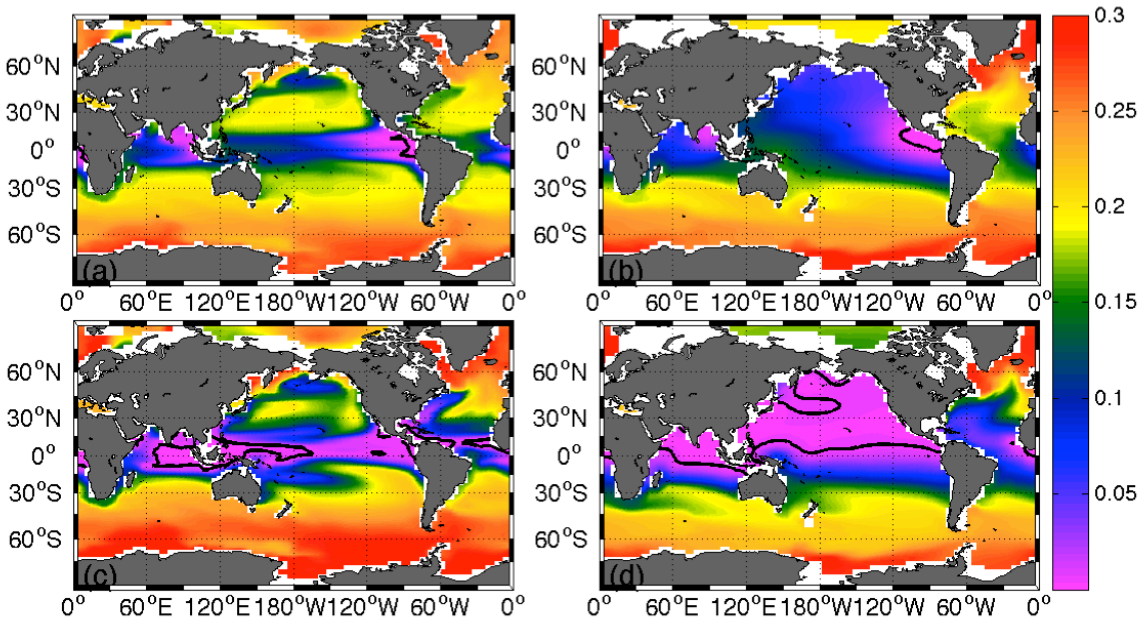

Fig. S4.2: Oxygen concentration in mol O_2 m^{-3} at year 10,000 simulated by the (a) control simulation at 300m depth, (b) and 900m depth, (c) simulation WB at 300m depth and (d) simulation WB at 900 m depth. The black contour lines at 0.005 mol m^{-3} highlight the oxygen minimum zones (OMZs).

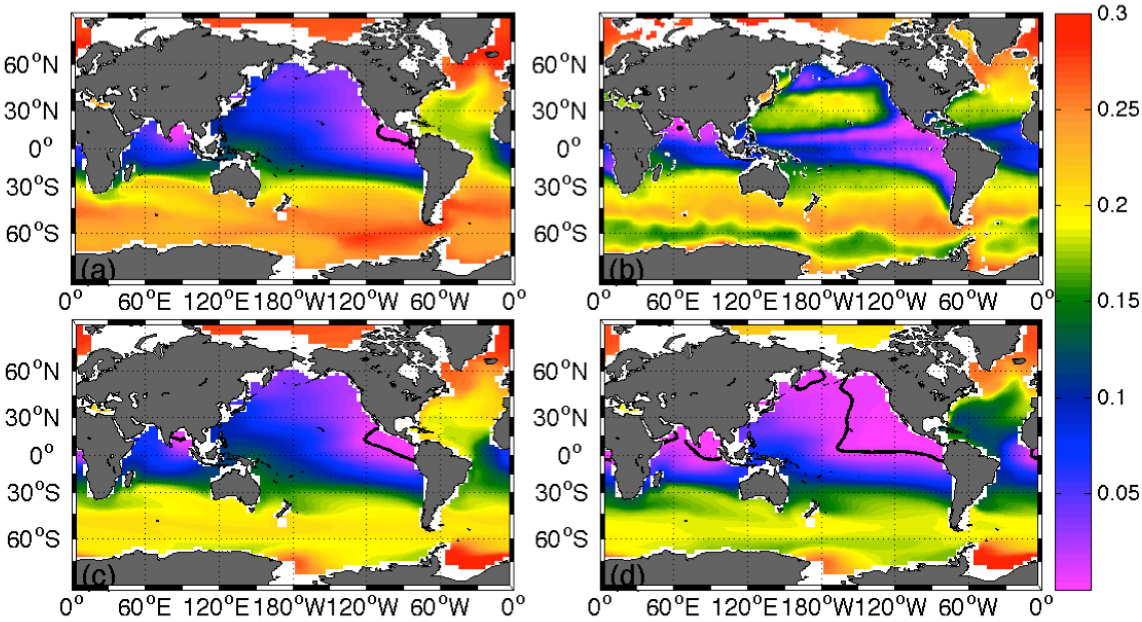

Fig. S4.3: Oxygen concentration in mol O_2 m^{-3} at 900m depth simulated by the (a) control simulation at year 1775 (representative for both REF and WB model runs in year 1775), (b) the World Ocean Atlas in 2009, (c) the control simulation at year 3005 and (d) simulation WB at year 3005. The black contour lines at 0.005 mol m^{-3} highlight the oxygen minimum zones (OMZs).

5. Ocean Phosphorus Inventory and Oceanic Deoxygenation: Large Uncertainties in Future Projections on Millennial Timescales

Tronje P. Kemena[1] • Andreas Oschlies[1] • Klaus Wallmann[1] • Wolfgang Koeve[1] • Angela Landolfi[1] • Andrew Dale[1]

Abstract

Previous studies have shown a strong relation between changes in ocean phosphorus (P) inventory and deoxygenation on millennial timescales. Weathering and benthic fluxes of P act on longer time scales by changing the oceanic P inventory. Under climate warming, weathering supplies additional P to the ocean, which in turn promotes ocean productivity and deoxygenation.

In this study, we investigate uncertainties in projected P inventories and their imprint on the oceanic deoxygenation process using an Earth system model of intermediate complexity for a business-as-usual CO_2 emission scenario.

Model results suggest a large spread in weathering and benthic fluxes of P due to uncertainties in assumptions for weathering parameters, in the representation of slope and shelfs in the model bathymetry, in the parametrization of benthic fluxes and in the representation of sediment P inventories. As a consequence an increase in the oceanic P inventory up to 60% is observed. This leads to large uncertainties in the estimation of suboxic volumes. In year 5000, suboxic volumes range between 1 and 5% of the whole ocean volume. Considerably large amounts of the added P (up to 90%) leave the ocean surface unused as preformed P. Our model simulations show a strong nitrogen limitation on ocean productivity. Nitrogen fixation is not able to counteract the nitrogen loss due to denitrification, in contrast to conclusions from palaeo-reconstructions of large scale deoxygenation events.

We therefore conclude that aforementioned uncertainties should be reduced to achieve more reliable predictions in future projections of oceanic P inventories and deoxygenation on millennial timescales.

Tronje Kemena

e-mail: tkemena@geomar.de

[1] GEOMAR Helmholtz Centre for Ocean Research Kiel, Germany

5.1 Introduction

Ocean phosphorus (P) substantially affects oceanic oxygen concentrations on longer timescales (Tsandev and Slomp, 2009; Palastanga et al., 2011; Monteiro et al., 2012). Phosphorus as ultimate limiting nutrient controls ocean productivity (Tyrrell, 1999). Higher supply of P to the ocean would stimulate export of organic matter and deoxygenation, with possible oxygen depletion in the oxygen minimum zones (OMZs) and along the continental margins (Palastanga et al., 2011). The role of P for the deoxygenation of the modern global ocean has been discussed for a global warming scenario (Niemeyer et al., 2017) and a large number of studies have addressed large-scale deoxygenation in the Cretaceous era, the so-called oceanic anoxic events (OAEs) (Tsandev and Slomp, 2009; Monteiro et al., 2012; Ruvalcaba Baroni et al., 2014).

Several processes are responsible for the large-scale deoxygenation during OAEs in the Cretaceous, which could also play an important role in potential future ocean deoxygenation. In the Cretaceous era, volcanic activity led to enhanced CO_2 outgassing (Jones and Jenkyns, 2001; Kidder and Worsley, 2012) and atmospheric CO_2 concentrations as high as 1000 to 3000 ppmv that have been suggested as a trigger of OAEs (Damsté et al., 2008; Méhay et al., 2009; Bauer et al., 2016). Anthropogenic emissions of CO_2 could, in a business-as-usual scenario, lead to CO_2 concentrations above 1000 ppmv already at the beginning of the 22nd century (Meinshausen et al., 2011). Anthropogenic CO_2 emissions are a short intense pulse over time in comparison to the long-term and relatively constant volcanic CO_2 emissions during OAEs (Kidder and Worsley, 2012), but still these high level of anthropogenic atmospheric CO_2 concentrations could persist for many millennia (Clark et al., 2016) providing conditions for large-scale deoxygenation in the future. During past OAEs a warmer climate led to an enhanced supply of nutrients, in particular P due to increased weathering on land (Blättler et al., 2011; Pogge von Strandmann et al., 2013), which increased the P inventory, productivity and oxygen consumption in the ocean (Monteiro et al., 2012). After the onset of the OAEs, low-oxygen conditions enhanced the recycling of P from the sediments and helped to maintain high levels of productivity in the ocean (Van Cappellen and Ingall 1994; Mort et al. 2007b; Tsandev and Slomp 2009; Kraal et al. 2010).

Kidder and Worsley (2010) found that the Earth had experienced several climate states, like the OAEs, with large-scale anoxia, euxinia and mass extinctions. There is thus some concern that anthropogenic CO_2 emissions and anthropogenic P supply to the ocean could potentially trigger another OAE (Watson et al., 2017). On the other hand Kidder and Worsley (2012) argue that emissions of global fossil fuel reserves are not sufficient enough to cause a modern OAE, but potentially enough to lead to widespread of OMZs.

Nowadays, P acts as ultimate limiting nutrient and controls global ocean productivity whereas N availability limits ocean productivity on a regional scale and on shorter timescales (Tyrrell, 1999). During climate warming, ultimate limitation of ocean productivity could probably switch from P limitation to N limitation (Saltzman, 2005). Nitrogen limitation could for example arise from enhanced denitrification rates in a more anoxic ocean. The spreading of OMZs could enhance denitrification rates and low N to P ratios would probably lead to a stimulation of nitrogen fixation (Kuypers et al., 2004). Nitrogen fixation in close connection with OMZs, however, leads to net N losses due to stoichiometric constraints (Landolfi et al., 2013) which may even overcompensate the effect of N2-fixation on the nitrogen inventory.

Recently, Niemeyer et al. (2017) showed that P weathering and P sediment recycling in a RCP8.5 scenario could strongly enlarge the ocean P inventory and lead to a 4 to 5-fold increase in the suboxic water volume on millennial timescales. Obviously changes in the P inventory have to be taken into account in simulations of long-term deoxygenation of the global ocean.

We hypothesize that the model formulations, which represent weathering and benthic fluxes of P applied in Niemeyer et al. (2017), are still subject to large uncertainties and therefore have to be reexamined. Here we present uncertainty estimates in projected P land-ocean and ocean-sediment fluxes and their impact on the future projection of the oceanic P inventory on millennial timescales. We aim to provide better constraints on future deoxygenation and assess the biogeochemical feedbacks triggered by P addition. In section 5.2 we present the experimental design and the model parameterizations of continental P-weathering and of benthic P release. In section 5.3 we assess uncertainties in P fluxes related to the following aspects:

- Uncertainties in weathering P fluxes due to different assumptions about the preindustrial weathering
- Uncertainties in benthic P fluxes due to different model formulations
- Representation of bathymetry
- Restriction of the reservoir of P in the sediment
- Effect of anthropogenic P fluxes

Consequences for the biogeochemical cycle and deoxygenation are presented in section 5.4. This is followed by the conclusion and discussion in section 5.5.

5.2 Model and Experimental Design

5.2.1 Model

We apply the University of Victoria (UVic) Earth System Model (ESM) version 2.9 (Weaver et al., 2001), which was used in several studies to investigate ocean oxygen dynamics (Schmittner et al., 2007; Oschlies et al., 2008; Getzlaff et al., 2016; Keller et al., 2016; Landolfi et al., 2017). The UVic model consists of a terrestrial model based on TRIFFID and MOSES (Meissner et al., 2003), an atmospheric energy-moisture-balance model (Fanning and Weaver, 1996), a sea-ice model (Bitz and Lipscomb, 1999) and the general ocean circulation model MOM2 (Pacanowski, 1996). Horizontal resolution of all model components is 1.8° latitude x 3.6° longitude. The ocean model has 19 layers with layer thicknesses ranging from 50 m for the surface layer to 500 m in the deep ocean. To represent the marine ecosystem we use an improved NPZD model (Keller et al., 2012). A calcium carbonate sediment model (Archer, 1996) and a parameterization for silicate and carbonate weathering (Meissner et al., 2012) is implemented and used in all simulations. Parameterizations for benthic and weathering fluxes of P, which are used to determine potential future changes in the oceanic P inventory, follow and extend the study of Niemeyer et al. (2017).

5.2.2 Experimental Designs

Twelve different model simulations were performed to explore the range of uncertainties for the long-term development of the oceanic P inventory (Overview in Table 1). Each simulation starts from an Earth system state close to equilibrium under preindustrial atmospheric CO_2 concentrations. To reach the equilibrium, individual spin-up runs were carried out with simulations length of 20.000 years or longer. During the spin-up, oceanic P inventories are conserved. In the spin-up runs for simulations with different P burial parametrizations (purple and red in Table 1), oceanic P loss is compensated by weathering fluxes of P. For model simulations without benthic fluxes of P (black, green and blue in Table 1), one common spin-up run was performed.

At the beginning of the simulations, we assume that the oceanic P cycle is in equilibrium. All simulations start in year 1775 and end in year 5000. The simulations are forced with anthropogenic CO_2 emissions according to the extended RCP 8.5 scenario until year 2300 (Meinshausen et al., 2011), followed by a linear decline to zero CO_2 emissions in year 3000. Anthropogenic emissions of non-CO_2 greenhouse gases and any greenhouse gas emissions from land-use change are not considered in the simulations.

The reference simulation (*Ref*) is performed without weathering and burial fluxes of P, so that the P inventory of the ocean remains unchanged. The remaining simulations

apply weathering and/or burial fluxes to the ocean. Weathering, anthropogenic and benthic P fluxes are modelled individually. The overview over all model configurations can be found in Table 1.

Simulations	Abbreviation	Fluxes	P Burial parametrization
Reference (constant P inv.)	Ref	No	No burial
Anthropogenic P input	Anthr	Flux from Filippelli (2008)	No burial
Weathering	Weath0.05	$W_{P,0}$=0.05; $W_{P,const}$=0; SED_P=0	No burial
Weathering	Weath0.10	$W_{P,0}$=0.10; $W_{P,const}$=0; SED_P=0	No burial
Weathering	Weath0.15	$W_{P,0}$=0.15; $W_{P,const}$=0; SED_P=0	No burial
Weathering	Weath0.38	$W_{P,0}$=0.38; $W_{P,const}$=0; SED_P=0	No burial
Burial Reference	Bur	SED_P(t=1775a)=0.38 $W_{P,0}$=0; $W_{P,const}$=0.38	C:P reg. ratio (Wallmann, 2010), C Burial (Flögel et al., 2011)
Burial Dunne	Bur_Dun	SED_P(t=1775a)=0.25 $W_{P,0}$=0; $W_{P,const}$=0.25	C:P reg. ratio (Wallmann, 2010), C Burial (Dunne et al., 2007)
Low burial estimate	Bur_low	SED_P(t=1775a)=0.21 $W_{P,0}$=0; $W_{P,const}$=0.21	Bur configuration, but with Y_F=100.5; A=90; r=38 in (3)
High burial estimate	Bur_high	SED_P(t=1775a)=0.60 $W_{P,0}$=0; $W_{P,const}$=0.60	Bur configuration, but with Y_F=167; A=108.5; r=29.5 in (3)
Burial with restricted Reservoir	Bur_res	SED_P(t=1775a)=0.41 $W_{P,0}$=0; $W_{P,const}$=0.41	Bur configuration, but with 113 µmolP cm^{-2} Reservoir
Burial without Subgrid Bathymetry	Bur_noSG	SED_P(t=1775a)=0.09 $W_{P,0}$=0; $W_{P,const}$=0.09	Bur configuration, but without Subgrid Bathymetry

Table 1: Overview of all conducted simulations. P inventory uncertainties are assessed by evaluating different P flux parameterizations, parameterization coefficient uncertainties, anthropogenic fluxes, effects of bathymetry and by constraining the benthic P reservoir. P fluxes are given in TmolP/yr. In the P weathering simulations only weathering anomalies were applied. In the P burial simulations a constant P weathering flux ($W_{P,0}$) balances P burial ($B_{P,0}$) during the spin up simulations. Size of the preindustrial P inventory is for all simulations the same. More detailed information can be found in the text.

Burial fluxes of P are applied in the simulations *Bur, Bur_noSG, Bur_Dun, Bur_low, Bur_high* and *Bur_res*. Uncertainties in benthic P fluxes are examined by modifying the *Bur* model configuration. In the following we describe how P burial is simulated in the *Bur* model configuration and then the differences between the model configurations *Bur_noSG, Bur_Dun, Bur_low, Bur_high* and *Bur_res* are explained.

Our model does not contain a prognostic sediment model, instead the ocean to sediment fluxes of P (SED_P) are determined in every grid box from the difference between the simulated organic P flux to the sediment (RR_{POP}) and the sedimentary release of P from the sediment (BEN_{DIP}):

$$SED_P = RR_{POP} - BEN_{DIP}. \quad (5.1)$$

RR_{POP} is interfered from the simulated detritus flux from the ocean to the sediment for fixed Redfield ratio (C:N:P, 106:16:1) and BEN_{DIP} is calculated locally by "transfer functions", which parameterize sediment/water exchange of P as a function of the rain rate of organic matter and the bottom-water oxygen concentration. A weaker P retention is observed in sediments overlain by oxygen depleted bottom waters (Ingall and Jahnke, 1994). We model the release of P (BEN_{DIP}) from the sediment in dependence on C release (BEN_{DIC}) via the C/P regeneration ratio r_{reg} (Wallmann et al., 2010):

$$BEN_{DIP} = \frac{BEN_{DIC}}{r_{reg}}. \quad (5.2)$$

BEN_{DIC} is the benthic carbon flux from organic matter degradation in the sediment to the overlaying ocean. In our model, this flux is determined just virtually and no burial of organic carbon is applied instead all carbon is remineralized in the deepest ocean layer (BEN_{DIC} is needed to calculate BEN_{DIP} in Eq. 5.2). The virtual burial of organic carbon (BUR_C) is given in dependence on the simulated organic C flux from the ocean to the sediment (RR_{POC}) and on sediment depth as described in (Flögel et al., 2011). Burial of organic C is more effective in sediments at the continental margin (Eq. 5.3a) than for the deep sea (Eq. 5.3b, sediment below 1000m water depth):

$$BUR_C = 0.14 \cdot RR_{POC}^{1.11}, \quad (5.3a)$$

$$BUR_C = 0.014 \cdot RR_{POC}^{1.05}. \quad (5.3b)$$

r_{reg} depends on oxygen and under high-oxygen conditions r_{reg} is close to the Redfield ratio 106. Under low-oxygen conditions, r_{reg} is lower than 106, which leads to a preferential P release from organic matter and, eventually, a net release of P from the sediment ($BEN_{DIP} > RR_{POP}$, in Eq. 5.5.1) (Wallmann et al., 2010):

$$r_{reg} = Y_F - A \cdot \exp(-O_2/r). \quad (5.4)$$

In *Bur* the coefficients Y_F=123±24; A=112±24; r=32±19 (Wallmann, 2010) are used for r_{reg} and equations from Flögel et al. (2011) for BEN_{DIC}.

The UVic model has a coarse standard model bathymetry with a horizontal resolution of 1.8° latitude x 3.6° longitude. This causes shelfs and slopes not to be well represented. In our experiments, however, sinking organic matter interacts with the sediment on a detailed sub-grid bathymetry, as described in the following.

The sub-grid bathymetry is inferred from ETOPO2v2[4] (National Geophysical Data Center, 2006). Fractional cover of sea floor by sediments is calculated at every depth level of the UVic model. Sinking organic matter is partially intercepted at the bottom of

[4] https://www.ngdc.noaa.gov/mgg/global/etopo2.html

each grid box by a sediment layer and the intercepted amount depends linearly on the fractional coverage of the seafloor. Sinking organic matter contains P, C and N in Redfield ratios (1:106:16). At the seafloor, P is remineralized in accordance to Eq. (5.1) and Eq. (5.2) as BEN_{DIP}, whereby C and N are completely remineralized under oxygen utilization without any burial. This leads to a better vertical representation of benthic fluxes of P and simulated sediment to ocean fluxes of detritus (see section 5.3.2). The sub-grid bathymetry does not affect other processes like circulation, advection or mixing processes.

Deviations from the *Bur* model configuration for the simulations *Bur, Bur_noSG, Bur_Dun, Bur_low, Bur_high* and *Bur_res* are described in the following.

For the simulation *Bur_noSG*, P fluxes at the sediment-ocean interface are calculated with the coarser standard model bathymetry (*noSG* for no Sub-Gridscale parameterization), which barely reproduce the global coverage of shelf areas.

In the *Bur_Dun* simulation BEN_{DIC} is calculated with the equation from Dunne et al. (2007):

$$BUR_C = RR_{POC} \cdot \left[0.013 + \frac{0.53 \cdot RR_{POC}^2}{(7 + RR_{POC})^2}\right]. \quad (5.5)$$

This equation leads to high (low) C burial rates for high (low) C rain rates. In contrast to Flögel et al. (2011), here the burial efficiency of C depends on water depth and it is a magnitude larger for slope and shelf regions (Eq. 5.3). These two formulations are affected differently by changes in ocean productivity, which further contributes to uncertainties in model projections.

In the *Bur_low* and *Bur_high* simulation we examine uncertainties in parameters of Eq. (5.4) and their influence on P burial fluxes. 100.000 independent coefficient combinations are picked from their Gaussian distributions to calculate a range of global P burial estimate. Coefficient and their uncertainties (Y_F=123±24; A=112±24; r=32±19) are derived from a curve fit to observations in Wallmann (2010). Global P burial varies between 0.21 TmolP yr^{-1} (*Bur_low*) and 0.60 TmolP yr^{-1} (*Bur_high)* for a confidence interval of 90% (coefficients are shown in Table 1). The P burial is calculated offline from the preindustrial virtual simulated detritus flux to the sediment (with fixed Redfield ratio: C:N:P, 106:16:1) and the preindustrial oxygen field above the model sea floor used in the *Bur* simulation. Only minor differences between the oxygen field of the *Bur* simulation and the oxygen field of *Bur_low* and *Bur_high* simulations appear, which lead to negligible errors in the offline calculation of the preindustrial global P burial.

The release of P can exceed the supply of organic P to the sediment. The implemented transfer functions (Eq. 5.2 and 5.4) imply unlimited reservoirs of sediment P at the continental shelf similar to Flögel et al. (2011). In the simulation *Bur_res* restrictions are applied to ocean-sediment P release by adding simple P inventories for ocean grid

boxes with a sediment. Ocean-sediment fluxes are integrated over time and a maximum inventory of 113 µmol P cm^{-2} can be accumulated, based on the following assumptions: The top 10 cm of the sediment column are mixed by organisms and are hence regarded as the active surface layer that is in contact with the overlying bottom water. Considering a mean porosity of 0.8 and a mean density of dry particles of 2.5 g cm^{-3}, the mass of solids in this layer is 5 g cm^{-2} (Burwicz et al., 2011). The mean concentration of total P in continental shelf and slope sediments is 0.07 wt-% = 22.6 µmol/g (Baturin, 2007). Together, these assumptions convert to an average inventory of total solid P in the active surface layer of 113 µmol cm^{-2}. We assume that shelf and slope sediments can release up to 100 % of this total inventory under low oxygen conditions. It is more likely that less P can be released from the sediment. For example under low oxygen conditions, reactive P is transformed into authigenic P (Filippelli, 2001), which is more difficult to dissolve.

In the following the *Bur, Bur_noSG, Bur_Dun, Bur_low, Bur_high* and *Bur_res* are described in the following.

Uncertainties in the ocean P inventory by weathering processes and anthropogenic fluxes of P are examined with the model simulations *Anthr, Weath0.05*, *Weath0.10*, *Weath0.15* and *Weath0.38*. The individual model configuration is described in the following.

Global P-fluxes from weathering and anthropogenic sources are distributed over all river basins, locally weighted by river discharge rates. Anthropogenic P fluxes from fertilization, soil loss due to deforestation and sewage (Filippelli, 2008) are applied in the *Anthr* simulation. In the *Weath0.05*, *Weath0.10*, *Weath0.15*, *Weath0.38* simulation anomalies due to weathering fluxes (W_P) are implemented as described in Eq. (5.6).

$$W_P = W_{P,0} \cdot (f(NPP, SAT) - 1) + W_{P,const} \quad (5.6)$$

In the simulations *Weath0.05*, *Weath0.10*, *Weath0.15*, *Weath0.38*, the weathering flux W_P is applied as an anomaly (parameter values see Table 1) with constant $W_{P,0}$ the preindustrial P flux. No benthic P fluxes are applied and for preindustrial conditions W_P equals 0 TmolP a^{-1}. The dynamic weathering function *f* is adopted from Niemeyer et al. (2017) and is originally based on the equations from Lenton and Britton (2006):

$$f = 0.25 + 0.75 \cdot (NPP/NPP_0) \cdot \left(1 + 0.087(SAT - SAT_0)\right). \quad (7)$$

The equation depends on globally averaged surface air temperature (SAT) and net primary production (NPP) on land. The index 0 indicates preindustrial values. Increasing SAT and NPP lead to an enhanced weathering.

The upper estimate of $W_{P,0}$ in *Weath0.38* is interfered from the burial reference simulation *Bur*. In the simulation, $W_{P,0}$ is the weathering fluxes that is needed to compensate for loss of P due to burial. With the simulations *Weath0.05*, *Weath0.10*,

Weath0.15 we cover the range of $W_{P,0}$ derived from observational studies ranging from 0.05 to 0.30 TmolP/yr (see Fig. 5.1, Benitez-Nelson, 2000; Compton et al., 2000; Ruttenberg, 2003).

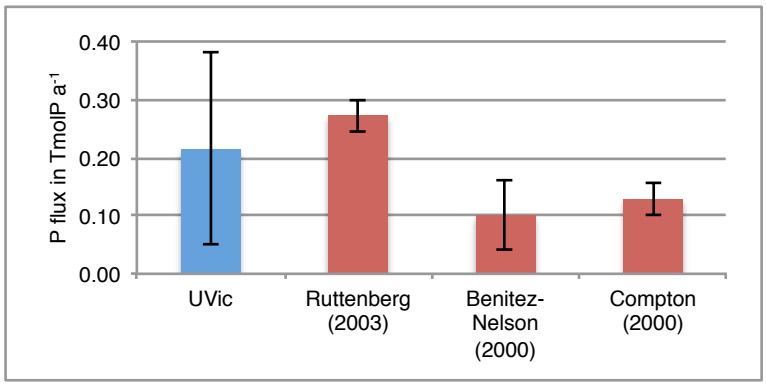

Fig. 5.1: Globally integrated preindustrial P fluxes in TmolP a^{-1} from observations (red) and applied in the UVic model (blue). Error bars for the UVic model (blue) denote the range of P fluxes $W_{P,a}$ that are applied in simulations (see Table 1). The P fluxes from observations (red) are estimated global riverine fluxes of reactive P and the error bars denote upper and lower estimates (Benitez-Nelson, 2000; Compton et al., 2000; Ruttenberg, 2003).

Uncertainties due to different weathering parameterizations are not investigated in this study, but the parameterization used here is not to be considered as a outlier in comparison to other weathering parameterizations (Fig. 6a in Meissner et al., 2012). In Meissner et al. (2012), the parameterization was used as a weathering parameterization for carbonate and silicate weathering and in Niemeyer et al. (2017) applied to calculate weathering fluxes of P.

5.3 Uncertainties in Phosphorus Inventory

In the performed model simulations, the large range of potential phosphorus (P) fluxes to the ocean (Fig. 5.2a) leads consequentially to uncertainties in future P inventories for climate warming (Fig. 5.2b). All simulations undergo a similar climate development with negligible small differences in atmospheric carbon dioxide (CO_2) concentrations. Maximum CO_2 concentrations of 2200 ppmv are reached in year 2250 and then CO_2 concentrations decline to 1100 ppmv until year 5000, comparable to results from Clark et al. (2016). We find that the large spread in P fluxes is not related to differences in the climate or atmospheric carbon dioxide forcings, but rather to the differences in parametrizations of P land-ocean (section 5.3.1) and sediment-ocean (section 5.3.2) fluxes.

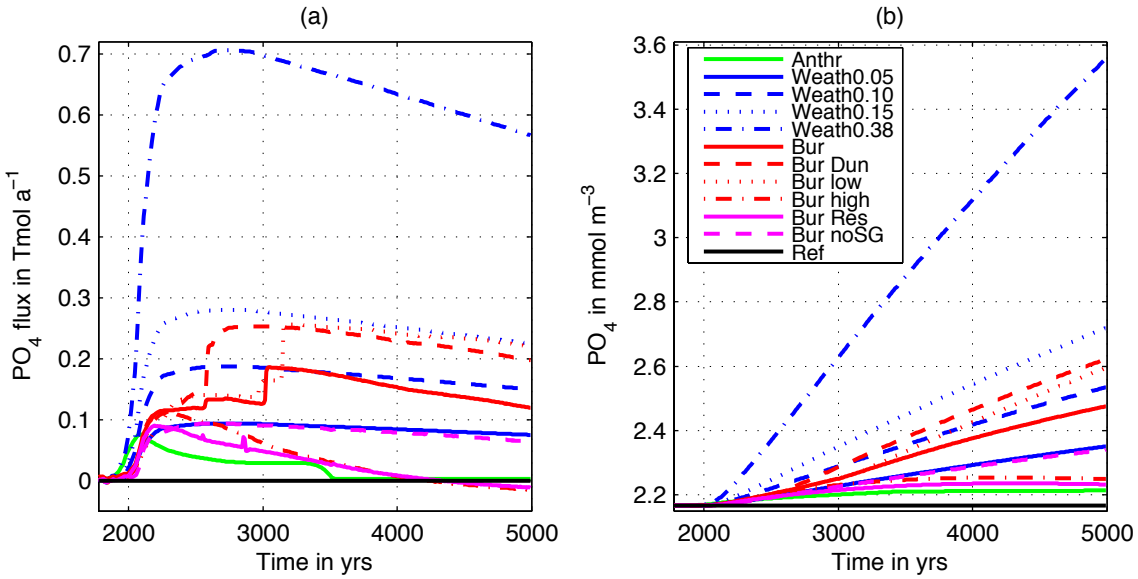

Fig. 5.2: Globally (a) integrated flux of PO_4 in Tmol a^{-1} and (b) averaged phosphate concentration in mmol m^{-3}. Simulation descriptions can be found in Table 1.

5.3.1 Land Fluxes: Weathering and Anthropogenic

Largest uncertainties in the P inventory appear from the large spread in the P-weathering fluxes (Fig. 5.2). Upper and lower estimates of P-weathering fluxes vary by a factor of 6 (Fig. 5.2a, blue lines). Weathering anomalies depend in our weathering simulations linearly on the estimate for the preindustrial weathering flux $W_{P,0}$ (see Eq. 5.6), because the climate development is equal among the simulations. Therefore, the uncertainty of $W_{P,0}$ (Fig. 5.1a) impacts future land-ocean P-fluxes significantly.

In this study weathering fluxes increase from the pre-industrial value by a factor of 2.5 until year 5000 for atmospheric CO_2 concentrations of 1100 ppmv. This compares well with the two to four times increase in weathering fluxes estimated for the OAE 2 approximately 91 Ma ago (Pogge von Strandmann et al., 2013) when atmospheric carbon dioxide concentrations increased order of 1000 ppmv (Damsté et al., 2008).

In contrast to weathering-induced P input, anthropogenic P fluxes (Filippelli, 2008) influence the P inventory only in the near future (Fig. 5.2a, green line). After year 2100 a decline in anthropogenic P fluxes is expected, because of the depletion of the easily reachable phosphorite mining reserves (Filippelli, 2008).

5.3.2 Sediment Fluxes: Parameterizations, Sub-grid Bathymetry, Sediment Reservoir

Release of P from the sediment are well connected to the redox state and thus with the oxygen state of ocean water above the sediments (Wallmann 2003; Flögel et al. 2011). Climate warming reduces the solubility of oxygen in the ocean and the continuous warming reduces ventilation and increases utilization of nutrients in the ocean (more

details in section 5.4). Distinct jumps in benthic fluxes of P appear, when conditions change from an oxic to a suboxic environment in individual regions. The feedback between sedimentary P release and productivity could then sustain and possibly extend such suboxic regimes.

Therefore, the general decrease in ocean oxygen could drive preferential release of P from the sediment. Differences in sediment P fluxes are related to uncertainties in the parameterization of the transfer function (Fig. 5.2, red lines), to different representations of the bathymetry (Fig. 5.2, purple dashed line) and to the way sediment P reservoirs in the sediment are represented (Fig. 5.2, purple solid line).

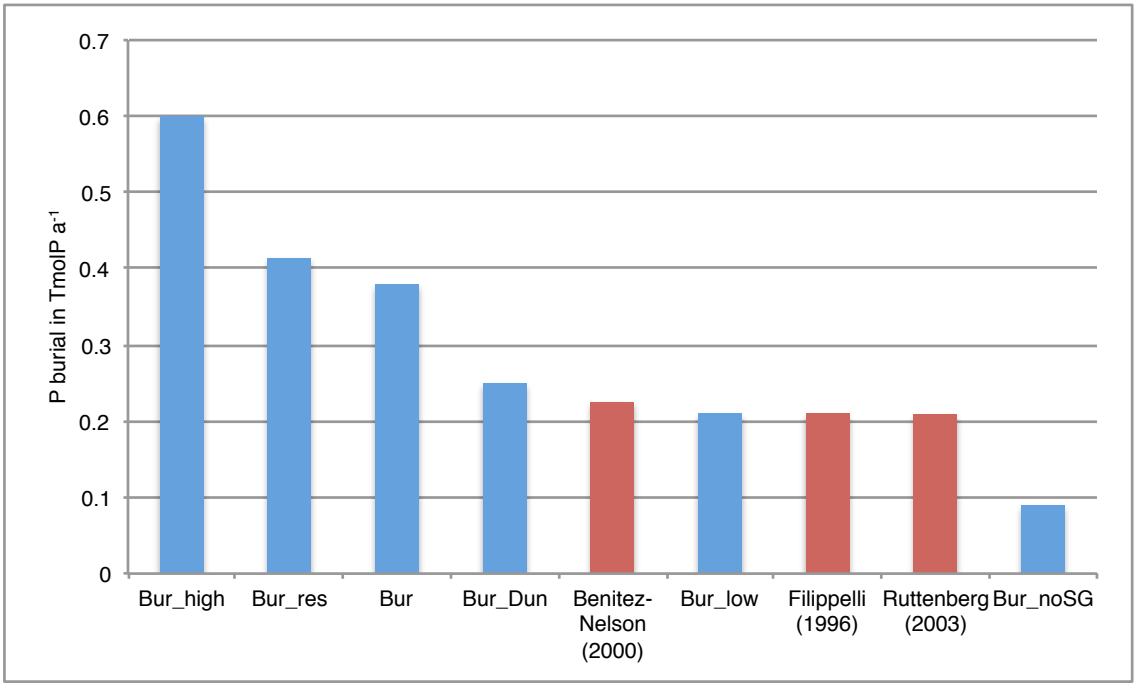

Fig. 5.3: Globally integrated preindustrial P-burial fluxes in TmolP a^{-1} from observations (red) (Filippelli and Delaney, 1996; Benitez-Nelson, 2000; Ruttenberg, 2003) and for UVic model simulations (blue). Description of the model simulations can be found in Table 1.

The different observational estimates of global burial amount approximately to 0.2 TmolP a^{-1} (Fig. 5.3) (Filippelli and Delaney, 1996; Benitez-Nelson, 2000; Ruttenberg, 2003), which are relatively well reproduced by simulations *Bur_low* and *Bur_Dun*. The simulation with the standard UVic-model bathymetry (*Bur_noSG*) underestimate P burial by 50% while the simulations *Bur_high*, *Bur* and *Bur_res* overestimate P burial by up to 300%. The transient response of the P release is stronger for simulations with a weak burial and vice versa (Fig. 5.2), except for simulation *Bur_res*. In *Bur_res* a significant reduction in the transient P release appears due to the implementation of a finite P reservoir. Net global P loss due to enhanced burial of P occurs in *Bur_res* at the end of the simulation. In year 5000 global P concentrations increased in *Bur_res* by just 0.06 mmolP m^{-3}, which is much smaller than the increase by 0.36 mmolP m^{-3} in simulation *Bur* with an assumed unlimited P reservoir. This small increase in the respective ocean P inventory can be explained by the reduction in P sediment inventory

rather than by changes in the rain rate of particulate organic matter to the sediment. Rain rate of particulate organic matter is represented in the UVic model by detritus that reaches the bottom of the ocean and is calculated in terms of carbon as rain rate of organic carbon (RRPOC) and is compared to observations (Table 2).

		Bohlen (2012)			*UVic model with sub-grid bath.*			*UVic model without sub-grid bath.*		
Area	*Depth range*	*RRPOC [TgC a^{-1}]*	*RRPOC [%]*	*Area [%]*	*RRPOC [TgC a^{-1}]*	*RRPOC [%]*	*Area [%]*	*RRPOC [TgC a^{-1}]*	*RRPOC [%]*	*Area [%]*
Shelf	*0-200m*	*1056*	*60*	*6*	*1039*	*70*	*6.5*	*179*	*28*	*2.3*
Slope	*200-2000m*	*393*	*22*	*10*	*205*	*14*	*11.7*	*219*	*34*	*13.3*
Deep sea	*>2000m*	*312*	*18*	*84*	*235*	*16*	*81.9*	*238*	*37*	*84.6*
Sum		*1761*			*1479*			*637*		

Table 2: Rain rate of particulate organic carbon (RRPOC) to the seafloor for the shelf, slope and deep-sea areas from Bohlen et al. (2012) and for UVic model simulations with and without sub-grid bathymetry.

A realistic model bathymetry improves simulated RRPOC in comparison to Bohlen et al. (2012) (shown in terms of carbon in Table 2), which affects global sedimentary P release and the vertical distribution of the P release. The estimates from Bohlen et al. (2012) are well in the range of uncertainties of observation based estimates (Fig. 5.4) (Muller-Karger et al., 2005; Burdige, 2007; Dunne et al., 2007; Bohlen et al., 2012). We use a sub-grid bathymetry in the UVic model. This significantly improves modelled RRPOC at the shelf compared to observations, but with less influence in the deep ocean and at the slope (Table 2). RRPOC increases significantly from 179 TgC a^{-1} without sub-grid to 1039 TgC a^{-1} with sub-grid bathymetry, the latter is comparable to estimates from Bohlen et al. (2012). Global RRPOC over all 3-depth regimes increases from 900 TgC a^{-1} without sub-grid to 1500 TgC a^{-1} with sub-grid bathymetry. This well represents RRPOC in data studies, which suggest that global RRPOC to the sediment could range from 900 to 2300 TgC a^{-1} (Fig. 5.4).

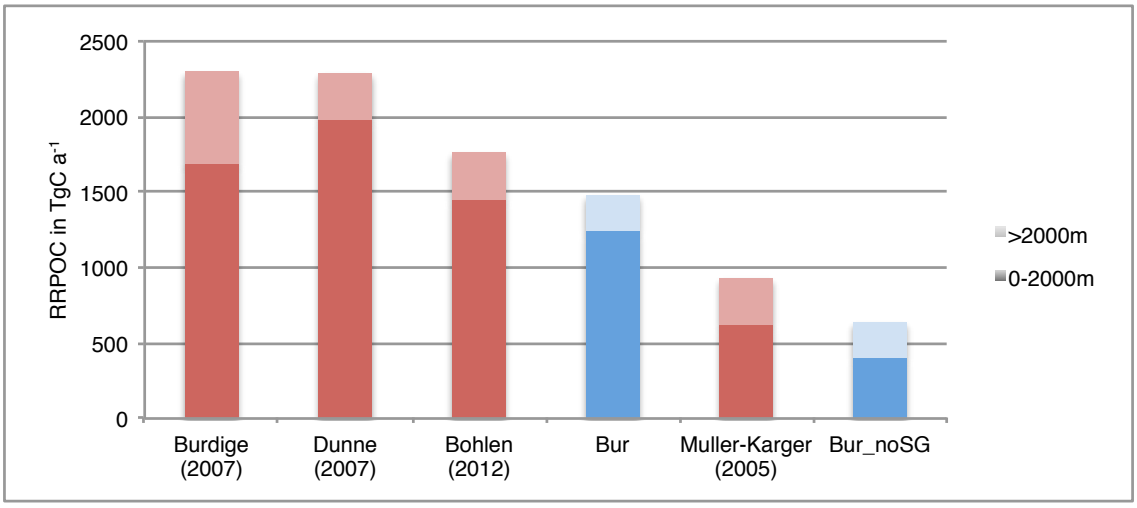

Fig. 5.4: Globally integrated preindustrial rain rate of particulate organic carbon (RRPOC) to the seafloor in TmolP a^{-1} from different studies (red) (Muller-Karger et al., 2005; Burdige, 2007; Dunne et al., 2007; Bohlen et al., 2012) and for UVic model simulations (blue) between 0 to 2000m water depth (darker) and below 2000m (brighter). In the UVic model organic carbon is completely remineralized at the seafloor. The simulation Bur is representative for all remaining UVic model simulations except Bur_noSG.

In summary, a sub-grid bathymetry leads to a substantial improvement of the representation of RRPOC to the sediment in the UVic model, more realistic benthic fluxes of P could be also attained by adjusting parameters for r_{reg} (Eq. 5.4) or by using the function of Dunne et al. (2007) to calculate BEN_{DIC} (Eq. 5.5). The implementation of a P reservoir in the sediment has a substantial impact on the transient development of the global P inventory on millennial time scale.

5.4 Oceanic Deoxygenation

Climate change influences deoxygenation in the global ocean by changes in circulation, ocean temperature and remineralisation of organic matter. Global warming leads to a stronger stratification and therefore less ventilation of the deeper layers. With a warmer ocean the solubility of O_2 decreases. Finally, the export of organic matter affects remineralisation processes in the deep ocean and therefore the suboxia (Fig. 5.5, black line). In the following we analyze how differences in ocean P inventories affect suboxia (Fig. 5.5). For a more clear comparison, the *Ref* simulation is compared here (and in the following sections) to simulation *Weath0.38* instead of to all simulations.

In the *Ref* simulation, global suboxic volume increases during climate change from 0.3 to 1% until year 5000 and the suboxic sediment area increases from 0.06 to 0.23% (Fig. 5.5, black line). The increase in the *Weath0.38* simulation is 5 (8) times higher for the suboxic volume (suboxic sediment area). The expansion of suboxic sediment areas is also enhanced for simulation with benthic fluxes, which could be related to regional feedbacks between marine productivity, oxygen and P as it was suggested in Wallmann et al. (2010). However, simulation *Bur_res* with restrictions in the P reservoir do not show such an enhanced spreading of suboxic areas.

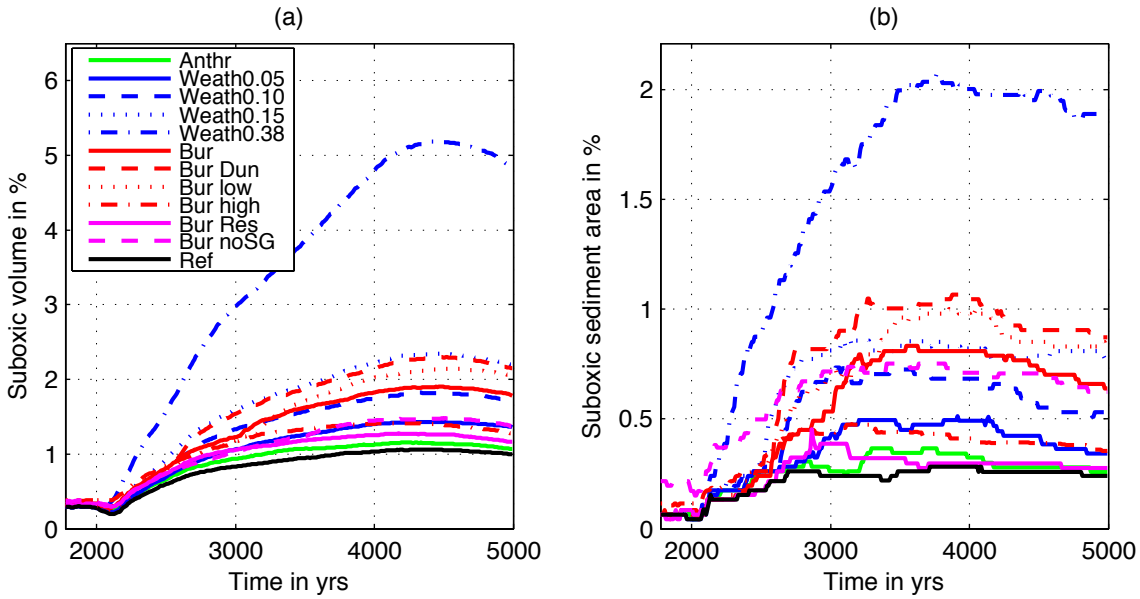

Fig. 5.5: Globally integrated (a) suboxic volume in percentage of total ocean volume and (b) suboxic sediment surface area in percentage of total sediment surface area. Water is designated as suboxic for oxygen concentrations below 0.005 molO_2 m^{-3}. Simulation descriptions can be found in Table 1.

In the following sections, we show how the expansion of suboxia is related to net primary production (NPP) and export of organic matter (section 5.4.1); to nitrogen limitation (section 5.4.2). Finally we show how the relevance of the different deoxygenation processes varies over time and compare therefore anomalies in the oxygen inventories (section 5.4.3). The latter approach gives another perspective by presenting anomalies of oxygen inventories instead of the extend of suboxia, which are consequence of more local processes.

5.4.1 Enhanced Biological Pump

The biological pump can be described by the supply from biological sequestered carbon to the deep ocean. In the euphotic zone phytoplankton and diazotrophs take up CO_2 in the UVic model (Fig. 5.6a). Once they die, they sink as detritus downward out of the euphotic zone (Fig. 5.6b), where the detritus is respired under the utilization of oxygen. And simultaneously organic P, C, N is remineralized and stored in dissolved form in the deep ocean. The remineralization process of detritus occurs in the UVic model in fixed Redfield ratios directly related to the utilization of oxygen until oxygen is depleted. P supply could stimulate the biological pump and could explain deoxygenation trends in the simulations. On the other hand, differences in the circulation could affect the ventilation of the deep ocean. However, no significant differences in climate and circulation appear among the simulations and therefore the ventilation affects all simulations in the same way. Net primary production (NPP) and export of organic matter out of the euphothic zone and their impact on the biological pump are discussed in the following.

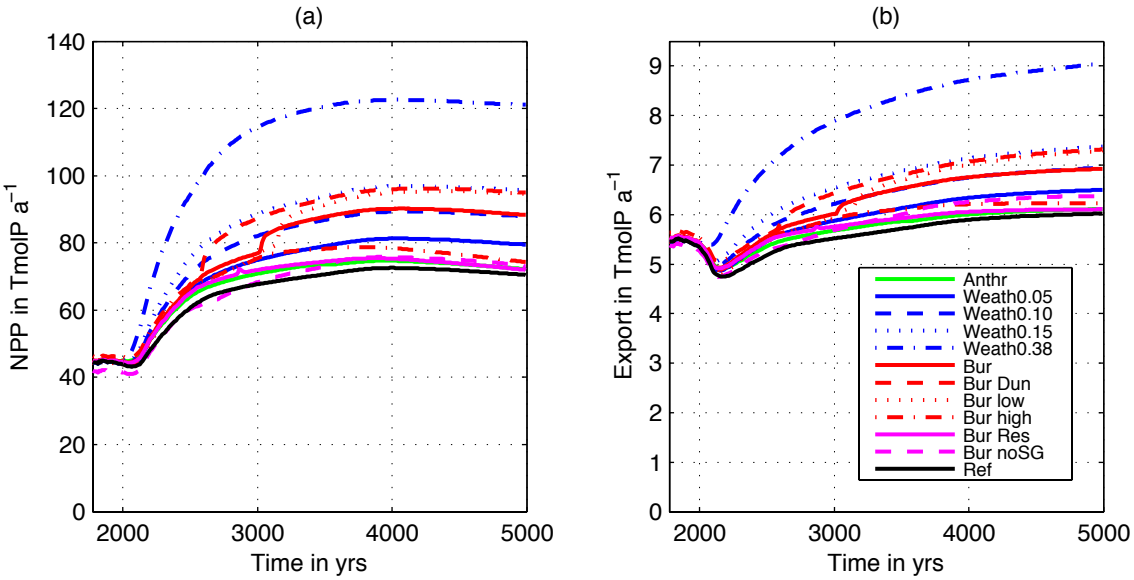

Fig. 5.6: Globally integrated (a) ocean net primary production (NPP) in TmolP a^{-1} and (b) export of organic matter below the 130m depth level in TmolP a^{-1} suboxic volume in percentage of total ocean volume. Simulation descriptions can be found in Table 1.

In the *Ref* simulation, net primary production (NPP, Fig. 5.6a black line) increases from 45 to 70 TmolP a^{-1} until the end of the simulation. In *Weath0.38*, enhanced P supply to the ocean lead to 3 times stronger NPP increase than in the *Ref* simulation. The P Inventory increases continuously, but the NPP do not follow this trend and instead it stagnates already in year 4000. In year 5000, NPP increases by 3.6 TmolP a^{-1} per 0.1 mmolP m^{-3} rise in the P inventory. The remaining simulations show a much stronger response with 5.4 TmolP a^{-1} per 0.1 mmolP m^{-3} increase (linear regression with R^2= 0.9624). A negative feedback seems to inhibit NPP more intensely in simulations with large oceanic P inventories. The different pathways of the new P to the surface, the release from sediments in contrast to the weathered P delivered by rivers, hereby did not affect the NPP sensitivity to the P inventory. The efficiency of the biological pump may be described by the export to NPP ratio, which has a preindustrial ratio in the UVic model of about 0.12. This ratio reduces in average among all simulations to 0.08 by year 5000 without considerable exceptions. However, we notice here that the positive feedback between P and deoxygenation in the deep is limited in our simulations by negative feedbacks. We investigate in the following the role of nitrate to limit NPP.

5.4.2 Nitrogen Limitation

At the beginning of the UVic simulations denitrification as sink of nitrate and nitrogen fixation by diazotrophs balance each other. In the *Ref* simulation climate warming enlarge the oxygen minimum zones, which enhances denitrification in the tropics (not shown). Nitrogen fixation by diazotrophs (Fig. 5.7a) is not able to balance the loss by denitrification. As a consequence nitrate decreases globally by 4 mmolN m^{-3} until year 5000 (Fig. 5.7b). In the model, diazotrophs have an advance over phytoplankton in low-N and high-P environments. In the simulation with P supply, nitrogen fixation by

diazotrophs is stimulated (Fig. 5.7a) and partly counteracts the nitrate loss by denitrification. The loss in nitrate is not completely compensated by nitrogen fixation, which leads to a decrease in globally averaged N to P ratios. In the *Ref* simulation N:P decreases from 14 to 12 and for the *Weath0.38* simulation it decreases to 8. The nitrogen cycle is not able to recover from the N:P ratio drop with respect to pre-industrial ratios. In the model, we assume that phytoplankton biomass is growing with fixed Redfield stoichiometry. The ability of marine organisms to respond to changing N:P ratios is not modelled. Marine organisms could probably utilize the excess in P, if they would be able to adapt their stoichiometry to the decreasing N:P ratios.

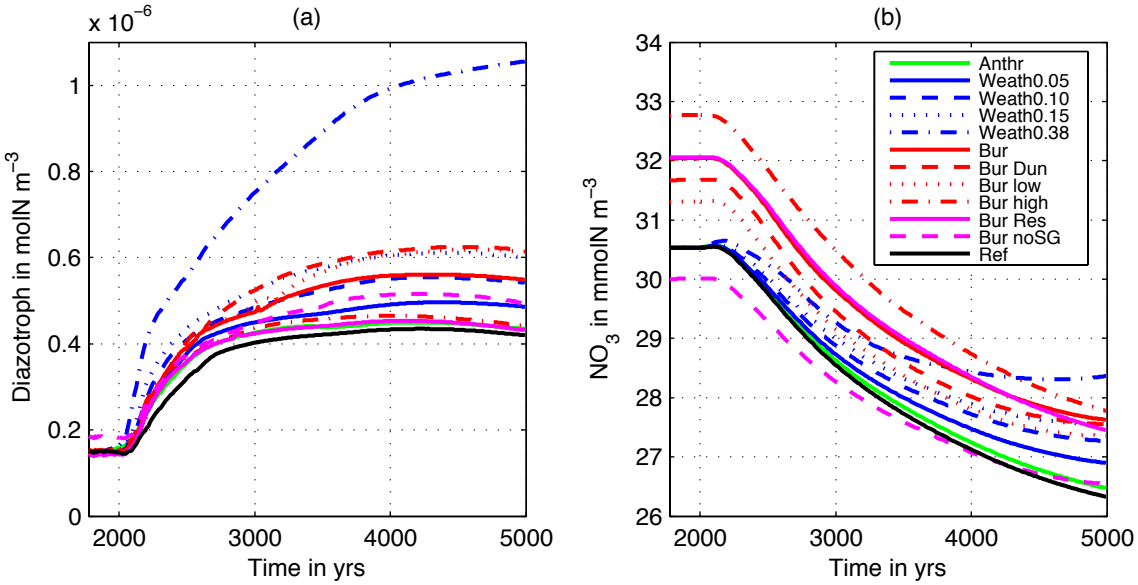

Fig. 5.7: Globally averaged (a) diazotroph concentration in molN m^{-3} and (b) nitrate (NO_3) concentration in mmolN m^{-3}. Simulation descriptions can be found in Table 1.

5.4.3 Temporal Variations of Deoxygenation Processes

Anomalies in circulation, ocean temperature and remineralisation of organic matter affect ocean oxygen in a climate-warming scenario. In the *Ref* simulation, the oxygen inventory (Fig. 5.8a) decreases by 60 Pmol O_2 in year 3000 and then recovers until year 5000. Added P enhances the deoxygenation in the ocean and leads to an enhanced decrease in O_2 than in the *Ref* simulation by 90 Pmol O_2 in year 3300 and still shows a negative anomaly of 50 Pmol O_2 in year 5000. Global anomalies in O_2 are due to changes of the Apparent Oxygen Utilization (AOU, Fig. 5.8b) and the oxygen saturation level (Fig. 5.8c). Changes in oxygen saturation level are similar among the model simulations and they follow ocean surface temperatures delayed by the ocean inertia.

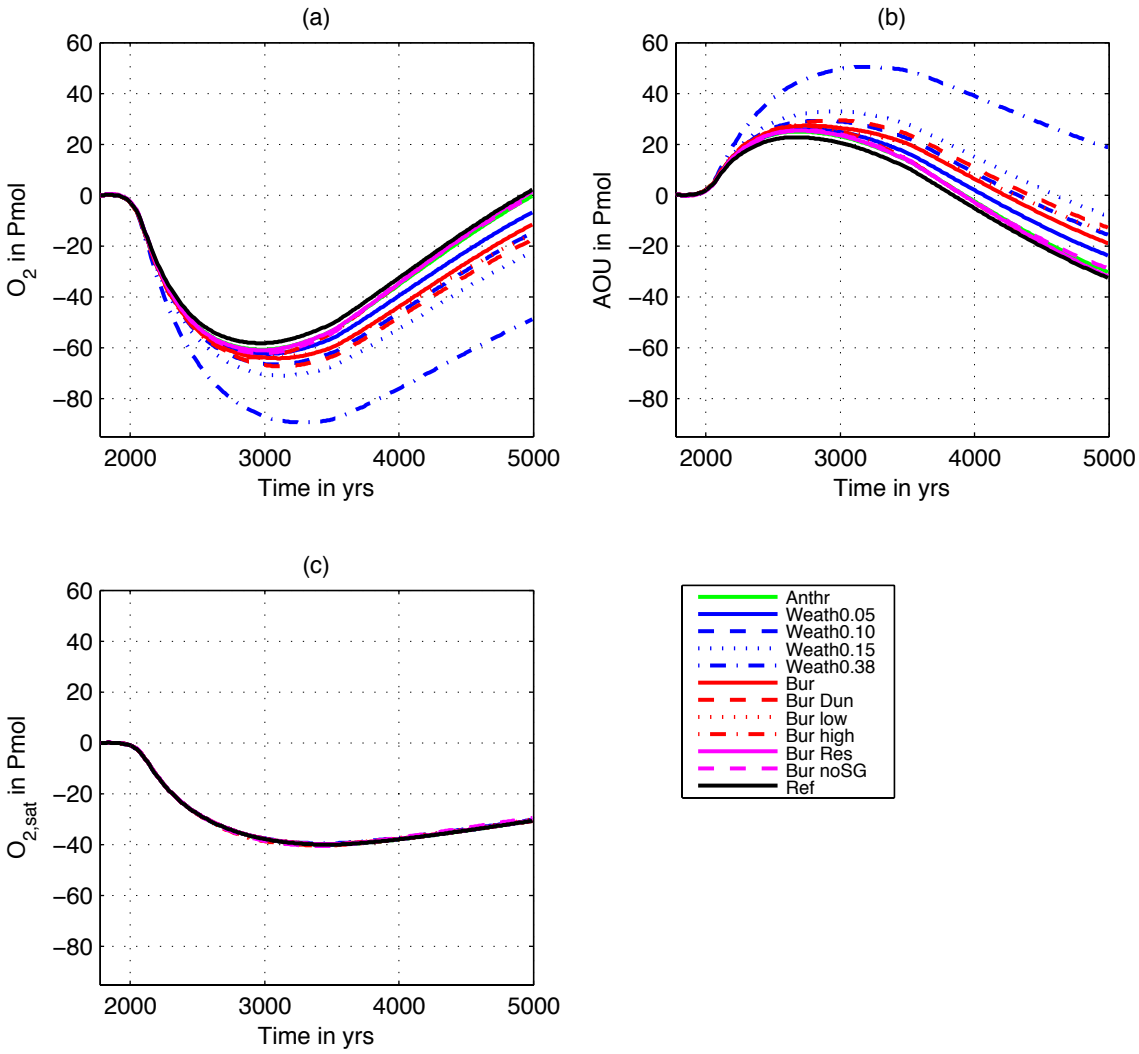

Fig. 5.8: Anomalies of globally integrated (a) oxygen (O_2), (b) apparent oxygen utilization (AOU) and (c) oxygen saturation ($O_{2,sat}$) in Pmol. Simulation descriptions can be found in Table 1.

Anomalies in AOU are inversely related to the changes in ocean oxygen and explain variations in oxygen levels among the different model simulations (compare Fig. 5.8a and 5.8b). Increasing oxygen utilization contributes to the decrease of the ocean oxygen level until year 3000. After year 3000, a distinct negative trend in AOU contributes to an oxygenation of the ocean. For simulations with a larger P inventory, the AOU has a positive offset to the *Ref* simulation. In contrast to this is the trend not affected by the P inventory. This could possibly related to N limitation (compare Fig. 5.7b and Fig. 5.8b).

Anomalies in AOU (Fig. 5.9, blue lines) can be explained by the difference between preformed nutrients (Fig. 5.9, red and black dashed lines as anomalies) and total integrated nutrients (Fig. 5.9, red and black solid lines as anomalies), here given in units Pmol O related to elemental ratios (O:N=10 and O:P=160). These elemental ratios are applied in the model for remineralization processes of detritus to estimate the amount of utilized oxygen. Preformed nutrients are nutrients that leave the ocean unutilized, for example in the Southern Ocean a large fraction of nutrients leave the surface as

preformed nutrients. The fraction of utilized and preformed nutrients can change and could affect the oxygen state of the ocean.

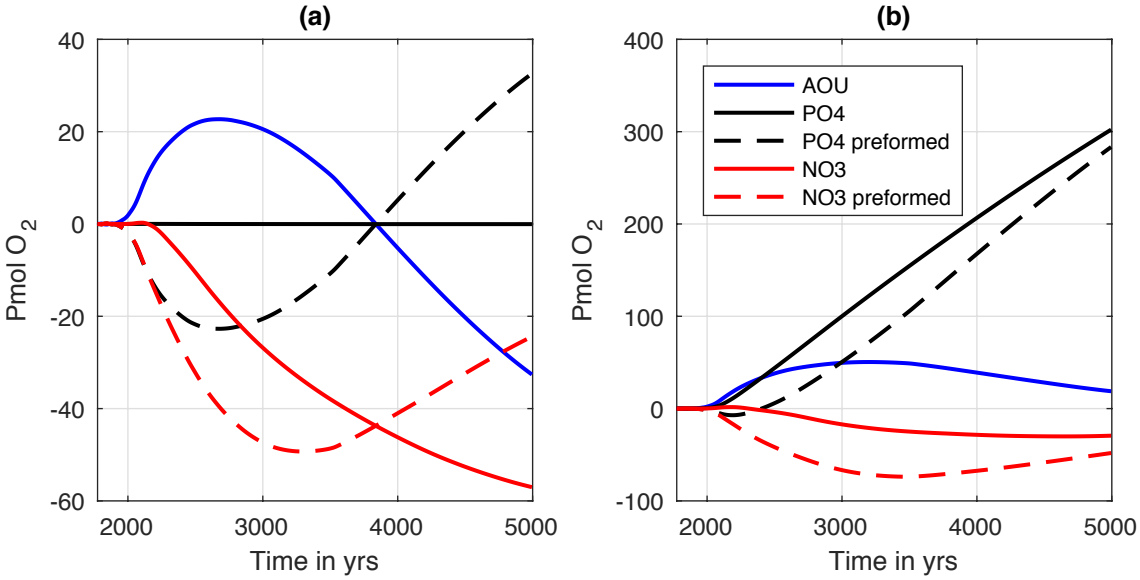

Fig. 5.9: Anomalies of globally integrated apparent oxygen utilization (AOU, blue line), PO_4 (black solid line), PO_4 preformed (black dashed line), NO_3 (red solid line) and NO_3 preformed (red dashed line) here expressed in equivalents of Pmol O_2 using fixed Redfield ratios (O:N=10 and O:P=160) for the (a) Ref simulation and the (b) Weath0.38 simulation.

In the *Ref* simulation (Fig. 5.9a), anomaly of preformed PO_4 is directly invers to the anomaly of AOU, because PO_4 is conserved in this simulation. Until year 2200 changes in circulation and climate seem to be the main driver for a reduction in preformed N and P in the *Ref* simulation, because global N and P inventories (Fig 9a, solid red and black line) are unchanged. During continuous and intense ocean warming a weaker meridional overturning (not shown) reduces ocean ventilation. The meridional overturning decrease from 17 Sv pre-industrial to 11 Sv in year 2200 and start to recover quickly when the rate of global warming reduces. As of year 3000 the meridional overturning is between 20 and 22 Sv. We suggest that a weaker overturning could increase the residence time of water in the surface ocean. This could give P in the polar regions longer time to mix horizontally into regions with lower light limitations. This could explain the reduction in preformed nutrients. Stronger stratification in the ocean tends to reduce the supply of nutrients from the deep ocean and therefore explain the reduced export of organic matter (Fig. 5.6b). However, the regional pattern and strength of export could still have an impact on suboxia or oxygen minimum zones, which are related more to local processes than to global budgets.

After year 2200 enhanced suboxia drives excess denitrification and a decline in nitrate (Fig. 5.9a red solid line) in the *Ref* simulation. The decline in nitrate explains the negative trend in AOU anomalies and therefore a negative feedback on the global deoxygenation. In the *Weath0.38* simulation the added P stimulates nitrogen fixation by

diazotrophs and counteracts the denitrification (Fig. 5.9b, red solid line), which increases N by 28 Pmol O. Furthermore, the high availability of P seems to reduce preformed N by 24 Pmol O. Both could explain the difference between *Weath0.38* and *Ref* of 52 Pmol O in AOU at the end of the simulation (Fig. 5.8b). However, approximately 92% of the added P in the *Weath0.38* simulation remains unused and leaves the surface ocean as preformed P. The negative feedback in the nitrogen cycle reduces the effect of P addition on the global oxygen level.

5.5 Discussion and Conclusions

Uncertainties in the development of the P inventory can be driven by different realization of weathering or benthic fluxes in the UVic model. We use here P weathering fluxes from observational estimates for calibration. These estimates suggest large uncertainties in land to ocean P-fluxes, which could vary from 0.05 to 0.30 Tmol P a^{-1} (Benitez-Nelson, 2000; Compton et al., 2000; Ruttenberg, 2003). This significantly contributes to uncertainties in the development of the global P inventory (Fig. 5.2, blue lines). In this study, we see an increase in global ocean P inventory by 60% by the year 5000 (Fig. 5.2b) in the Weath0.38 simulation. This seems to be surprisingly high, but several studies indicate that changes in past climate could also have gone along with substantial changes in the P inventory (Planavsky et al., 2010; Monteiro et al., 2012; Wallmann, 2014).

The representation of benthic P-fluxes is realized in the UVic model by a transfer function on a sub-grid bathymetry. The sub-grid bathymetry improves substantially rain rate of particular organic carbon (RRPOC) on the sediment (Table 2). In particular, RRPOC is increased on the shelf, which most geological models do not resolve. Transfer functions can systematically overestimate the release of benthic P on long time scales, because transfer functions do not take into account local P inventory and its limitation for the P release. In the UVic model, sediments under low-oxygen conditions could be quickly depleted already after years or decades (Fig. 5.2, dashed purple line).

The increased P inventory (Fig. 5.2b) promotes deoxygenation (Fig. 5.5) and expansion of suboxia, but a net loss in nitrate limits the utilization of P by phytoplankton. Wallmann (2003) already recognized that for an eutrophied ocean, eventually nitrate limits productivity. As a consequence, large amounts of P leave the surface unused as preformed P (Fig. 5.9b), bypass the remineralization process and therefore have no impact on oxygen or deoxygemation. Low N/P ratios are thought to give N_2-fixers a competitive advantage over ordinary phytoplankton and lead to an extensive increase in nitrogen fixation and concentration of diazotrophs in the ocean (Fig. 5.7a). A substantial increase in nitrogen fixation was also discovered in a study by Kuypers et al. (2004). Kuypers et al. (2004) indicated that newly fixed nitrogen was the main source for nitrate during oceanic anoxic events. However, high denitrification rates remove nitrate from the global ocean and in the UVic model nitrogen-fixers are not able to compensate for

the loss (Fig. 5.7b). This could indicate that deoxygenation studies without a nitrogen cycle could miss a negative feedback limiting global deoxygenation, but a lack in the representation of nitrogen fixers in the UVic model could be also a plausible explanation, as results from Kuypers et al. (2004) indicate.

Several model limitations can add uncertainty to our results, which we present in the following. As the first limitation, benthic denitrification is not simulated in the UVic model, which could even more increase N-limitation and reduce the effect of P fluxes on the biological pump. Sea level change and the implied bathymetry change is not simulated in the UVic model. In future projections, higher surface air temperatures would lead to a sea level rise, which increase global coverage of shelf areas. Burial of P is more effective on the shelf (Flögel et al., 2011), which would remove P from the ocean and lead to a lower P residence time (Bjerrum et al., 2006). This negative feedback on the P cycle is not simulated in the UVic model, because bathymetry is fixed during the individual model simulations. Uncertainties in the representation of marine biology could affect the uptake of nutrients and the biological pump. In the UVic model, we consider fixed Redfield-ratio stoichiometry and do not consider adaptation abilities of phytoplankton or different species. Future deoxygenation studies with Earth system models should also consider the potential of variable N:P stoichiometry due to adaptation or changes in community composition. In the UVic model, no distinction is done between particular and dissolved weathering fluxes of P. The delivery of riverine particulate P to the ocean could be affected by increased damming of water for hydropower (Seitzinger et al., 2010). Dams trap part of the particulate P before it is able to reach the open ocean.

To conclude, climate warming leads to a larger ocean P inventory mainly due to addition of P by weathering, release from the sediment and benthic recycling of P. However, the uncertainties in the model formulations are still too large to give reliable quantitative estimates for ocean deoxygenation, which should be taken into account for model improvement and future studies.

6. Overall conclusion and outlook

6.1 Summary and conclusion

Earth system feedbacks play an important role in predicting the response of the Earth climate to anthropogenic forcing. The strength and direction of feedbacks could potentially determine whether anthropogenic greenhouse gas emissions are able to push the climate system or a subsystem of the climate into a new equilibrium state or not. In this thesis two sub-systems are investigated, the North African climate system and its response to irrigated afforestation (Chapters 2 and 3) and the ocean oxygen state and its response to global warming (Chapter 4 and 5). Detailed conclusions to these two case studies are given further on in this chapter. It should be mentioned, that each case study is conducted with just one model, and the following conclusions only apply for the specific model. Strength and sign of the investigated feedbacks could be model-dependent.

1. Are atmospheric feedbacks able to sustain an artificial Green Sahara? And if not, to what extent is an artificial Green Sahara self-sustainable? What role do the atmospheric feedbacks play in the self-sustainability of an artificial Green Sahara? (Chapter 2)

- Atmospheric feedbacks would reduce precipitation potential over an irrigated artificial Green Sahara and probably prevent it from self-sustainability.
- The local water recycling feedback is weak. Only 26% of the evapotranspirated water re-precipitates over an artificial Green Sahara. Considerable large amounts are advected to the Sahel zone and to the North Atlantic. The advection affects also the water-vapor feedback. In contrast to ocean regions, over land the water-vapor feedback is limited by the availability of moisture, and the advection reduces the availability of moisture over the Sahara.
- A circulation-precipitation feedback reduces the potential for precipitation over the Green Sahara. Enhanced evapotranspiration moistens Saharan air and leads to radiative cooling. The moist air is advected southward to the Sahel zone and promotes high-level cloud formation as well as atmospheric warming. Both lead to a circulation anomaly with descending air over the Sahara and ascending air over the Sahel zone, which reduces precipitation over the Sahara. The cloud closely interacts with the circulation-precipitation feedback.
- Maximum surface temperatures determine the position of low-level convection and therefore affect the precipitation potential. In the Sahara temperatures decrease by 6K. The water-vapor feedback and the vegetation albedo feedback are not able to increase the surface temperature, instead low-level clouds and intensive latent heat fluxes lead to a net cooling in the Sahara. The temperature

reduction in the Sahara shifts the temperature maximum from the Sahara into the Sahel zone, which affect the position of the ITCZ and also the northward-extent of WAM precipitation.
- The soil moisture feedback intensifies WAM precipitation, but does not necessarily affect precipitation in the Sahara as long as the WAM does not move northward into the Sahara.

2. How does the artificial Green Sahara affect the tropical cyclone development? (Chapter 3)

- Environmental conditions for tropical cyclones are improved in the North Atlantic and the tropical cyclones are intensified by moisture advection from the irrigated and afforested Sahara.
- The advected moisture from the Green Sahara induces changes in mid-tropospheric relative humidity, sea surface temperatures, vertical wind shear and maximum potential intensity over the North Atlantic, which would contribute to an intensification of North Atlantic tropical cyclones.
- The irrigated afforestation of the Sahara has a substantially larger effect on the tropical cyclone development than a worst-case global warming scenario

3. Is it possible that anthropogenic climate change can drive the ocean anoxic on millennial timescales? How does phosphorus weathering and benthic phosphorus fluxes affect the development of ocean anoxia? What is the role of biogeochemical feedbacks in the development of future ocean anoxia? Does the oxygen-productivity feedback lead to a positive runaway feedback and turn the ocean anoxic? (Chapter 4)

- Anthropogenic climate change does not lead to global large-scale anoxia, but to substantially enlarged oxygen minimum zones.
- The phosphorus input from weathering and benthic release fluxes leads to 4- to 5-fold expansion of the suboxic water volume (until year 3000), considerably larger than for simulations with constant P inventory.
- Benthic phosphorus release plays a minor role in the oxygen productivity feedback for the expansion of suboxia and does not lead to a positive runaway feedback regarding the global ocean deoxygenation.

4. How does the future phosphorus inventory change on millennial timescales, what are the uncertainties and what are drivers of uncertainties? What are the consequences for the deoxygenation of the ocean? What is the role of nitrate limitation? (Chapter 5)

- In general, climate warming leads to a larger ocean phosphorus inventory mainly due to weathering and benthic fluxes.
- Largest uncertainties in phosphorus inventories on millennial timescales appear from the formulation of the benthic and weathering fluxes, while anthropogenic fluxes have a minor impact. A better representation of the bathymetry by the integrated sub-grid bathymetry substantially improves burial fluxes of phosphorus. Benthic fluxes of phosphorus could be systematically overestimated, because the sediment to ocean release fluxes are not limited by a local phosphorus inventory. Limiting of the phosphorus inventory of the sediment reduces uncertainties and the general contribution of benthic phosphorus fluxes to the ocean inventory.
- Uncertainties in phosphorus fluxes substantially affect estimates of expansion of local suboxia. Suboxic volume ranges between 1 and 5% of the global ocean in year 5000.
- Global deoxygenation is also subject to large uncertainties. In year 5000, the simulations exhibit a spread in the global oxygen of 50 Pmol O_2 due to variations in the oceanic phosphorus inventory. In comparison, reduced solubility of oxygen leads to a decrease in the global oxygen of 30 Pmol O_2.
- Nitrate limitation increases preformed phosphorus fraction in the ocean (up to 90% for the *Weath0.38* simulation) and limits therefore the effect of phosphorus addition on global deoxygenation. Enhanced denitrification due to expansion of suboxic volume acts as a negative feedback on deoxygenation.

6.2 Outlook and evaluation of project ideas

This thesis can answer several questions to the presented two case studies, but also reveals new questions. This section presents a number of scientific questions arising from the results obtained so far. It is less an outlook, but more an evaluation of project ideas, which evolved during the PhD thesis.

The afforestation case study raises the question, if such a climate engineering project is reasonable. The low level of self-sustainability and the intensification of tropical cyclones in the North Atlantic are the main concerns. In this PhD thesis, the following project ideas came up:

- Simulations of an irrigated afforested Sahara with a dynamic dust cycle. The dust-precipitation feedback could enhance self-sustainability of an artificial Green Sahara.
- Re-evaluating the feasibility of such a project by implementing a simple model for economic damages by tropical cyclones (similar to Narita et al. (2009)) into an optimization study (complementary to the study from Bowring et al. (2014)).
- Evaluation of changes in the El Niño-Southern Oscillation. Preliminary results indicate a significant impact from the irrigated afforestation of the Sahara on the atmospheric dynamics and circulation in the equatorial Pacific.

The ocean deoxygenation case study showed that the here used model formulation for weathering and benthic fluxes of P are not sufficient enough to give reliable future projections of the oceanic deoxygenation. The study indicated also further uncertainties in the representation of denitrification processes. The following ideas are proposed:

- Simulations with a full complex sediment model and with a representation of P in the sediment model (for example the sediment model in Palastanga et al. (2011)) give more possibilities to reduce uncertainties. Sediment profiles can be compared to profiles from present-day and palaeo sediment cores or to palaeo reconstructions. The inventory of P is implicitly modelled and no assumptions have to be made. The large uncertainties from the formulation of benthic P fluxes from the here used transferfunctions can be avoided.
- A more sophisticated weathering model (Brault et al., 2017) and a coast mask to emulate coastal P processes could improve the presentation of ocean input of P by weathering.
- Over the last glacial cycle, sea level changes over the range of 100m occurred. Simulations with an adaptable sediment depth and a modern sub-grid bathymetry could reveal an interesting insight in the long-term nutrient dynamics during the last glacial cycle.

Bibliography

Aiyyer A, Thorncroft CD (2006) Climatology of vertical wind shear over the tropical Atlantic. J Clim 19:2969–2983. doi: 10.1175/JCLI3685.1

Allaway WG, Mansfield TA (1967) Stomatal Responses To Changes in Carbon Dioxide Concentration in Leaves Treated. New Phytol 66:57–63.

Archer D (1996) A data driven model of the global calcite lysocline. Global Biogeochem Cycles 10:511–526.

Ayars JE, Christen EW, Hornbuckle JW (2006) Controlled drainage for improved water management in arid regions irrigated agriculture. Agric Water Manag 86:128–139. doi: 10.1016/j.agwat.2006.07.004

Bathiany S, Claussen M, Brovkin V, Raddatz T, Gayler V (2010) Combined biogeophysical and biogeochemical effects of large-scale forest cover changes in the MPI earth system model. Biogeosciences 7:1383–1399. doi: 10.5194/bg-7-1383-2010

Baturin GN (2007) Issue of the relationship between primary productivity of organic carbon in ocean and phosphate accumulation (Holocene-Late Jurassic). Lithol Miner Resour 42:318–348. doi: 10.1134/S0024490207040025

Bauer KW, Zeebe RE, Wortmann UG (2016) Quantifying the volcanic emissions which triggered Oceanic Anoxic Event 1a and their effect on ocean acidification Associate Editor – Stuart Robinson. 204–214. doi: 10.1111/sed.12335

Benitez-Nelson CR (2000) The biogeochemical cycling of phosphorus in marine systems. EarthEarth Sci Rev 51:109–135. doi: 10.1016/S0012-8252(00)00018-0

Berner, R. A.(1991) Weathering, plants and the long-term carbon cycle. Geochim. Cosmochim. Acta, 56, 3225-3231.

Berner R a., Rao J-L (1994) Phosphorus in sediments of the Amazon River and estuary: Implications for the global flux of phosphorus to the sea. Geochim Cosmochim Acta 58:2333–2339. doi: 10.1016/0016-7037(94)90014-0

Betts R a. (2011) Climate science: Afforestation cools more or less. Nat Geosci 4:504–505. doi: 10.1038/ngeo1223

Bianchi D, Dunne JP, Sarmiento JL, Galbraith ED (2012) Data-based estimates of suboxia, denitrification, and N 2 O production in the ocean and their sensitivities to dissolved O 2. Global Biogeochem Cycles 26:n/a-n/a. doi: 10.1029/2011GB004209

Bister M, Emanuel KA (2002) Low frequency variability of tropical cyclone potential intensity 1. Interannual to irtterdecadal variability. J Geophys Res Atmos. doi: 10.1029/2001JD000776

Bitz CM, Lipscomb WH (1999) An energy-conserving thermodynamic model of sea ice. J Geophys Res 104:15669. doi: 10.1029/1999JC900100

Bjerrum CJ, Bendtsen J, Legarth JJF (2006) Modeling organic carbon burial during sea level rise with reference to the Cretaceous. doi: 10.1029/2005GC001032

Blättler CL, Jenkyns HC, Reynard LM, Henderson GM (2011) Significant increases in

global weathering during Oceanic Anoxic Events 1a and 2 indicated by calcium isotopes. Earth Planet Sci Lett 309:77–88. doi: 10.1016/j.epsl.2011.06.029

Bohlen L, Dale AW, Wallmann K (2012) Simple transfer functions for calculating benthic fixed nitrogen losses and C:N:P regeneration ratios in global biogeochemical models. Global Biogeochem Cycles. doi: 10.1029/2011GB004198

Bopp L, Le Quéré C, Heimann M, Manning AC, Monfray P (2002) Climate-induced oceanic oxygen fluxes: Implications for the contemporary carbon budget. Global Biogeochem Cycles 16:6-1-6–13. doi: 10.1029/2001GB001445

Bopp L, Resplandy L, Orr JC, Doney SC, Dunne JP, Gehlen M, Halloran P, Heinze C, Ilyina T, Séférian R, Tjiputra J, Vichi M (2013) Multiple stressors of ocean ecosystems in the 21st century: projections with CMIP5 models. Biogeosciences 10:6225–6245. doi: 10.5194/bg-10-6225-2013

Bowring SPK, Miller LM, Ganzeveld L, Kleidon A (2014) Applying the concept of "energy return on investment" to desert greening of the Sahara/Sahel using a global climate model. Earth Syst Dyn 5:43–53. doi: 10.5194/esd-5-43-2014

Boyce DG, Lewis MR, Worm B (2010) Global phytoplankton decline over the past century. Nature, 466, 7306, 591-596.

Braconnot P, Otto-Bliesner B, Harrison S, Joussaume S, Peterchmitt JY, Abe-Ouchi A, Crucifix M, Driesschaert E, Fichefet T, Hewitt CD, Kageyama M, Kitoh A, Laîné A, Loutre MF, Marti O, Merkel U, Ramstein G, Valdes P, Weber SL, Yu Y, Zhao Y (2007) Results of PMIP2 coupled simulations of the Mid-Holocene and Last Glacial Maximum - Part 1: experiments and large-scale features. Clim Past 3:261–277. doi: 10.5194/cp-3-261-2007

Brault MO, Matthews HD, Mysak LA (2017) The importance of terrestrial weathering changes in multimillennial recovery of the global carbon cycle: A two-dimensional perspective. Earth Syst Dyn 8:455–475. doi: 10.5194/esd-8-455-2017

Braun SA, Sippel JA, Nolan DS (2012) The Impact of Dry Midlevel Air on Hurricane Intensity in Idealized Simulations with No Mean Flow. J Atmos Sci 69:236–257. doi: 10.1175/JAS-D-10-05007.1

Broccoli AJ, Dahl KA, Stouffer RJ (2006) Response of the ITCZ to Northern Hemisphere cooling. Geophys Res Lett 33:1–4. doi: 10.1029/2005GL024546

Budyko MI (1968) The effect of solar radiation variations on the climate of the Earth.

Burdige DJ (2007) Preservation of organic matter in marine sediments: Controls, mechanisms, and an imbalance in sediment organic carbon budgets? Chem Rev 107:467–485. doi: 10.1021/cr050347q

Burwicz EB, Rüpke LH, Wallmann K (2011) Estimation of the global amount of submarine gas hydrates formed via microbial methane formation based on numerical reaction-transport modeling and a novel parameterization of Holocene sedimentation. Geochim Cosmochim Acta 75:4562–4576. doi: 10.1016/j.gca.2011.05.029

Cabré A, Marinov I, Bernardello R, Bianchi D (2015) Oxygen minimum zones in the tropical Pacific across CMIP5 models: mean state differences and climate change trends. Biogeosciences 12:5429–5454. doi: 10.5194/bg-12-5429-2015

Camargo SJ (2013) Global and regional aspects of tropical cyclone activity in the CMIP5 models. J Clim 26:9880–9902. doi: 10.1175/JCLI-D-12-00549.1

Camargo SJ, Ting M, Kushnir Y (2013) Influence of local and remote SST on North Atlantic tropical cyclone potential intensity. Clim Dyn 40:1515–1529. doi: 10.1007/s00382-012-1536-4

Charney JG (1975) Dynamics of deserts and drought in the Sahel. Q J R Meteorol Soc 101:193–202. doi: 10.1002/qj.49710142802

Chen TC, Wang SY, Clark AJ (2008) North Atlantic hurricanes contributed by African esterly waves north and south of the African easterly jet. J Clim 21:6767–6776. doi: 10.1175/2008JCLI2523.1

Cheng W, Moore JC, Cao L, Ji D, Zhao L (2017) Simulated climate effects of desert irrigation geoengineering. Sci Rep 7:46443. doi: 10.1038/srep46443

Clark PU, Shakun JD, Marcott SA, Mix AC, Eby M, Kulp S, Levermann A, Milne GA, Pfister PL, Santer BD, Schrag DP, Solomon S, Stocker TF, Strauss BH, Weaver AJ, Winkelmann R, Archer D, Bard E, Goldner A, Lambeck K, Pierrehumbert RT, Plattner G-K (2016) Consequences of twenty-first-century policy for multi-millennial climate and sea-level change. Nat Clim Chang 6:360–369. doi: 10.1038/nclimate2923

Claussen M, Kubatzki C, Brovkin V, Ganopolski A, Hoelzmann P, Pachur H-J (1999) Simulation of an abrupt change in Saharan vegetation in the mid-Holocene. Geophys Res Lett 26:2037–2040. doi: 10.1029/1999GL900494

Colbert AJ, Soden BJ (2012) Climatological variations in North Atlantic tropical cyclone tracks. J Clim 25:657–673. doi: 10.1175/JCLI-D-11-00034.1

Colmann AS, Holland HD (2000) The global diagenetic flux of phosphorus from marine sediments to the ocean: Redox sensitivity and the control of atmospheric oxygen levels. Marine Authigenesis: from global to Microbial, 66, 53-75.

Compton J, Mallinson D, Glenn CR, Filippelli G, Föllmi K, Shields G, Zanin Y (2000) Variations in the global phosphorus cycle. Marine Authigenesis: From Global to Microbial, 66, 21-33.

Cook K, Meehl G a, Arblaster JM (2012) Monsoon Regime and Processes in CCSM4. Part II: African and American Monsoon Systems. J Clim 25:2609–2621. doi: 10.1175/JCLI-D-11-00185.1

Cook KH (1999) Generation of the African Easterly Jet and Its Role in Determining West African Precipitation. J Clim 12:1165–1184. doi: 10.1175/1520-0442(1999)012<1165:GOTAEJ>2.0.CO;2

Cook KH, Vizy EK (2006) Coupled Model Simulations of the West African Monsoon System: Twentieth- and Twenty-First-Century Simulations. J Clim 19:3681–3703. doi: 10.1175/JCLI3814.1

Damsté JSS, Kuypers MMM, Pancost RD, Schouten S (2008) The carbon isotopic response of algae, (cyano)bacteria, archaea and higher plants to the late Cenomanian perturbation of the global carbon cycle: Insights from biomarkers in black shales from the Cape Verde Basin (DSDP Site 367). Org Geochem 39:1703–1718. doi: 10.1016/j.orggeochem.2008.01.012

Danabasoglu G, Bates SC, Briegleb BP, Jayne SR, Jochum M, Large WG, Peacock S,

Yeager SG (2012) The CCSM4 Ocean Component. J Clim 25:1361–1389. doi: 10.1175/JCLI-D-11-00091.1

DeMaria M (1996) The Effect of Vertical Shear on Tropical Cyclone Intensity Change. J. Atmos. Sci. 53:2076–2088.

DeMott PJ, Sassen K, Poellot MR, Baumgardner D, Rogers DC, Brooks SD, Prenni AJ, Kreidenweis SM (2003) African dust aerosols as atmospheric ice nuclei. Geophys Res Lett 30:26–29. doi: 10.1029/2003GL017410

Devaraju N, Bala G, Modak A (2015) Effects of large-scale deforestation on precipitation in the monsoon regions: Remote versus local effects. Proc Natl Acad Sci 112:201423439. doi: 10.1073/pnas.1423439112

Diongue A, Lafore J-P, Redelsperger J-L, Roca R (2002) Numerical study of a Sahelian synoptic weather system: Initiation and mature stages of convection and its interactions with the large-scale dynamics. Q J R Meteorol Soc 128:1899–1927. doi: 10.1256/003590002320603467

Doi T, Vecchi GA, Rosati AJ, Delworth TL (2013) Response to CO2 doubling of the Atlantic hurricane main development region in a high-resolution climate model. J Clim 26:4322–4334. doi: 10.1175/JCLI-D-12-00110.1

Dunion JP, Velden CS (2004) The impact of the Saharan Air Layer on Atlantic tropical cyclone activity. Bull Am Meteorol Soc 85:353–365. doi: 10.1175/BAMS-85-3-353

Dunne JP, Sarmiento JL, Gnanadesikan A (2007) A synthesis of global particle export from the surface ocean and cycling through the ocean interior and on the seafloor. Global Biogeochem Cycles 21:1–16. doi: 10.1029/2006GB002907

Eby M, Zickfeld K, Montenegro A, Archer D, Meissner KJ, Weaver AJ (2009) Lifetime of Anthropogenic Climate Change: Millennial Time Scales of Potential CO 2 and Surface Temperature Perturbations. J Clim 22:2501–2511. doi: 10.1175/2008JCLI2554.1

Elsner JB, Kossin JP, Jagger TH (2008) The increasing intensity of the strongest tropical cyclones. Nature 455:92–95. doi: 10.1038/nature07234

Evan AT, Dunion J, Foley JA, Heidinger AK, Velden CS (2006) New evidence for a relationship between Atlantic tropical cyclone activity and African dust outbreaks. Geophys Res Lett 33:1–5. doi: 10.1029/2006GL026408

Fanning AF, Weaver AJ (1996) An atmospheric energy-moisture balance model: Climatology, interpentadal climate change, and coupling to an ocean general circulation model. J Geophys Res 101:15111. doi: 10.1029/96JD01017

Filippelli GM (2001) Carbon and phosphorus cycling in anoxic sediments of the Saanich Inlet, British Columbia. Mar Geol 174:307–321. doi: 10.1016/S0025-3227(00)00157-2

Filippelli GM (2002) The Global Phosphorus Cycle. Rev Mineral Geochemistry 48:391–425. doi: 10.2138/rmg.2002.48.10

Filippelli GM (2008) The Global Phosphorus Cycle: Past, Present, and Future. Elements 4:89–95. doi: 10.2113/GSELEMENTS.4.2.89

Filippelli GM, Delaney ML (1996) Phosphorus geochemistry of equatorial Pacific

sediments. Geochim Cosmochim Acta 60:1479–1495. doi: 10.1016/0016-7037(96)00042-7

Flögel S, Wallmann K, Poulsen CJ, Zhou J, Oschlies a., Voigt S, Kuhnt W (2011) Simulating the biogeochemical effects of volcanic CO2 degassing on the oxygen-state of the deep ocean during the Cenomanian/Turonian Anoxic Event (OAE2). Earth Planet Sci Lett 305:371–384. doi: 10.1016/j.epsl.2011.03.018

Föllmi KB (1996) The phosphorus cycle , phosphogenesis phosphate-rich deposits. Earth-Science Rev 40:55–124.

Frank WM, Ritchie EA (2001) Effects of Vertical Wind Shear on the Intensity and Structure of Numerically Simulated Hurricanes. Mon Weather Rev 129:2249–2269. doi: 10.1175/1520-0493(2001)129<2249:EOVWSO>2.0.CO;2

Froelich P. N.: Interactions of the marine phosphorus and carbon cycles, in Moore, B. and Dastoor, M. N., eds., The Interaction of Global Biogeochemical Cycles: Pasadena, California Institute of Technology, NASA - JPL Publication 84-21, 141-176, 1984.

Froelich PN, Bender ML, Luedtke N a., Heath GR, DeVries T (1982) The marine phosphorous cycle. Am. J. Sci. 282:474–511. doi: 10.2475/ajs.282.4.474

Fuller DQ, van Etten J, Manning K, Castillo C, Kingwell-Banham E, Weisskopf A, Qin L, Sato Y-I, Hijmans RJ (2011) The contribution of rice agriculture and livestock pastoralism to prehistoric methane levels. The Holocene 21:743–759. doi: 10.1177/0959683611398052

Garcia RR, Marsh DR, Kinnison DE, Boville BA, Sassi F (2007) Simulation of secular trends in the middle atmosphere, 1950-2003. J Geophys Res Atmos 112:1–23. doi: 10.1029/2006JD007485

Getzlaff J, Dietze H, Oschlies A (2016) Simulated effects of southern hemispheric wind changes on the Pacific oxygen minimum zone. Geophys Res Lett 43:728–734. doi: 10.1002/2015GL066841

Gray WM (1968) Global View of the Origin of Tropical Disturbances and Storms. Mon Weather Rev 96:669–700. doi: 10.1175/1520-0493(1968)096<0669:GVOTOO>2.0.CO;2

Gregg WW (2005) Recent trends in global ocean chlorophyll. Geophys Res Lett 32:L03606. doi: 10.1029/2004GL021808

Grist JP, Nicholson SE (2001) A Study of the Dynamic Factors Influencing the Rainfall Variability in the West African Sahel. J Clim 14:1337–1359. doi: 10.1175/1520-0442(2001)014<1337:ASOTDF>2.0.CO;2

Gualdi S, Scoccimarro E, Navarra a. (2008) Changes in Tropical Cyclone Activity due to Global Warming: Results from a High-Resolution Coupled General Circulation Model. J Clim 21:5204–5228. doi: 10.1175/2008JCLI1921.1

Hall A, Manabe S (1999) The role of water vapor feedback in unperturbed climate variability and global warming. J Clim 12:2327–2346. doi: Doi 10.1175/1520-0442(1999)012<2327:Trowvf>2.0.Co;2

Handoh IC, Lenton TM (2003) Periodic mid-Cretaceous oceanic anoxic events linked by oscillations of the phosphorus and oxygen biogeochemical cycles. Global Biogeochem Cycles 17:1–11. doi: 10.1029/2003GB002039

Harlaß J, Latif M, Park W (2015) Improving climate model simulation of tropical Atlantic sea surface temperature: The importance of enhanced vertical atmosphere model resolution. 1–8. doi: 10.1002/2015GL063310.Received

Harrison JA, Seitzinger SP, Bouwman AF, Caraco NF, Beusen AHW, Vörösmarty CJ (2005) Dissolved inorganic phosphorus export to the coastal zone: Results from a spatially explicit, global model. Global Biogeochem Cycles. doi: 10.1029/2004GB002357

Harrison SP, Bartlein PJ, Izumi K, Li G, Annan J, Hargreaves J, Braconnot P, Kageyama M (2015) Evaluation of CMIP5 palaeo-simulations to improve climate projections. Nat Clim Chang 5:735–743. doi: 10.1038/nclimate2649

Held IM, Soden BJ (2000) Water Vapor Feedback and Global Warming. Annu Rev Energy Environ 25:441–475. doi: 10.1146/annurev.energy.25.1.441

Hibler WD (1979) A dynamic thermodynamic sea ice model. J. Phys. Oceanogr., 9, 815–846.

Hill KA, Lackmann GM (2009) Influence of Environmental Humidity on Tropical Cyclone Size. Mon Weather Rev 137:3294–3315. doi: 10.1175/2009MWR2679.1

Hofmann M, Schellnhuber HJ (2010) Ocean acidification: a millennial challenge. Energy Environ. Sci., 3, 1883-1896. doi: 10.1039/C000820F

Holland MM, Bailey D a., Briegleb BP, Light B, Hunke E (2012) Improved Sea Ice Shortwave Radiation Physics in CCSM4: The Impact of Melt Ponds and Aerosols on Arctic Sea Ice*. J Clim 25:1413–1430. doi: 10.1175/JCLI-D-11-00078.1

Huffman GJ, Bolvin DT, Nelkin EJ, Wolff DB, Adler RF, Gu G, Hong Y, Bowman KP, Stocker EF (2007) The TRMM Multisatellite Precipitation Analysis (TMPA): Quasi-Global, Multiyear, Combined-Sensor Precipitation Estimates at Fine Scales. J Hydrometeorol 8:38–55. doi: 10.1175/JHM560.1

Hunke EC, Dukowicz JK (1997) An Elastic-Viscous-Plastic Model for Sea Ice Dynamics. J. Phys. Oceanogr., 27 (9), 1849-1867.

Ingall E, Jahnke R (1994) Evidence for enhanced phosphorus regeneration from marine sediments overlain by oxygen depleted waters. Geochim Cosmochim Acta 58:2571–2575. doi: 10.1016/0016-7037(94)90033-7

IPCC, 2013: Summary for Policymakers. In: Climate Change 2013: The Physical Science Basis. Contribution of Working Group I to the Fifth Assessment Report of the Intergovernmental Panel on Climate Change [Stocker, T.F., D. Qin, G.-K. Plattner, M. Tignor, S.K. Allen, J. Boschung, A. Nauels, Y. Xia, V. Bex and P.M. Midgley (eds.)]. Cambridge University Press, Cambridge, United Kingdom and New York, NY, USA

Irizarry-Ortiz MM, Wang G, Eltahir EAB (2003) Role of the biosphere in the mid-Holocene climate of West Africa. J Geophys Res D Atmos 108:ACL 5-1 ACL 5-15. doi: Artn 4042 Doi 10.1029/2001jd000989

Jenkyns HC (2010) Geochemistry of oceanic anoxic events. Geochemistry, Geophys Geosystems 11:1–30. doi: 10.1029/2009GC002788

Jones CE, Jenkyns HC (2001) Seawater strontium isotopes, oceanic anoxic events, and seafloor hydrothermal activity in the Jurassic and Cretaceous. Am J Sci 301:112–

149. doi: 10.2475/ajs.301.2.112

Kafando P, Chane-Ming F, Petitdidier M (2015) Stratospheric variability of wave activity and parameters in equatorial coastal and tropical sites during the West African monsoon. Clim Dyn. doi: 10.1007/s00382-015-2764-1

Kaplan JO, Krumhardt KM, Ellis EC, Ruddiman WF, Lemmen C, Goldewijk KK (2011) Holocene carbon emissions as a result of anthropogenic land cover change. The Holocene 21:775–791. doi: 10.1177/0959683610386983

Keller DP, Feng EY, Oschlies A (2014) Potential climate engineering effectiveness and side effects during a high carbon dioxide-emission scenario. Nat Commun 5:3304. doi: 10.1038/ncomms4304

Keller DP, Kriest I, Koeve W, Oschlies A (2016) Southern Ocean biological impacts on global ocean oxygen. Geophys Res Lett 43:6469–6477. doi: 10.1002/2016GL069630

Keller DP, Oschlies A, Eby M (2012) A new marine ecosystem model for the University of Victoria Earth System Climate Model. Geosci Model Dev 5:1195–1220. doi: 10.5194/gmd-5-1195-2012

Kemena TP, Matthes K, Martin T, Wahl S, Oschlies A (2017) Atmospheric feedbacks in North Africa from an irrigated, afforested Sahara. Clim Dyn. doi: 10.1007/s00382-017-3890-8

Kidder DL, Worsley TR (2010) Phanerozoic Large Igneous Provinces (LIPs), HEATT (Haline Euxinic Acidic Thermal Transgression) episodes, and mass extinctions. Palaeogeogr Palaeoclimatol Palaeoecol 295:162–191. doi: 10.1016/j.palaeo.2010.05.036

Kidder DL, Worsley TR (2012) A human-induced hothouse climate? GSA Today 22:4–11. doi: 10.1130/G131A.1

Kimball SK (2006) A modeling study of hurricane landfall in a dry environment. Mon Weather Rev 134:1901–1918. doi: 10.1175/MWR3155.1

Kojima T, Kakubari Y, Komiyama H (1995) Significance of afforestation of desert and its evaluation as a countermeasure against carbon dioxide problem. Energy Convers Manag 36:923–926. doi: 10.1016/0196-8904(95)00154-6

Kraal P, Slomp CP, Forster A, Kuypers MMM (2010) Phosphorus cycling from the margin to abyssal depths in the proto-Atlantic during oceanic anoxic event 2. Palaeogeogr Palaeoclimatol Palaeoecol 295:42–54. doi: 10.1016/j.palaeo.2010.05.014

Kraal P, Slomp CP, Reed DC, Reichart G-J, Poulton SW (2012) Sedimentary phosphorus and iron cycling in and below the oxygen minimum zone of the northern Arabian Sea. Biogeosciences 9:2603–2624. doi: 10.5194/bg-9-2603-2012

Kraus EB (1977) Subtropical droughts and cross-equatorial energy transports. Mon. Weather Rev. 105:1009–1018.

Kuypers MMM, van Breugel Y, Schouten S, Erba E, Damsté JSS (2004) N2-fixing cyanobacteria supplied nutrient N for Cretaceous oceanic anoxic events. Geology 32:853–856. doi: 10.1130/G20458.1

Kvale KF, Meissner KJ, Keller DP (2015) Potential increasing dominance of heterotrophy in the global ocean. Environ Res Lett 10:74009. doi: 10.1088/1748-

9326/10/7/074009

Landolfi A, Dietze H, Koeve W, Oschlies A (2013) Overlooked runaway feedback in the marine nitrogen cycle: The vicious cycle. Biogeosciences 10:1351–1363. doi: 10.5194/bg-10-1351-2013

Landolfi A, Somes CJ, Koeve W, Zamora LM, Oschlies A (2017) Oceanic nitrogen cycling and N 2 O flux perturbations in the Anthropocene. Global Biogeochem Cycles 1–20. doi: 10.1002/2017GB005633

Landsea CW (1993) A Climatology of Intense (or Major) Atlantic Hurricanes. Mon. Weather Rev. 121:1703–1713.

Landsea CW, Gray WM (1992) The Strong Association between Western Sahelian Monsoon Rainfall and Intense Atlantic Hurricanes. J. Clim. 5:435–453.

Latif M, Keenlyside NS (2011) A perspective on decadal climate variability and predictability. Deep Res Part II Top Stud Oceanogr 58:1880–1894. doi: 10.1016/j.dsr2.2010.10.066

Lawrence DM, Oleson KW, Flanner MG, Fletcher CG, Lawrence PJ, Levis S, Swenson SC, Bonan GB (2012) The CCSM4 Land Simulation, 1850–2005: Assessment of Surface Climate and New Capabilities. J Clim 25:2240–2260. doi: 10.1175/JCLI-D-11-00103.1

Leng G, Huang M, Tang Q, Sacks WJ, Lei H, Leung LR (2013) Modeling the effects of irrigation on land surface fluxes and states over the conterminous United States: Sensitivity to input data and model parameters. J Geophys Res Atmos 118:9789–9803. doi: 10.1002/jgrd.50792

Lenton TM, Britton C (2006) Enhanced carbonate and silicate weathering accelerates recovery from fossil fuel CO2 perturbations. Global Biogeochem Cycles 20:1–12. doi: 10.1029/2005GB002678

Lenton TM, Held H, Kriegler E, Hall JW, Lucht W, Rahmstorf S, Joachim H (2008) Tipping elements in the Earth' s climate system. Proc Natl Acad Sci 105:1786–1793. doi: 10.1073/pnas.0705414105

Lenton TM, Watson AJ (2000) Redfield revisited: 1. Regulation of nitrate, phosphate, and oxygen in the ocean. Global Biogeochem Cycles 14:225–248. doi: 10.1029/1999GB900065

Levis S, Bonan GB, Bonfils C (2004) Soil feedback drives the mid-Holocene North African monsoon northward in fully coupled CCSM2 simulations with a dynamic vegetation model. Clim Dyn 23:791–802. doi: 10.1007/s00382-004-0477-y

Liou KN (1986) Influence of cirrus clouds on weather and climate processes: A global perspective, Mon. Wea. Rev., 114, 1167-1198.

Liou KN (2002) An Introduction of Atmospheric Radiation, 2nd Edition, Academic Press, Chapter 8.

Manabe S, Stouffer RJ (1993) Multiple-Century Response of a Coupled Ocean-Atmosphere Model to an increase of Atmospheric Carbon Dioxide. J. Climate 7, 5-23, 1993.

Marcott SA, Shakun JD, Clark PU, Mix AC (2013) A Reconstruction of Regional and Global Temperature for the Past 11,300 Years. Science 339(6124):1198–1201. doi:

10.1126/science.1228026

Marsh DR, Mills MJ, Kinnison DE, Lamarque JF, Calvo N, Polvani LM (2013) Climate change from 1850 to 2005 simulated in CESM1(WACCM). J Clim 26:7372–7391. doi: 10.1175/JCLI-D-12-00558.1

Méhay S, Keller CE, Bermasconi SM, Weissert H, Erba E, Bottini C, Hochuli PA (2009) A volcanic CO2 pulse triggered the Cretaceous oceanic Anoxic event 1a and a biocalcification crisis. Geology 37:819–822. doi: 10.1130/G30100A.1

Meinshausen M, Smith SJ, Calvin K, Daniel JS, Kainuma MLT, Lamarque J, Matsumoto K, Montzka SA, Raper SCB, Riahi K, Thomson A, Velders GJM, van Vuuren DPP (2011) The RCP greenhouse gas concentrations and their extensions from 1765 to 2300. Clim Change 109:213–241. doi: 10.1007/s10584-011-0156-z

Meissner KJ, McNeil BI, Eby M, Wiebe EC (2012) The importance of the terrestrial weathering feedback for multimillennial coral reef habitat recovery. Global Biogeochem Cycles 26:1–20. doi: 10.1029/2011GB004098

Meissner KJ, Weaver AJ, Matthews HD, Cox PM (2003) The role of land surface dynamics in glacial inception: a study with the UVic Earth System Model. Clim Dyn 21:515–537. doi: 10.1007/s00382-003-0352-2

Mitchell L, Brook E, Lee JE, Buizert C, Sowers T (2013) Constraints on the Late Holocene Anthropogenic Contribution to the Atmospheric Methane Budget. Science 342(6161):964–966. doi: 10.1126/science.1238920

Monteiro FM, Pancost RD, Ridgwell A, Donnadieu Y (2012) Nutrients as the dominant control on the spread of anoxia and euxinia across the Cenomanian-Turonian oceanic anoxic event (OAE2): Model-data comparison. Paleoceanography 27:1–17. doi: 10.1029/2012PA002351

Moore JK, Lindsay K, Doney SC, Long MC, Misumi K (2013) Marine Ecosystem Dynamics and Biogeochemical Cycling in the Community Earth System Model [CESM1(BGC)]: Comparison of the 1990s with the 2090s under the RCP4.5 and RCP8.5 Scenarios. J Clim 26:9291–9312. doi: 10.1175/JCLI-D-12-00566.1

Mort H, Jacquat O, Adatte T, Steinmann P, Föllmi K, Matera V, Berner Z, Stüben D (2007a) The Cenomanian/Turonian anoxic event at the Bonarelli Level in Italy and Spain: enhanced productivity and/or better preservation? Cretac Res 28:597–612. doi: 10.1016/j.cretres.2006.09.003

Mort HP, Adatte T, Föllmi KB, Keller G, Steinmann P, Matera V, Berner Z, Stüben D (2007b) Phosphorus and the roles of productivity and nutrient recycling during oceanic anoxic event 2. Geology 35:483–486. doi: 10.1130/G23475A.1

Muller-Karger FE, Varela R, Thunell R, Luerssen R, Hu C, Walsh JJ (2005) The importance of continental margins in the global carbon cycle. Geophys Res Lett 32:1–4. doi: 10.1029/2004GL021346

Narita D, Tol RSJ, Anthoff D (2009) Damage costs of climate change through intensification of tropical cyclone activities: An application of fund. Clim Res 39:87–97. doi: 10.3354/cr00799

National Geophysical Data Center (2006) 2-minute Gridded Global Relief Data (ETOPO2) v2. National Geophysical Data Center, NOAA. doi:10.7289/V5J1012Q.

Nicholson SE (2009) A revised picture of the structure of the “monsoon” and land ITCZ over West Africa. Clim Dyn 32:1155–1171. doi: 10.1007/s00382-008-0514-3

Nicholson SE (2013) The West African Sahel: A Review of Recent Studies on the Rainfall Regime and Its Interannual Variability. ISRN Meteorol 2013:32. doi: 10.1155/2013/453521

Nicholson SE, Grist JP (2001) A conceptual model for understanding rainfall variability in the West African Sahel on interannual and interdecadal timescales. Int J Climatol 21:1733–1757. doi: 10.1002/joc.648

Niemeyer D, Kemena TP, Meissner KJ, Oschlies A (2017) A model study of warming-induced phosphorus–oxygen feedbacks in open-ocean oxygen minimum zones on millennial timescales. Earth Syst Dyn 8:357–367. doi: 10.5194/esd-8-357-2017

Oleson KW, Lawrence DM, Gordon B, Flanner MG, Kluzek E, Peter LJ, Levis S, Swenson SC, Thornton PE (2010) Technical Description of version 4.0 of the Community Land Model (CLM). NCAR/TN-478+STR NCAR Tech Note 266.

Ornstein L, Aleinov I, Rind D (2009) Irrigated afforestation of the Sahara and Australian Outback to end global warming. Clim Change 97:409–437. doi: 10.1007/s10584-009-9626-y

Oschlies A, Schulz KG, Riebesell U, Schmittner A (2008) Simulated 21st century’s increase in oceanic suboxia by CO 2-enhanced biotic carbon export. Global Biogeochem Cycles 22:1–10. doi: 10.1029/2007GB003147

Ozawa H, Okabayashi T, Komiyama H, Kaya Y (1995) Research of arid land afforestation technologies for carbon dioxide fixation. Energy Convers. Manag. 36:911–914.

Pacanowski RC (1996) MOM2: Documentation, User’s Guide and Reference Manual. GFDL Ocean Tech Rep 3.2:329pp.

Palastanga V, Slomp CP, Heinze C (2011) Long-term controls on ocean phosphorus and oxygen in a global biogeochemical model. Global Biogeochem Cycles 25:1–19. doi: 10.1029/2010GB003827

Parajuli SP, Yang Z-L, Lawrence DM (2016) Diagnostic evaluation of the Community Earth System Model in simulating mineral dust emission with insight into large-scale dust storm mobilization in the Middle East and North Africa (MENA). Aeolian Res 21:21–35. doi: 10.1016/j.aeolia.2016.02.002

Park JY, Bader J, Matei D (2015) Northern-hemispheric differential warming is the key to understanding the discrepancies in the projected Sahel rainfall. Nat Commun 6:5985. doi: 10.1038/ncomms6985

Park JY, Bader J, Matei D (2016) Anthropogenic Mediterranean warming essential driver for present and future Sahel rainfall. Nat Clim Chang 6:1–6. doi: 10.1038/nclimate3065

Paterson LA, Hanstrum BN, Davidson NE, Weber HC (2005) Influence of Environmental Vertical Wind Shear on the Intensity of Hurricane-Strength Tropical Cyclones in the Australian Region. Mon Weather Rev 133:3644–3660. doi: 10.1175/MWR3041.1

Patricola CM, Cook KH (2008) Atmosphere/vegetation feedbacks: A mechanism for

abrupt climate change over northern Africa. J Geophys Res 113:D18102. doi: 10.1029/2007JD009608

Paulmier A, Ruiz-Pino D (2009) Oxygen minimum zones (OMZs) in the modern ocean. Prog Oceanogr 80:113–128. doi: 10.1016/j.pocean.2008.08.001

Pausata FSR, Messori G, Zhang Q (2016) Impacts of dust reduction on the northward expansion of the African monsoon during the Green Sahara period. Earth Planet Sci Lett 434:298–307. doi: 10.1016/j.epsl.2015.11.049

Paytan A, McLaughlin K (2007) The Oceanic Phosphorus Cycle. Chem Rev 107:563–576. doi: 10.1021/cr0503613

Planavsky NJ, Rouxel OJ, Bekker A, Lalonde S V., Konhauser KO, Reinhard CT, Lyons TW (2010) The evolution of the marine phosphate reservoir. Nature 467:1088–1090. doi: 10.1038/nature09485

Pogge von Strandmann PAE, Jenkyns HC, Woodfine RG (2013) Lithium isotope evidence for enhanced weathering during Oceanic Anoxic Event 2. Nat Geosci 6:668–672. doi: 10.1038/ngeo1875

Polvani LM, Camargo SJ, Garcia RR (2016) The Importance of the Montreal Protocol in Mitigating the Potential Intensity of Tropical Cyclones. J Clim 29:2275–2289. doi: 10.1175/JCLI-D-15-0232.1

Prentice IC, Jolly D (2000) Mid-Holocene and glacial-maximum vegetation geography of the northern continents and Africa. J Biogeogr 27:507–519. doi: 10.1046/j.1365-2699.2000.00425.x

Rachmayani R, Prange M, Schulz M (2015) North African vegetation-precipitation feedback in early and mid-Holocene climate simulations with CCSM3-DGVM. Clim Past 11:175–185. doi: 10.5194/cp-11-175-2015

Redfield AC, Ketchum BH, Richards FA (1963) The influence of organisms on the composition of seawater. The Sea. Ed. M.N. Hill, 2, 26-77.

Riahi K, Rao S, Krey V, Cho C, Chirkov V, Fischer G, Kindermann G, Nakicenovic N, Rafaj P (2011) RCP 8.5-A scenario of comparatively high greenhouse gas emissions. Clim Change 109:33–57. doi: 10.1007/s10584-011-0149-y

Richter I, Xie SP (2008) On the origin of equatorial Atlantic biases in coupled general circulation models. Clim Dyn 31:587–598. doi: 10.1007/s00382-008-0364-z

Richter JH, Sassi F, Garcia RR (2010) Toward a Physically Based Gravity Wave Source Parameterization in a General Circulation Model. J Atmos Sci 67:136–156. doi: 10.1175/2009JAS3112.1

Rienecker MM, Suarez MJ, Gelaro R, Todling R, Bacmeister J, Liu E, Bosilovich MG, Schubert SD, Takacs L, Kim GK, Bloom S, Chen J, Collins D, Conaty A, Da Silva A, Gu W, Joiner J, Koster RD, Lucchesi R, Molod A, Owens T, Pawson S, Pegion P, Redder CR, Reichle R, Robertson FR, Ruddick AG, Sienkiewicz M, Woollen J (2011) MERRA: NASA's modern-era retrospective analysis for research and applications. J Clim 24:3624–3648. doi: 10.1175/JCLI-D-11-00015.1

Ruddiman WF (2003) The Anthropogenic Greenhouse Era Began Thousands of Years Ago. Clim Change 61:261–293. doi: 10.1023/B:CLIM.0000004577.17928.fa

Ruddiman WF (2006) The early anthropogenic hypothesis-challenges and responses. Rev Geophys 8:1749. doi: 10.1029/2006RG000207.1.INTRODUCTION

Ruddiman WF, Vavrus SJ, Kutzbach JE (2005) A test of the overdue-glaciation hypothesis. Quat Sci Rev 24:1–10. doi: 10.1016/j.quascirev.2004.07.010

Ruttenberg KC (2003) The Global Phosphorus Cycle. In: Treatise on Geochemistry. Elsevier, pp 585–643

Ruvalcaba Baroni I, Topper RPM, M. Van Helmond NAG, Brinkhuis H, Slomp CP (2014) Biogeochemistry of the North Atlantic during oceanic anoxic event 2: Role of changes in ocean circulation and phosphorus input. Biogeosciences 11:977–993. doi: 10.5194/bg-11-977-2014

Sabine CL (2004) The Oceanic Sink for Anthropogenic CO2. Science (80-) 305:367–371. doi: 10.1126/science.1097403

Saltzman MR (2005) Phosphorus, nitrogen, and the redox evolution of the Paleozoic oceans. Geology 33:573–576. doi: 10.1130/G21535.1

Sarmiento JL, Hughes TMC, Stouffer RJ, Manabe S (1998) Simulated response of the ocean carbon cycle to anthropogenic climate warming. Nature 393:245–249. doi: 10.1038/30455

Sarmiento JL, Slater R, Barber R, Bopp L, Doney SC, Hirst AC, Kleypas J, Matear R, Mikolajewicz U, Monfray P, Soldatov V, Spall SA, Stouffer R (2004) Response of ocean ecosystems to climate warming. Global Biogeochem Cycles 18:n/a-n/a. doi: 10.1029/2003GB002134

Sarmiento JL, Orr JC (1991) Three-dimensional simulations of the impact of Southern Ocean nutrient depletion on atmospheric CO2 and ocean chemistry. Limnol. Oceanog., 36, 8, 1928-1950.

Saunders M a, Harris AS (1997) Statistical evidence links exceptional 1995 Atlantic hurricane season to record sea warming. Geophys Res Lett 24:1255–1258. doi: 10.1029/97GL01164

Saunders M a, Lea AS (2008) Large contribution of sea surface warming to recent increase in Atlantic hurricane activity. Nature 451:557–560. doi: 10.1038/nature06422

Schlanger SO, Jenkyns HC (1976) Cretaceous oceanic anoxic events: Causes and consequences. Geol Mijnb 55:179–184.

Schmidtko S, Stramma L, Visbeck M (2017) Decline in global oceanic oxygen content during the past five decades. Nature 542:335–339. doi: 10.1038/nature21399

Schmittner A, Galbraith ED, Hostetler SW, Pedersen TF, Zhang R (2007) Large fluctuations of dissolved oxygen in the Indian and Pacific oceans during Dansgaard-Oeschger oscillations caused by variations of North Atlantic Deep Water subduction. Paleoceanography 22:1–17. doi: 10.1029/2006PA001384

Schmittner A, Oschlies A, Matthews HD, Galbraith ED (2008) Future changes in climate, ocean circulation, ecosystems, and biogeochemical cycling simulated for a business-as-usual CO 2 emission scenario until year 4000 AD. Global Biogeochem Cycles 22:n/a-n/a. doi: 10.1029/2007GB002953

Seitzinger SP, Mayorga E, Bouwman a. F, Kroeze C, Beusen a. HW, Billen G, Van Drecht G, Dumont E, Fekete BM, Garnier J, Harrison J a. (2010) Global river nutrient export: A scenario analysis of past and future trends. Global Biogeochem

Cycles. doi: 10.1029/2009GB003587

Semtner AJ (1976) A Model for the Thermodynamic Growth of Sea Ice in Numerical Investigations of Climate. J. Phys. Oceanogr., 6, 379-389.

Shepherd JG (2012) Geoengineering the climate: an overview and update. Philos Trans R Soc A Math Phys Eng Sci 370:4166–4175. doi: 10.1098/rsta.2012.0186

Slomp CP (2011) Phosphorus Cycling in the Estuarine and Coastal Zones. In: Treatise on Estuarine and Coastal Science. Elsevier, pp 201–229

Slomp CP, Van Cappellen P (2007) The global marine phosphorus cycle: sensitivity to oceanic circulation. Biogeosciences 4:155–171. doi: 10.5194/bg-4-155-2007

Smith LJ, Torn MS (2013) Ecological limits to terrestrial biological carbon dioxide removal. Clim Change 118:89–103. doi: 10.1007/s10584-012-0682-3

Smith P, Davis SJ, Creutzig F, Fuss S, Minx J, Gabrielle B, Kato E, Jackson RB, Cowie A, Kriegler E, van Vuuren DP, Rogelj J, Ciais P, Milne J, Canadell JG, McCollum D, Peters G, Andrew R, Krey V, Shrestha G, Friedlingstein P, Gasser T, Grübler A, Heidug WK, Jonas M, Jones CD, Kraxner F, Littleton E, Lowe J, Moreira JR, Nakicenovic N, Obersteiner M, Patwardhan A, Rogner M, Rubin E, Sharifi A, Torvanger A, Yamagata Y, Edmonds J, Yongsung C (2015) Biophysical and economic limits to negative CO2 emissions. Nat Clim Chang 6:42–50. doi: 10.1038/nclimate2870

Somes CJ, Oschlies A, Schmittner A (2013) Isotopic constraints on the pre-industrial oceanic nitrogen budget. Biogeosciences 10:5889–5910. doi: 10.5194/bg-10-5889-2013

Steenhof PA, Gough WA (2007) The impact of tropical sea surface temperatures on various measures of Atlantic tropical cyclone activity. Theor Appl Climatol 92:249–255. doi: 10.1007/s00704-007-0316-2

Steinacher M, Joos F, Frölicher TL, Bopp L, Cadule P, Cocco V, Doney SC, Gehlen M, Lindsay K, Moore JK, Schneider B, Segschneider J (2010) Projected 21st century decrease in marine productivity: a multi-model analysis. Biogeosciences 7:979–1005. doi: 10.5194/bg-7-979-2010

Stramma L, Johnson GC, Sprintall J, Mohrholz V (2008) Expanding Oxygen-Minimum Zones in the Tropical Oceans. Science 320(5876):655–658. doi: 10.1126/science.1153847

Stramma L, Oschlies A, Schmidtko S (2012) Mismatch between observed and modeled trends in dissolved upper-ocean oxygen over the last 50 yr. Biogeosciences 9:4045–4057. doi: 10.5194/bg-9-4045-2012

Swann ALS, Fung IY, Chiang JCH (2012) Mid-latitude afforestation shifts general circulation and tropical precipitation. Proc Natl Acad Sci U S A 109:712–6. doi: 10.1073/pnas.1116706108

Swann ALS, Fung IY, Liu Y, Chiang JCH (2014) Remote Vegetation Feedbacks and the Mid-Holocene Green Sahara. J Clim 27:4857–4870. doi: 10.1175/JCLI-D-13-00690.1

Taucher J, Oschlies A (2011) Can we predict the direction of marine primary production change under global warming? Geophys. Res. Lett, 38. doi: 10.1029/2010GL045934.

Taylor KE, Stouffer RJ, Meehl GA (2012) An overview of CMIP5 and the experiment design. Bull Am Meteorol Soc 93:485–498. doi: 10.1175/BAMS-D-11-00094.1

Thiéblemont R, Matthes K, Omrani N-E, Kodera K, Hansen F (2015) Solar forcing synchronizes decadal North Atlantic climate variability. Nat Commun 6:8268. doi: 10.1038/ncomms9268

Thorncroft CD, Nguyen H, Zhang C, Peyrille P (2011) Annual cycle of the West African monsoon: Regional circulations and associated water vapour transport. Q J R Meteorol Soc 137:129–147. doi: 10.1002/qj.728

Tierney JE, Pausata FSR, deMenocal PB (2017) Rainfall regimes of the Green Sahara. Sci Adv 3:1–9. doi: 10.1126/sciadv.1601503

Ting M, Camargo SJ, Li C, Kushnir Y (2015) Natural and Forced North Atlantic Hurricane Potential Intensity Change in CMIP5 Models*. J Clim 28:3926–3942. doi: 10.1175/JCLI-D-14-00520.1

Tsandev I, Slomp CP (2009) Modeling phosphorus cycling and carbon burial during Cretaceous Oceanic Anoxic Events. Earth Planet Sci Lett 286:71–79. doi: 10.1016/j.epsl.2009.06.016

Tyrrell T (1999) The relative influences of nitrogen and phosphorus on oceanic primary production. Nature 400:525–531. doi: 10.1038/22941

Van Cappellen P, Ingall ED (1994) Benthic phosphorous regeneration, net primary production, and ocean anoxia: a model of the couple biogeochemical cycles of carbon and phosphorous. Paleooceanography 9:667–692.

Vecchi G a., Soden BJ (2007) Increased tropical Atlantic wind shear in model projections of global warming. Geophys Res Lett 34:1–5. doi: 10.1029/2006GL028905

Wallmann K (2003) Feedbacks between oceanic redox states and marine productivity: A model perspective focused on benthic phosphorus cycling. Global Biogeochem Cycles 17:n/a-n/a. doi: 10.1029/2002GB001968

Wallmann K (2010) Phosphorus imbalance in the global ocean? Global Biogeochem Cycles 24:1–12. doi: 10.1029/2009GB003643

Wallmann K (2014) Is late Quaternary climate change governed by self-sustained oscillations in atmospheric CO2? Geochim Cosmochim Acta 132:413–439. doi: 10.1016/j.gca.2013.10.046

Wallmann K, Floegel S, Poulsen C, Voigt S, Kuhnt W (2010) Simulating the onset and spread of anoxic conditions during Cretaceous. 12:3236.

Wallmann K, Schneider B, Sarnthein M (2016) Effects of eustatic sea-level change, ocean dynamics, and nutrient utilization on atmospheric pCO2 and seawater composition over the last 130 000 years: A model study. Clim Past 12:339–375. doi: 10.5194/cp-12-339-2016

Wang S, Gillies RR (2011) Dynamic Linkage between the Sahel Greening and Intense Atlantic Hurricanes. Science and Technology Infusion Climate Bulletin NOAA's Weather Service: 3–6.

Wang Y, Holland GJ (1996) Tropical Cyclone Motion and Evolution in Vertical Shear. J. Atmos. Sci. 53:3313–3332.

Wang Y, Montgomery MT, Wang B (2004) How Much Vertical Shear Can a Well-Developed Tropical Cyclone Resist. In 26th Conf. on Hurricanes and Tropical Meteorology: 2-3.

Wang Y, Notaro M, Liu Z, Gallimore R, Levis S, Kutzbach JE (2008) Detecting vegetation-precipitation feedbacks in mid-Holocene North Africa from two climate models. 59–67. doi: 10.5194/cp-4-59-2008

Watson AJ, Lenton TM, Mills BJW (2017) Ocean deoxygenation, the global phosphorus cycle and the possibility of human-caused large-scale ocean anoxia. Philos Trans R Soc A Math Phys Eng Sci 375:20160318. doi: 10.1098/rsta.2016.0318

Weaver AJ, Eby M, Wiebe EC, Bitz CM, Duffy PB, Ewen TL, Fanning AF, Holland MM, MacFadyen A, Matthews HD, Meissner KJ, Saenko O, Schmittner A, Wang H, Yoshimori M (2001) The UVic earth system climate model: Model description, climatology, and applications to past, present and future climates. Atmosphere-Ocean 39:361–428. doi: 10.1080/07055900.2001.9649686

Webb MJ, Andrews T, Bodas-Salcedo A, Bony S, Bretherton CS, Chadwick R, Chepfer H, Douville H, Good P, Kay JE, Klein SA, Marchand R, Medeiros B, Pier Siebesma A, Skinner CB, Stevens B, Tselioudis G, Tsushima Y, Watanabe M (2017) The Cloud Feedback Model Intercomparison Project (CFMIP) contribution to CMIP6. Geosci Model Dev 10:359–384. doi: 10.5194/gmd-10-359-2017

Webster PJ, Holland GJ, Curry JA, Chang H-R (2005) Changes in Tropical Cyclone\rNumber, Duration, and Intensity\rin a Warming Environment. Science (80-) 309:1844–1846. doi: 10.1126/science.1116448

Wong M, Chan J (2004) Tropical cyclone intensity in vertical wind shear. J Atmos Sci 1859–1876. doi: 10.1175/1520-0469(2004)061<1859:TCIIVW>2.0.CO;2

Wu L, Su H, Fovell RG, Dunkerton TJ, Wang Z, Kahn BH (2015) Impact of environmental moisture on tropical cyclone intensification. Atmos Chem Phys 15:14041–14053. doi: 10.5194/acp-15-14041-2015

Wu L, Su H, Fovell RG, Wang B, Shen JT, Kahn BH, Hristova-Veleva SM, Lambrigtsen BH, Fetzer EJ, Jiang JH (2012) Relationship of environmental relative humidity with North Atlantic tropical cyclone intensity and intensification rate. Geophys Res Lett 39:2–9. doi: 10.1029/2012GL053546

Wu M-LC, Reale O, Schubert SD, Suarez MJ, Koster RD, Pegion PJ (2009) African Easterly Jet: Structure and Maintenance. J Clim 22:4459–4480. doi: 10.1175/2009JCLI2584.1

Yan Q, Korty R, Zhang Z (2015) Tropical Cyclone Genesis Factors in a Simulation of the Last Two Millennia: Results from Community Earth System Model. J Clim 150715142453002. doi: 10.1175/JCLI-D-15-0054.1

Yool A, Popova EE, Coward AC, Bernie D, Anderson TR (2013) Climate change and ocean acidification impacts on lower trophic levels and the export of organic carbon to the deep ocean. Biogeosciences 10:5831–5854. doi: 10.5194/bg-10-5831-2013

Yu J, Wang Y, Hamilton K (2010) Response of tropical cyclone potential intensity to a global warming scenario in the IPCC AR4 CGCMs. J Clim 23:1354–1373. doi: 10.1175/2009JCLI2843.1

Yu K, D'Odorico P, Bhattachan A, Okin GS, Evan AT (2015) Dust-rainfall feedback in West African Sahel. Geophys Res Lett 42:7563–7571. doi: 10.1002/2015GL065533

Zhang H, Henderson-Sellers A, McGuffie K (1996) Impacts of tropical deforestation. Part I: Process analysis of local climatic change. J. Clim. 9:1497–1517.

Zheng X, Duan YH, Yu H (2007) Dynamical effects of environmental vertical wind shear on tropical cyclone motion, structure, and intensity. Meteorol Atmos Phys 97:207–220. doi: 10.1007/s00703-006-0253-0

Abbreviations

AEJ	African Easterly Jet
AOU	Apparent Oxygen Utilization
C	Carbon
CaCO3	Calcium Carbonate
CAM	Community Atmospheric Model
CAPE	Convective Available Potential Energy
CAPE*	Convective Available Potential Energy for a Saturated Air Parcel
CE	Climate Engineering
CESM	Community Earth System Model
CH_4	Methane
CICE	Community Ice CodE
CLM	Community Land Model
CMIP5	Coupled Model Intercomparison Project Phase 5
CO_2	Carbon Dioxide
DIP	Dissolved Inorganic Phosporus
ESCM	Earth System Climate Model
ESM	Earth System Model
GCM	General Circulation Model
GHG	Greenhouse Gas
IPCC	Intergovernmental Panel on Climate Change
ITCZ	Intertropical Convergence Zone
ITF	Inner-Tropical Front
LW	Longwave
MDR	Main Development Region
MDR	Main Development Region
N	Nitrogen
N_2O	Nitrous Oxide
NCAR	National Center for Atmospheric Research
NPP	Net Primary Production
NPZD	Nutrient-Phytoplankton-Zooplankton-Detritus
O	Oxygen
OAE	Oceanic Anoxic Event

OMZ Oxygen Minimum Zones

ONPP Ocean Net Primary Production

P Phosphorus

PFT Plant Functional Type

PMIP Paleoclimate Modelling Intercomparison Project

PO_4 Phosphate

POP Parallel Ocean Program

RCP Representative Concentration Pathways-Scenario

RRPOC Rain Rate of Organic Carbon

SAT Surface Air Temperature

SAT Surface Air Temperature

SAZ Sahel Zone

SST Sea Surface Temperatures

SW Shortwave

T_0 Outflow Temperature

TC Tropical Cyclone

TOA Top of the Atmosphere

TRMM Tropical Rainfall Measurement Mission

UVic University of Victoria

VMAX Maximum Potential Intensity

WACCM Whole Atmosphere Community Climate Model

WAM West African Monsoon

Erklärung

Hiermit erkläre ich, dass die vorliegende Arbeit mit dem Titel: '*Assessment of Feedbacks in the Earth System under Anthropogenic Forcing: Two Case Studies*' von mir selbstständig angefertigt wurde. Bis auf zitierte Referenzen und Beratung meiner Betreuer wurden keine weiteren Quellen verwendet. Diese Arbeit ist unter Einhaltung der Regeln guter wissenschaftlicher Praxis der Deutschen Forschungsgemeinschaft entstanden. Sie wurde weder im Rahmen eines Prüfungsverfahrens an anderer Stelle vorgelegt noch veröffentlicht. Ich erkläre mich einverstanden, dass diese Arbeit an die Bibliothek des GEOMAR und die Universitätsbibliothek der CAU weitergeleitet wird.

Kiel, Oktober 2017

(Tronje Kemena)